



Development of an in-vitro intestinal model featuring peristaltic motion

Lauriane G  r  mie

► To cite this version:

Lauriane G  r  mie. Development of an in-vitro intestinal model featuring peristaltic motion. Biological Physics [physics.bio-ph]. Sorbonne Universit  , 2019. English. NNT : 2019SORUS118 . tel-03155665

HAL Id: tel-03155665

<https://theses.hal.science/tel-03155665>

Submitted on 2 Mar 2021

HAL is a multi-disciplinary open access archive for the deposit and dissemination of scientific research documents, whether they are published or not. The documents may come from teaching and research institutions in France or abroad, or from public or private research centers.

L'archive ouverte pluridisciplinaire **HAL**, est destin  e au d  p  t et    la diffusion de documents scientifiques de niveau recherche, publi  s ou non,   manant des   tablissements d'enseignement et de recherche fran  ais ou   trangers, des laboratoires publics ou priv  s.

Sorbonne Université

Ecole doctorale Physique en Île-de-France

*Institut Curie, UMR168 / Equipe Macromolécules et Microsystèmes en Biologie et en
Médecine*

Development of an *in-vitro* intestinal model featuring peristaltic motion

Par Lauriane Gérémié

Thèse de doctorat de Biophysique

Dirigée par Stéphanie Descroix et Jean-Louis Viovy

Présentée et soutenue publiquement le 25 Janvier 2019

Devant un jury composé de :

Mme Audrey Ferrand, CR (Rapporteur)

M Abdul Barakat, PR (Rapporteur)

M Jacques Fattaccioli, MCF (Examineur SU)

M Sylvain Monnier, MCF (Examineur)

Mme Danijela Vignjevic (Invitée)

Mme Stéphanie Descroix (Invitée, Co-directrice de thèse)

M Jean-Louis Viovy (Directeur de thèse)

Acknowledgements

.

*On ira trinquer au sommet du monde,
On lèvera nos verres à ceux qui n'en feront alors plus partie,
Aux dignes vaincus de la vie, cette course contre la tombe
Et on boira à nos familles, à nos vieux potos et à tout ce qu'on aura construit*
Mall'Oh, On va le faire, 2016

A ma famille
En hommage à Jean Gérémie

.

Table of contents

INTRODUCTION	1
1 INTRODUCTION TO THE INTESTINE	3
1.1 The gut into shape	5
i) Anatomy of the Intestine	5
ii) Structure of the Intestine	7
iii) The intestinal properties	10
1.2 The intestinal geometry	11
i) The epithelium	12
ii) The mesenchyme	16
1.3 The ecosystem of the intestine	19
i) Microbial population	19
ii) Enteric Nervous System	20
iii) Immune system, microbiota, neuronal network: the <i>Triumvirate</i> of the intestine	22
1.4 The dynamics of the intestine	23
i) Anatomical point of view	23
ii) Intestinal contraction	24
2 THE GUT-ON-CHIP	27
2.1 The Emergence of the Organ-on-Chip field	29
i) Introduction to the organ on chip field	29
ii) The first Organ-on-Chip	32
2.2 State-of-the-art of the Gut-on-Chip models	34
i) The 3D structured <i>Gut-on-chip</i> models	35
ii) The mechanically active <i>Gut-on-chip</i> models	38
2.3 Development of our Gut-on-Chip platform	42
i) Discussion	57
ii) Materials and Methods	58
3 FROM STATIC TO DYNAMIC	67
3.1 The influence of the mechanical environment	69
i) At the cellular level	69
ii) At the tissue level	72

3.2	Stretching platforms, the <i>State-of-the-art</i>	74
i)	Different stretching technologies	74
ii)	Biological responses to cells stretching	80
iii)	Focus on : intestinal epithelial stretching	84
3.3	Peristalsis-on-chip	87
i)	Stretcher	87
ii)	3D stretching chips microfabrication	92
iii)	Calibration	94
3.4	Conclusion	97
4	HOW DOES STRETCHING AFFECT INTESTINAL EPITHELIUM?	99
4.1	Determination of the operating conditions	101
i)	PDMS Chips	101
ii)	Coating of the chips	102
iii)	Seeding of the cells	103
iv)	Stretching of the chips	104
4.2	Influence of intestinal cells stretching on 2D experiments	105
i)	How does stretching affect the tissue state?	105
ii)	How does cell stretching affect the cell morphology?	111
iii)	How does cell recover the stretching influence?	120
iv)	How does stretching affect primary cell: Organoids ?	121
4.3	Influence of the stretching on 3D experiments	122
i)	How stretching does affect the covering of the patterns ?	124
ii)	Influence of topography on the cellular alignment in the grooves	127
4.4	Conclusion	134
	CONCLUSION AND PERSPECTIVES	137
	A IMMUNOSTAINING PROTOCOL	141
	B CODE OF THE FIRST STRETCHERS	143
	C CODE OF THE FINAL STRETCHER	147
	BIBLIOGRAPHY	149

Introduction

Over the last 10 years, the biotechnology field has taken benefit of the convergence of tissue engineering and microfluidics leading to the development of a new technology for life sciences: the Organ-on-chips. These organ-on-chip platforms reproduce the key features of specific tissue microenvironment (cells, extracellular matrix...) with a precise fluidic, geometrical and mechanical control to address tissue-specific questions. The predictive power of these in vitro models has the potential to transform the drug discovery industry and to provide researchers and clinicians with new and valuable tools. Therefore, it has attracted large interest, and currently, almost every organ of the human body has been reproduced on-chip. My thesis project lies in this emerging and exciting field and more precisely in the Gut-on-chip context.

The Gut was one of the first organs reproduced on-chip, since a plethora of models have been reported with various level of complexity. From these models, the technological approaches can be divided in two types of strategy: the reproduction of the intestine microenvironment either in terms of architecture or in terms of mechanical constraints. Previously to my work, a first PhD was performed on the Gut-on-chip field and followed the first strategy, resulting in the development of an innovative 3D structured gut-on-chip recapitulating its complex architecture and some essential components of the intestinal stroma. This first study represents the foundation of my own work which focuses on the development of a platform recapitulating both the architecture and the mechanical constraints of the intestine. Indeed, the problematic of my PhD work was to assess the influence of one specific mechanical constrain of the gut, namely the peristalsis, on intestinal cells seeded on a 3D scaffold.

First, I had to build a 3D structured, mechanically active and biocompatible Gut-on-chip platform, which was at the same time a technological and biophysical challenge. Indeed, the first part of my PhD work was mainly to design and develop a platform recapitulating all the previously mentioned features as well as compatible with cell culture conditions and observations. This part allow me to develop my competences in electronics, 3D printing and micro-milling. Once achieved this versatile platform allow us to apply a controlled stretching on cells seeded either on a 2D or a 3D scaffold. To complete this study we had to optimize the cells culture conditions under stretching as well as the staining and imaging protocol. The completeness of this PhD project offers me the opportunity to discover the complexity of the Organ-on-chip field, through the concrete example of the Gut-on-chip.

In the first chapter of this manuscript, I will first introduce the reader to my organ of predilection; the intestine. I proposed in the first chapter a vast description of this organ to better understand its complexity.. Moreover, this non-exhaustive description allows the reader to better asses the choices made by every scientist working in the organ-on-chip field about the selection of the features which need to be implemented in the platform and the one which will be missing.

This choice is central in the second chapter, where various gut-on-chips are described underlying the chosen features to recreate as faithfully as possible the intestine microenvironment. I also participate to the development of an original gut-on-chip platform and our choices are discussed in an article presented in the last part of this chapter.

The third chapter focuses on the mechanical environment of the cells, first through a short introduction to the mechanotransduction. Then we study the technological solutions reported to reproduce this mechanical environment and how cell response to mechanical constraints have been described in the literature, with a specific focus on the intestinal cells. . Finally, this chapter ended by the description and characterization of my technological developments. In the last chapter of the manuscript, the technologies developed during my PhD have been used to investigate how epithelial intestinal cells respond to stretching and how this response is modified when cells are grown in 3D. Different parameters will discussed in particular of cells get oriented as function of the stretching time.

Chapter

1

Introduction to the intestine

Contents

1.1	The gut into shape	5
	i) Anatomy of the Intestine	5
	ii) Structure of the Intestine	7
	iii) The intestinal properties	10
1.2	The intestinal geometry	11
	i) The epithelium	12
	ii) The mesenchyme	16
1.3	The ecosystem of the intestine	19
	i) Microbial population	19
	ii) Enteric Nervous System	20
	iii) Immune system, microbiota, neuronal network: the <i>Tri- umvirate</i> of the intestine	22
1.4	The dynamics of the intestine	23
	i) Anatomical point of view	23
	ii) Intestinal contraction	24

Introduction

An eighty years old person spends on average 25 years sleeping and 2 years eating. These two activities are fundamental to human survival. Indeed, the first one is essential to allow the human organism to physically restore itself and for memory processing. Whereas the second one provides one source of chemical energy required for the proper functioning of the human body.

To eat, is the action to introduce food into our body in a tubular system occupying a major part of our abdomen, extending from the mouth to the anus. The path followed by the food is called the gastrointestinal (GI) tract. During its GI travelling, the food undergoes major transformations where it is broken into molecules small enough to be absorbed. The sum of all these processings is called the digestion (*dis* = apart; *gerere* = to carry). It has to be as efficient as possible to extract as much energy as possible from a given amount of food. To do so, the digestion takes place in a succession of complementary organs, one after the other each with its own function.

The first step of this process is a mechanical digestion, namely the mastication. It takes place in the mouth where the teeth chew the aliments then the tongue mixes it with saliva to assist the swallowing. This mixture of food and saliva, called the bolus, travels down through the oesophagus until reaching the stomach where it is mixed with protease and hydrochloric acid to become a partially digested food: the chyme. Then the chyme continues its path, reaching the intestine. The name "intestine" gathers two different organs together, the small and the large one. The intestine and the gut refer generally to the small intestine, where the large intestine is also called the colon. The small intestine is the first one in the gastrointestinal tract, it is where most of the absorption of the nutrients takes place. Then, the colon absorbs the water and the remaining waste is stored as feces until evacuation through the rectum.

In this digestive path, the small intestine plays the role of the front door of our organism: a gateway for nutrients and a barrier for bacteria. To fulfil these two main functions the gut has specific properties such as its specially adapted morphology, its rich stroma and its complex dynamics as it will be discussed in the following sections.

1.1 The gut into shape

The intestine is in charge of the absorption of the nutrients in the GI tract. This function can be achieved thanks to its large surface compared to the other organs of the GI tract, as illustrated in the *Figure 1.1*. The exact measurement of its surface was challenging, due to its complex 3D shape. Therefore, it has been overestimated for a long time to 300m^2 , that is in the order of magnitude of a tennis court, but a recent study reassesses its surface area to 30m^2 [1]. Still making the intestine the largest exchange surface area of our body.

In this chapter I will first describe the general anatomy of the intestine, before focusing on its emblematic pattern: the villi and crypts.

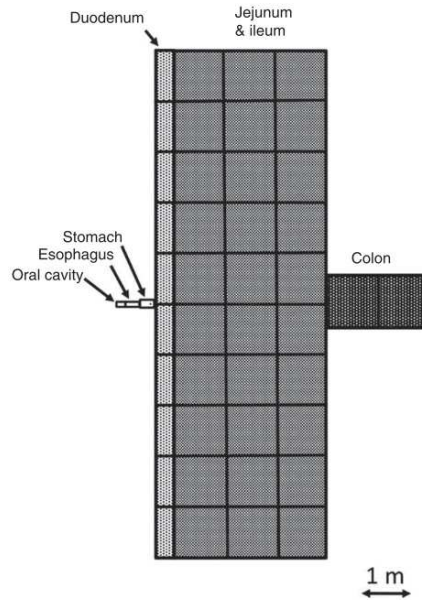


Figure 1.1: Approximation of the distribution of the mucosal luminal surfaces along the digestive tract done by Helander *et al.*

i) Anatomy of the Intestine

The intestine is a tube separating the external environment, called the lumen, from the inner environment. Its length alone is between 3 to 5 meters providing already a large surface area further increased by folds, villi and microvilli. The intestine is divided into three parts in aboral direction: the duodenum, jejunum and ileum. This discrimination is related to morphological changes appearing along the intestinal tract, illustrated in the *Figure 1.2*.

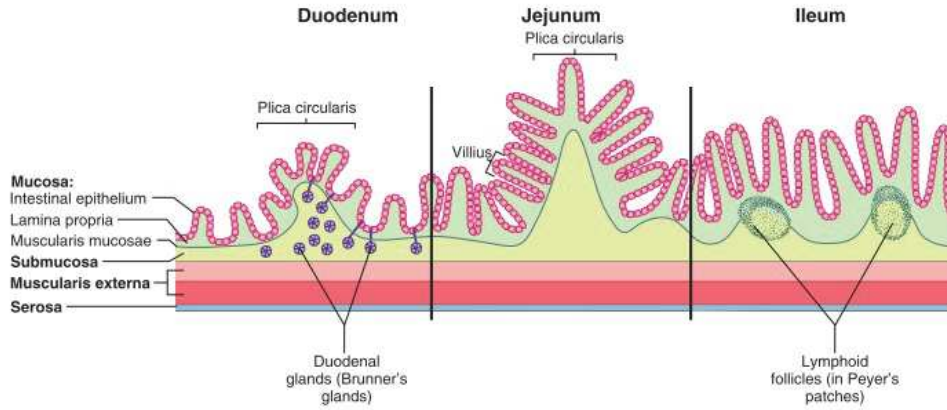


Figure 1.2: Schematic view of the different parts of the intestine done by Rehfeld et al. [2]

Duodenum

The first part of the intestine is the duodenum, so-called by *Herophilus of Chalcedon* a Greek anatomist because of its short length, *dodekadaktylon* means 12 fingerbreadths in greek which is about twenty centimeters [3]. It is in a "C" shape and makes the junction between the stomach and the jejunum.

One particularity of the duodenum is the presence of Brunner's glands. They are unique to mammalian species, and only present in the first few millimeters of the duodenum's submucosa. They are secretory glands, that mainly produce mucin glycoproteins to form a viscoelastic gel to lubricate, and more importantly to protect the epithelium from gastric acid. The mucus is delaying the diffusion of acid to provide enough time to be neutralized by the bicarbonate secreted by the intestinal epithelium. In addition, Brunner's glands produce other factors such as epidermal growth factor important in wound healing and differentiation and some bactericidal factors such as lysozyme [4].

Jejunum

The second part of the intestine is the jejunum and is about 1 meter long. It is the site of the absorption. To distinguish the jejunum from the duodenum one specific clue is the aparition of folds of the mucosa and submucosa about 10mm high: the *Circular folds*. They increase the surface area by a factor 3 and enhance the exchange by causing the chyme to spiral rather than move in straight line [5], textitFigure 1.3 presents an illustration of the cross-section of these structures.

An other important difference is the shape of the protrusions made by the mucosa and submucosa. These protrusions named *Villus* are emblematic of the intestine, in the duodenum, they are mainly leaf-like [1].

Ileum

Finally, the last and longest (~ 2 meters long) part of the intestine is the ileum. As the last site of absorption in the GI tract, it supports the enterohepatic circulation, meaning the active absorption of the bile salts (95%) into the portal circulation for transport back to the liver [6].

Besides, most of the bacterial population present in the intestine is concentrated in this part, i.e. because of the low pH of gastric contents in the upper part of the intestinal tract [7]. Therefore, a more developed lymphatic network is found in the Ileum illustrated by the important concentration of Peyer's patches (50%) [8].

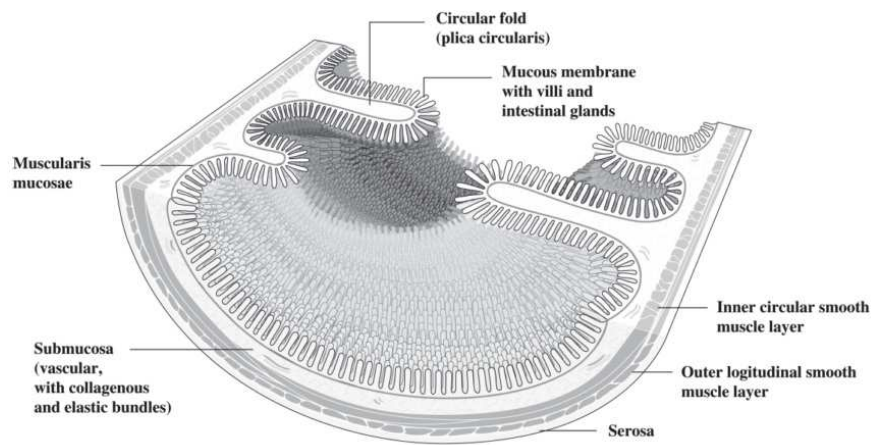


Figure 1.3: Representation of a cross-section of the proximal small intestine made by DeSesso et al. [7]

ii) Structure of the Intestine

The walls of the intestine consist in a juxtaposition of 4 layers of concentric tissues, illustrated in the *Figure 1.4*. This arrangement is basically the same from the esophagus to the anal canal. From the inner to the external layer are: the mucosa, submucosa, muscularis and serosa [5].

Mucosa

The mucosa is a mucous membrane composed of an epithelium in direct contact with the bowel, a layer of connective tissue namely the lamina propria, and a thin layer of smooth muscle called the muscularis mucosae.

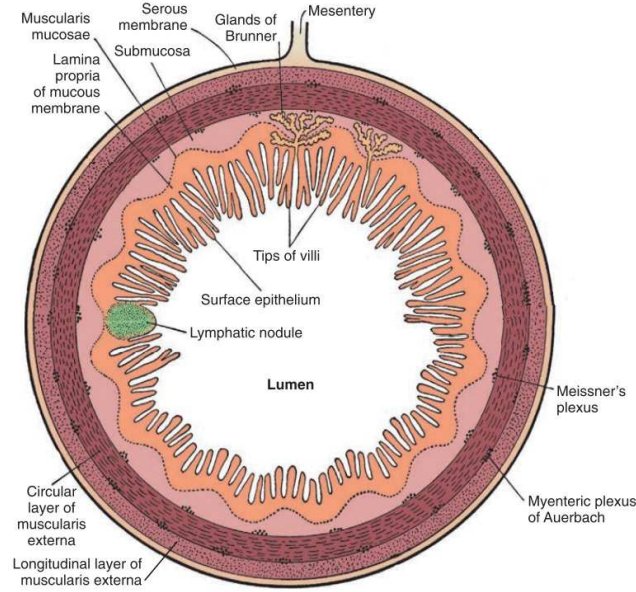


Figure 1.4: Representation of a cross-section of the intestine tube adapted from Charles J. Yeo [6]

- The epithelium is a simple columnar monolayer composed of a heterogeneous group of cells, it supports functions such as absorption and secretion of mucus. The cells of this epithelium have a polarised structure with an apical plasma membrane facing the gut lumen, responsible for the absorption of the nutrients. And a baso-lateral membrane which maintains the integrity of the epithelium, thanks to a strong cell-cell contact allows by various types of junctions such as the tight junctions.
- The lamina propria is an areolar connective tissue containing many blood and lymphatic vessels. It binds the epithelium to the muscularis mucosae. Most of the immune system resides there, it consists of isolated or aggregated lymphoid follicles, named the gut-associated lymphoid tissue (GALT). It is one of the largest lymphoid organs, containing up to 70% of the body's immunocytes. The aggregated lymphoid follicles, called the Peyer's patches are considered as the immune sensors of the intestine. A complex interplay between immune cells located in the core of the Peyer's patches and the subjacent epithelium, called the follicle-associated epithelium (FAE), induces an immune tolerance or defence respectively against commensal bacteria or luminal pathogens. This mucosal tolerance protects the mucosa from detrimental inflammatory immune responses by the regulation of T-cell differentiation after antigen exposure [8].
- Finally, the muscularis mucosae is responsible for the undulation of the villi to allow every cell to be in contact with the bolus, helping the absorption.

Submucosa

The submucosa is composed of areolar connective tissue that binds the mucosa to the muscularis. As for the muscosa, it contains many blood and lymphatic vessels. Some glands can also be found like in the duodenum. A specificity of the submucosa is the presence of an extensive network of neurons called the submucosal plexus [5]. The neuronal population of the intestine will be discussed in more details in the third part of this chapter (1.3).

Muscularis

The musucularis consists of two layers of smooth muscle, an inner sheet of circular fibers and an outer sheet of longitudinal fibers.

These layers of muscle play a double role in the dynamics of the gut. The first one, during morphogenesis as a major actor of the villification of the gut. Indeed, it has been shown that the differentiation of the smooth muscle cells, generates a compressive stress acting as a mechanical barrier restraining the circumferential expansion of the intestine. This muscle-driven constraint leads to the folding of the growing endoderm and the formation of villi [9]. On the other hand, the apparition of the crypts occurs later in the development as the final step in tissue maturation [10].

The second role of the muscularis happens all along life, as the contraction of the intestine helping to break down the food, mix it with intestinal fluids and propulsion along the intestine. These wall movements are called segmental and peristaltic motion. They will be further described in the section 1.4.

Interestingly, between the musucular layers we found a second plexus of neurons called the myenteric plexus.

Serosa

The serosa is a serous membrane composed of areolar connective tissue and an epithelium. It secretes fluid to provide lubrication and prevents friction due to digestion movements of the intestine in the abdomen. The serosa is connected to the mesentary that suspends the intestine from the wall of the abdomen, it is an elastic tissue offering structural support and allowing movement to the digestive tract [11].

iii) The intestinal properties

In the gut, the lamina propria has a non-trivial 3D geometry made of finger-like extrusions and well-like invagination, respectively the Villi and the Crypts (also known as *Crypt of Lieberkühn* termed after their discoverer Jonathan Nathanael Lieberkühn (1711–1756) [12]).

This 3D geometry is an evolutionarily conserved shape, found in many vertebrates including the chicken, pig, mouse and human but also in vertebrates such as zebrafish and amphibians [13–15]. Some villi are present in the stomach and crypts in the colon [5], but the combination is singular to the gut. In average, the villi is 500 μm high and the crypt is 100 μm depth in human.

The villus core contains in its center a lymphatic channel, named lacteal, allowing the absorption of lipids along with a dense blood network carrying the nutrients to the rest of the body (*Figure 1.5*) [5]. Moreover, the villus is populated by a multitude of stromal cells, such as the pericytes that support the microcirculation, or the vertically-aligned smooth muscle cells shelf of the lacteal system and engaged in the contraction of individual villus.

In the human, the villi are 20 to 40 per square millimeter, surrounding each by approximately 6 crypts, their presence increases the surface area of the gut by a factor of 6.5 [1].

The crypt is defined as stem cell compartment or 'niche', a biomechanically suitable micro-environment for stem cell survival and function [16, 17]

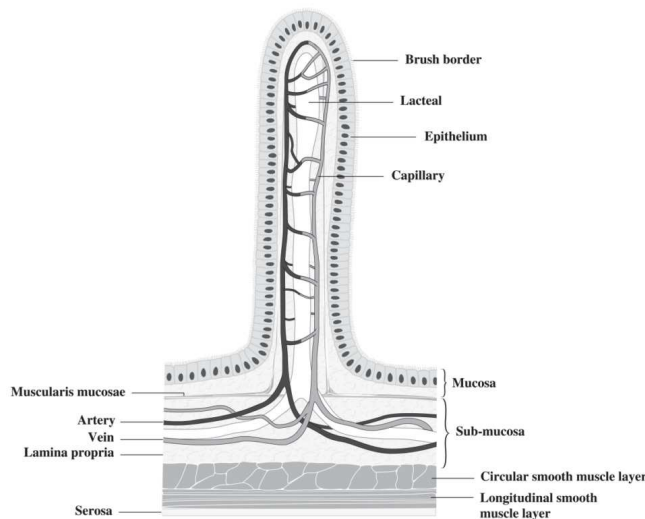


Figure 1.5: Representation of the internal organisation of the intestinal Villus by DeSesso *et al.* [7]

1.2 The intestinal geometry

The non-trivial 3D geometry of the intestine, namely the Villus and the Crypt, is one of its emblematic feature. These two sub-geometric units can be distinguished by the cellular process occurring at there emplacement. Indeed, in the intestine, cell function and location are correlated. More precisely, the crypt is the unit of proliferation and the villus is the unit of differentiation and absorption.

The cells composing the epithelium of the gut have been the subject of many researches since the last fifty years due to their remarkable renewal potential [18]. Indeed, the cells located at the bottom of the crypt are stem cells, meaning they can generate progeny and renewing themselves by division [12, 19, 20]. The stem cells of the gut have the fastest rate of the human body (one division every 24 hours [12]), indeed they have to supply a sufficient amount of cell to counterbalance the daily lost of 10^{11} epithelial cells in the intestinal lumen [21]. To ensure this turnover the crypts display a hierarchical structure well organized, described in the following [20, 22].

Exiting the crypt, the cells migrate along the crypt-villi axis, while differentiating. The migration is here indiscernible from the differentiation. This cellular adaptation results in differentiated cells covering the villi mandatory for a proper functioning of the intestine. Finally, they reach the top of the villi where they die by anoikis (*Figure 1.6*).

This process ensures the integrity of the epithelium, it is an harmonious balance between cell life and death maintained by a complex interplay between the epithelium and the mesenchyme.

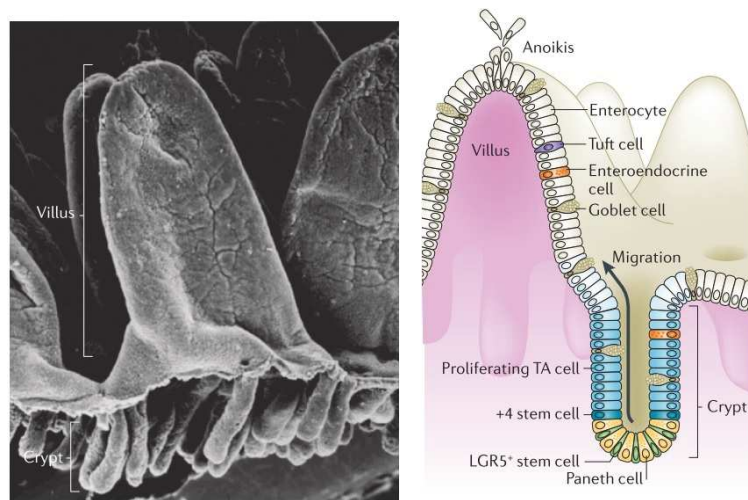


Figure 1.6: Representation of the villus and crypt with the adjacent epithelium made by Barker *et al.* [20]

i) The epithelium

The intestine epithelium is a cell monolayer that covers all the surface of the intestine walls. It consists of differentiated cells (with various cell types, that will be further discussed), as well as intestinal stem cells and transit amplifying cells. Such stem cells display two basic characteristics: self-renewal and multipotency [12].

Starting from the bottom of the crypt, labelled as position 0, are located the stem cells pool spreading until the position +3, occupied by approximately 3 to 16 crypt base columnar (CBC) stem cells evenly distributed between Paneth cells [20]. Then, the position +4 is occupied by the + 4 stem cells also called the Intestinal Stem Cells (ISCs) reserve. Indeed, the destruction of the $Lgr5^+$ CBC cells pool does not induce the destruction of the crypt, suggesting the presence of a robust regenerative response, supposedly located at this position [22].

From the position +5 until the end of the crypt the cell population is called the transit-amplifying (TA) cells. These cells are the result of the division of CBC cells and have the capacity to divide 2 to 3 times before undergoing differentiation themselves while migrating upwards. They can be divided into three sub-populations, the absorptive progenitor, the secretory progenitor and the paneth cell progenitor which give rise respectively to the absorptive enterocyte; the enteroendocrine cell, Tuft cell, Goblets cell and the Paneth cells. This cellular distribution is illustrated in the *Figure 1.7*.

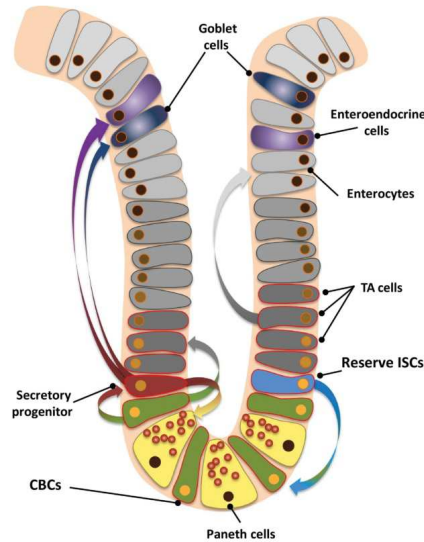


Figure 1.7: Representation of the population laying in the intestinal crypts by Yousefi *et al.* [22]

The Crypt Base Columnar stem cells

The CBC cells have been identified thanks to a stemness gene the Leu-rich repeat-containing G protein-coupled receptor 5 (Lgr5) and confirmed using mouse model [20]. They are considered as active stem cells, responsible for the daily epithelial homeostasis driven by the surrounding micro-environment. They undergo asymmetric divisions approximately 95% of the time, resulting in one stem cell and one highly proliferative progenitors called TA cells [23].

The Paneth cells

Paneth cells are the exception in the migration-differentiation dynamics of the gut. Indeed, they are differentiated cells and exclusively located in the crypt. Moreover, they are renewed only every 3 to 6 weeks as compared to the 5 days life time of other differentiated cells. They contain large apical secretory granules and secrete lysozyme and anti-bacterial peptides to protect the epithelium from contamination due to the proximity of bacteria present in the food [16]. Most noteworthy, Paneth cells provide key niche signals, such as Epithelial growth factors (EGF), Wnt3 and Notch essentials for the maintenance of stem cells [24]. Indeed, in vivo loss of Paneth cells induces the depletion of stem cells but not a complete disparition, suggesting redundant sources of Wnt [25]. Moreover, Paneth cells are sensitive to calorie restriction, initiating the reduction in the size of the CBC cells pool if needed [20].

The Intestinal Stem cells reserve

The +4 stem cells population has been first distinguished from the CBC stem cells because of their peculiar properties. Actually, +4 stem cells are 'quiescent' cells residing outside the cell cycle in G0, they reveal high resistance to DNA damage and little readouts of canonical Wnt pathway. Moreover, they can give rise to all intestinal cell types and they are indispensable for epithelial maintenance under normal and injured conditions.[22]

The Transit-Amplifying cells

Among the TA population, an interesting capacity has been found to asymmetrically divide to selectively retain the older DNA or 'immortal' parental DNA strand [26]. These Label-retaining cells (LRCs) are supposed to be secretory progenitors and Paneth progenitors that can reacquire CBC identity in case of injury, demonstrating the high plasticity of the crypt[27].

Once the cells exit the crypt they are differentiated and can ensure the digestive function of the gut. This epithelium is composed of three major cell types: the absorptive enterocytes, entero-endocrine cells and goblet cells. Finally, all the cells are intended to die at the tip of the villus. The cells undergo a programmed cell death induced by anchorage-dependent cells death after detachment from their matrix, named anoikis. It is supposedly helpful to maintain a normal size of epithelial cells population and serve to preserve intestinal homeostasis [28].

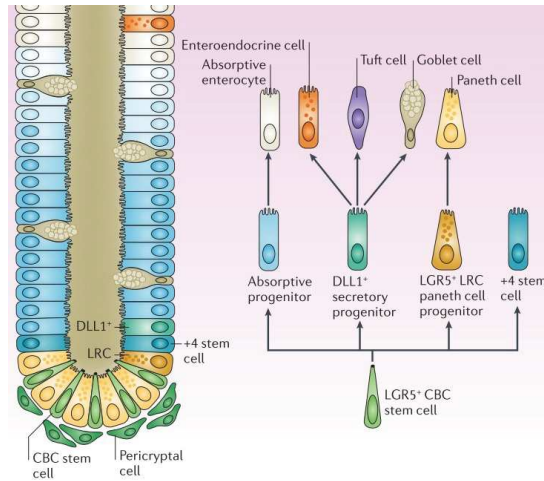


Figure 1.8: Representation of the differentiation pathways followed by intestinal cell from [20]

Enterocytes

In the intestine, the digestion is carried out by the absorptive cells, namely the enterocytes, which represents 80% of the epithelium. These cells are highly polarised with an apical membrane made of 450 microvilli per cell [29] called the brush-border. These microvilli have pretty uniform dimensions along the intestinal tract: 100 nm diameter and 1 μ m to 3 μ m length [30]. The resulting surface enlargement is averaged to 13 times [1]. These microvilli are the main site of absorption. Indeed, they have brush-border enzymes helping the digestion of carbohydrates, proteins and lipids. Once the food is transformed into these digest nutrients they are small enough to be absorbed by the absorptive cells to reach the underlying network of blood and lymphatic vessels.

The enterocytes are also involved in the immunity response of the gut, they produced antibacterial proteins that mixed with the mucus generate an antibacterial layer keeping the bacteria away from the epithelial cell surface.

Goblet cells

The Goblet cells are the first line of defence against microbes. They secrete the intestinal mucus that protects the epithelium from the shear stress induced by the passage of the bolus and acts as a barrier against bacteria [31]. Interestingly, the goblet cells are also active agents in the immune response through the goblet-cell-associated antigen passages (GAPs). They are able to act as a passage delivering low molecular weight antigens from the intestinal lumen to the dendritic cells of the lamina propria [32].

Entero-endocrine cells

The enteroendocrine adjective is a general nomination for a group of cells responsible of the hormonal response of the gut. These cells secrete over 20 different gut hormones, and are involved in wide range of biological events [33]. Nevertheless, they can be gathered together into two groups. The first one is composed of L-cells, K-cells and CCK-cells playing the role of receptors, to sense the nutrients in the food and therefore secrete the appropriate hormones to promote either food intake or satiety, insulin secretion or suppression of gastric acid secretion [34].

The second group is composed of microfold cells (M cells) and the tuft cells, they are both involved in immune response. The M cells populate mainly the Peyer's patches and act as immunosurveillance cells. They possess receptors on their apical surfaces that enable them to sample a diverse range of microbial pathogens and antigens [35]. On the other hand, the tuft cells are particular due to their elongated morphology with an apical border made of long and thick microvilli. Recently, they have been identified as the trigger to induction of the type 2 immune response following parasite infections [36].

ii) The mesenchyme

The mesenchyme of the intestine, so called the lamina propria or stroma, is a connective tissue. It has a large influence on the homeostasis and maintenance of the intestinal form. Remarkably, highly expressed epithelial genes are intestine specific where nearly all genes in the intestinal stroma are expressed in numerous additional tissues. It seems that the stroma is a "reservoir" of soluble signaling proteins for various signaling pathways, and for all of them soluble inhibitors and modulators are dominantly or exclusively in the stroma, highlighting its substantial potential to activate or suppress important guiding pathways [37].

The stroma is a 3D matrice made of extra cellular matrix (ECM). It is densely populated by non-hematopoietic, non-epithelial and non-endothelial cells, named "stromal cells", as fibroblasts, myofibroblasts, pericytes, bone marrow stromal cells, and smooth muscle cells [38]. These cells possess a high plasticity and functional properties like contractility, production and remodelling of the ECM. As a consequence, they are involved in a wide range of biological responses such as wound healing, fibrosis and tumor progression. Moreover, recent researches demonstrate the role of the stromal cells in immune responses [39].

These cells seem to be resident sentinels, able to sense bacterial, damage-associated and inflammatory signals. And to respond through the production of chemokines, resulting in the recruitment of immune cells such as lymphocytes and macrophages. Furthermore, the stromal cells are able to regulate T cell proliferative responses, playing an important role in the tolerance process of the intestine [38]. These cells can assume either an immunosuppressive role or an immunostimulatory role depending on their micro-environment. To underline these new functional properties of these cells a new nomenclature "non-hematopoietic immune cells" has been proposed [40].

Now that the active role of the stroma in the global homeostasis is clear, I will focus the discussion on its implication for the intestine. Stromal cells together with signalling pathways are the keepers of the integrity of the intestine, indeed they are key factors in the architecture of the crypt/villus axis, segregation and maintenance of the intestinal stem cells [41].

Development of the Crypt/Villus architecture in small intestine morphogenesis and through life

The Hedgehog (Hh) pathway is unidirectional: from the epithelium to the mesenchyme and is essential for villus development. Experiments performed on genetically modified mice reports villus phenotypes depending on the expression level of Hh signal. Mice with an important reduction in Hh signalling have a flat, hyperproliferative and pseudostratified epithelium, they barely survived after birth. Even mice with a slight attenuation of Hh signalling exhibit already important loss of polarity compare to normal epithelium, displaying disorganized villi with nascent crypts on the sides and branches [42]. These chaotic architectures are the result of the mislocated intestinal subepithelial pericryptal myofibroblast (ISEMF), triggered by Hh signal. Indeed, in normal intestine the ISEMFs are located around the base crypt where they act as anchor for the proliferative cells [43]. In mice with reduced Hh signal the ISEMFs are found in the villous core and tips leading to the formation of proliferative areas on the villous, as illustrated by the immunofluorescent images in the *Figure 1.9* [44].

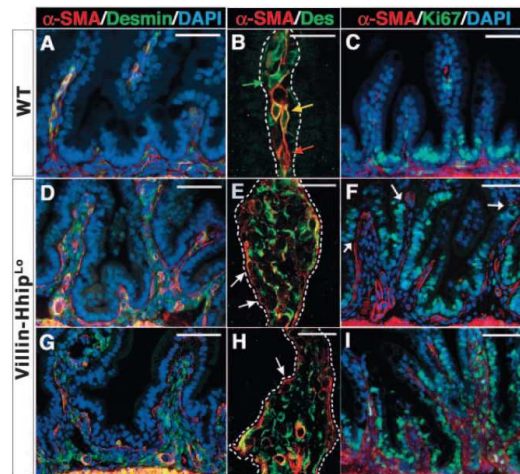


Figure 1.9: Immunofluorescent images of wild type and *Hh* deficient mice, α -SMA (in Red) staining the myofibroblast, desmin (in Green) is expressed by smooth muscle cells precursor and pericytes, Dapi (in blue) stained the nucleus and Ki67 (in green) the proliferative cells, obtained by Madison *et al.* [44]

Moreover, one of the supposed stromal target of the Hh pathway is the *Bmp4* ligand from the bone morphogenetic protein (BMP) family. This ligand is secreted by intravillus stromal cells [45] and involved in the inhibition of the intestinal stem cell expansion. The BMP signalling prevent the hyperproliferation of the *Lgr5*⁺ stem cells niche by directly repressing the expression of the stem cell signature genes, preventing a subsequent epithelium outgrowth in physiological conditions [46]. The BMP signalling follows a gradient along the crypt-villus axis, activated in the villus it is suppressed toward the base of the crypt due to antagonist mainly expressed by ISEMFs [39].

This collaboration between Hh and BMP signals spatially restricts the formation of the crypt compartment to the intervillus base. It is a striking example of the close regulation between the ISCs and their niche. Controlled localisation of the proliferative area is required to the proper functioning of the gut but superfluous if they cannot maintain their stemness.

Maintenance of the intestinal stem cells

One of the most important and reviewed intestinal pathway is the Wnt signalling. This pathway is essential for stem cell proliferation [47]. A complete block-out of Wnt signalling induces the lost of *LGR5*⁺ stem cells and the proliferative crypt [48]. As an insurance, this signalling pathway is redundant in the crypt environment. Indeed, epithelium Wnt signal (*Wnt3*) has been found to be secreted by the Paneth cells, as well as by fibroblasts. Interestingly, Paneth cells are a source, but also depend on Wnt, suggesting the existence of an autocrine signaling loop [43]. Moreover, Wnt signal acts as short-range intercellular signals mainly between adjacent cells which spatially delimits the niche and the number of stem cells at the bottom of the crypt [49].

Interestingly, Wnt signalling seems able to trigger Notch activity. The Notch pathway is a cell-cell communication. As a result, Paneth cells which express Notch ligands and are adjacent to intestinal CBC stem cells, can influence their decision to self-renew or differentiate into one of the secretory lineages[50]. Indeed, inhibition of the Notch pathway causes rapid conversion of all proliferative crypt cells into goblet cells [48]. Moreover, the Notch pathway influences through lateral inhibition the choice between an absorptive and a secretory fate [41]. It is a feedback loop allowing the diversity of the intestinal epithelium, cells becoming committed to a secretory fate express Notch ligands and inhibit their neighbours from differentiating in the same way [51].

1.3 The ecosystem of the intestine

The intestine is, as previously discussed, a complex 3D structure made of villi and crypts. This structure is a support for the dense epithelium covering it, as well as for the stromal cells and immune system living into its heart. This already complex ecosystem only represents the visible tip of the iceberg. Indeed, two other main cell types can be found in the intestine: the beneficial microbial community and the complex nervous network. We will discuss in the following section how the cells composing the epithelium, the immune system and the microbiota formed an alliance to reach together a matured state [52] supervised by the enteric Nervous System (ENS) [53].

i) Microbial population

The gastrointestinal tract is one of the most densely populated habitat in the human body with 10^1 , 10^3 , 10^4 , 10^7 and 10^{12} microbial cells per gram of content respectively in the stomach, duodenum, jejunum, ileum and colon [54]. This massive amount of cells, so called the microbiota, is mainly composed of bacteria living almost exclusively in the lumen. The colonisation of the intestine starts after birth and is stabilized to an 'adult state' around 1 to 2 years of age. The microbial population can be considered as an additional organ and is, as a signature, unique to each of us [54].

The microbiota as for a long time only be considered as pathogenic and solely an immunological threat, but recent investigations have highlighted its beneficial influence on human health [54–56]. Studying the influence of the microbiota on the gut epithelium has been challenging, as only 20 to 40 % of the bacterial species from the mammalian gastrointestinal tract can be cultured in *in vitro* conditions. The development of germ-free (GF) animal models since the late 1940s provides most of the information regarding the role of bacteria in host development.

Bacteria are involved in a wide range of biological reactions, they facilitate the metabolism of otherwise indigestible polysaccharides, produce essential vitamins and confer a protection against invasions of opportunistic pathogens [54]. Furthermore, they are required for the development and differentiation of the host's intestinal immune system [54, 55, 57]. Indeed, microbial colonization drives maturation of the lymphoid tissues, such as T cell specialization toward a pro- or an anti-inflammatory profile determining the overall immune equilibrium [54].

Moreover, intestinal epithelial cells are able to sense the presence of microorganisms thanks to a range of pattern recognition receptors (PRR), such as toll-like receptors (TLR) and nucleotide oligomerization domain- like receptors (NLR), expressed at their membrane [54]. Activation of the PRR triggers downstream signalling inducing expres-

sion of proinflammatory cytokines, chemokines and soluble immunoglobulin A (IgA) [58]. This activation is adjusted to avoid chronic stimulation of inflammatory signaling by the resident microbiota while maintaining responsiveness to pathogens [55]. Interestingly, the presence of commensal bacteria induces the goblet cells differentiation, producers of the mucin which serves as nutrients source and restricts at the same time the bacteria growth [54].

Being able to understand the symbiosis between the microbiota and the gut is a great challenge and could help us to understand the immune tolerance, fundamental in drug screening as the intestine is by far the largest antibody-producing organ in the body [55].

ii) Enteric Nervous System

The human nervous system is composed of two complementary systems, the central nervous system (CNS) and the peripheral nervous system (PNS). The CNS comprised the brain and the spinal cord, it contains the majority of the nervous system and coordinates all parts of the body. The PNS, on the other hand encompasses all the nerves outside the brain and the spinal cord. It is the link between the CNS and the organs.

The PNS is divided into the somatic nervous system, in charge of the voluntary control of body movements, and the autonomic nervous system. The autonomic nervous system handles all the unconscious functions, such as heart and respiratory rate, digestion and urination. The autonomic nervous system can be divided into three systems, the sympathetic and parasympathetic systems respectively responsible for the "flight or fight" and "rest and digest" responses. The third component of the autonomic nervous system is the enteric nervous system (ENS) [59].

The ENS is referred as the "second brain" of our body [60], due to its large number of neurons about 200 to 600 millions. This number is almost similar to the number of neurons contained in the spinal cord [61]. Moreover, it is the original nervous system emerging in the first vertebrates over 500 millions years ago [59]. The ENS is in charge of the digestion in the entire gastro-intestinal tract, and controls three essential functions: wall movement, water and electrolyte balance and local blood flow. The ENS is quite independent from the CNS, severing the connections between the CNS and the GI tract, through sympathetic and parasympathetic nerves, has relatively minor effects on digestion. In contrast, absence of ENS is lethal in various species [61].

The ENS is found in the submucosa and between the muscular layers respectively named the submucosal plexus and the myenteric plexus. All neurons are exposed to pressure, nutrients and endocrine hormones [62]. The myenteric plexus regulates the muscle rythm of the gut and the submucosal plexus the chemical monitoring and glandular secretion [59]. These plexus are composed of approximately 20 types of enteric neurons [61], they can be sort into three classes :

The intrinsic primary afferent neurons (IPANs) represents about 14 to 30% of the neurones. They act as sensors and detect activity in the lumen of the GI tract. They respond to changes in the luminal chemistry, such as chemicals contained in the food, and are sensitive to strength, such as the mechanical distortion of the mucosa due to the passage of the bowel [5, 61].

The interneurons are the link between sensory and motor neurons, they propagate neuronal impulses [52, 63].

The motor neurons represent 56% of the neurons and are of two kinds: the muscle motor neurons and the "sensor" motor neurons [63]. The first ones comprise (1) the excitatory and inhibitory circular muscle motoneurons that project to the circular muscle. Their axons are associated to ensure a balanced response and a modulated effect on the radial contraction. (2) The longitudinal muscle motoneurons are involved in the peristaltic motion. They all respond to signals initiated by mechano- and tension receptors. The second category is mainly located in the submucosal plexus where they represent 30 to 40% of the neurons. They mediate the transport of water and electrolytes across the intestinal mucosa. Some infective agents can abnormally activated these neurons resulting in fluid loss, such as cholera toxin[52, 61, 63].

The implication of the ENS in the intestinal motility is clear, therefore studying the interaction between the smooth muscle cells and the ENS is privileged to understand dismotility [64]. But surprisingly, the gut-brain communication has been implicated in Parkinson disease. Indeed, patients with Parkinson disease show degradation of enteric neurons several years before motor symptoms suggesting that the ENS is an initial site of the disease. Therefore the intestinal neurons could be an early biomarker of the disease [53].

iii) **Immune system, microbiota, neuronal network: the *Triumvirate* of the intestine**

The two populations described above are key regulators of the intestinal homeostasis and a cross talk has been identified between them through the immune system. As a matter of fact, common regulatory mechanisms are shared by the enteric neurons and intestinal immune cells to coordinate their responses. Examples have been found during organogenesis, as the neurotrophic-factor receptor and neuroregulator RET, expressed by lymphoid-tissue-inducer cells, essentials for ENS development and Peyer's patches formation. Moreover, quiescent hematopoietic stem cells and neuroectodermal progenitor cells which give rise, respectively, to all lineages of immune cells and all enteric neurons and glia rely on survival signals provided by factor induced by RET activation [65].

Furthermore, collaborating mechanisms have been found during the maturation of intestinal neural circuits and immune system mainly driven by the luminal microenvironment, namely the microbiota. Indeed, germ-free mice have fewer enteric neurons, altered ratios of neuronal subtypes, deficits in gut motility and underdeveloped immunological network. Interestingly, reconstitution of GF mice with conventional microbiota normalized the density of EGC network and gut physiology. One striking example of this collaboration is the microbial factors (short-chain fatty acids (SCFAs)) secreted by bacteria promoting the production of serotonin by intestinal epithelium essential for the maturation of intestinal motor reflexes [53].

Moreover, in the daily life, some neuroregulatory molecules are expressed by intestinal immune cells and act on enteric neurons. An example is the neuron-macrophage interactions in response to microbial signals. The muscularis macrophages (MMs) present in intestinal muscles are in close contact with ENS cells, once activated they expressed proteins (BMP) that activates enteric neurons which produce stimulatory factor (CSF1) that contributes for MM development and enhances this tissue-protective reaction [53].

1.4 The dynamics of the intestine

The intestine is a puzzling organ, with various attributes from its non-trivial architecture to its biodiversity, made of a plethora of cells organised in a neuronal, immune and stromal framework, a microbiota and an epithelium. Finally, a last peculiarity needs to be discussed to have a complete picture of the intestine; its contraction.

The intestine, as part of the GI tract, is a duct for the food through our body, where occurs the digestion. This travel, namely the propulsion of the bolus, is critical for life. Without intestinal contraction neither digestion or discharge of the intestine can be ensured. This motility follows the "law of the intestine" first enumerated by William Bayliss and Ernest Starling in 1899, who reported that excitation at any point of the gut causes contraction above and inhibition below [66].

i) Anatomical point of view

The walls' movements of the intestine rely on the collaboration between (1) the ENS that detects the contents of the gut, (2) the Interstitial cells of Cajal (ICC) that links the neurons to the smooth muscle and (3) the muscularis that interprets inputs and develops appropriate responses. These three components are essential, if one of them is missing motility disorders will occur [67].

The muscularis of the intestine is composed of a longitudinal and a circular layer of smooth muscles. These cells form a junctional network surrounding the lumen. Adjacent cells are coupled mechanically, by intermediate junctions that allow parallel transmission of contractile proteins along the longitudinal axis, and electrically by gap junctions that permit stream of ions and thus electric currents to passively flow between cells [68]. The smooth muscles of the digestive tract answer to ICC that dictate the rhythm of contractions and are innervated by the autonomic nervous system which can also modulate the contractile response.

The ICC are named accordly to the spanish Nobel Laureate physician Santiago Ramon y Cajal that identified in 1893, intestine "interstitial cells" located between the nerve endings and smooth muscle cells. These cells are organised in dense networks located in the myenteric plexus and in the deep muscularis propria, they represent 5 to 9% of the total number of cells in the muscle layers [68]. They possess the intrinsic ability to periodically depolarize their membrane producing spontaneous electrical "slow waves" at a frequency of 12 per min in the duodenum.

The ICCs in the myenteric plexus initiate the slow wave activity spreading to the smooth muscle, and the intramuscular ICCs propagate the slow wave through the GI tract [6]. These "slow waves" dictate the rhythm, meaning the frequency and propagation, of the electrical contractile activity of the gut. Therefore the ICCs are considered as the pacemakers of the intestine [67].

This depolarization, however, is not significant enough to reach the excitatory threshold of the muscle cells, the slow waves are the base line of the intestine, essential but not sufficient for contraction of the intestine. A contraction is achieved when a slow wave and an excitatory impulse from a motor neuron of the enteric nervous system occur simultaneously [69]. On top of their pacemaker activity, recent studies suggest a role of ICCs in neurotransmission. Indeed, they seem able to integrate excitatory and inhibitory neurotransmission with slow-wave activity to orchestrate peristaltic motor activity in the gut [70]. In particular the ICC of the deep muscular plexus are densely innervated by excitatory and inhibitory enteric motor neurons, therefore mediating the enteric neural input to the GI muscle cells [71].

The ENS activity determines the pattern of contractile activity of the intestine by delivering an electrical spikes on the plateau phase of the slow-wave activity inducing the contractile activity. Moreover, chemical factors can stimulate or inhibit GI motility such as hormones, neurocrines, paracrine and also autocrine factors [72].

ii) Intestinal contraction

The contractile activity of the gut has two distinctive sequence, respectively during periods of fasting or feeding. The feeding state sequence is dominated by peristaltic and segmental motions whereas the interdigestive state is based on the Migrating Motility Complex (MMC) [68]. The daily distribution of these two movement sequences is proposed in the *Figure 1.10*.

The MMC is a propagative cycle of activity that lasts 90 minutes and is divided into three phases. The phase I, is a quiescent period where only the "slow waves" are detected, it is a rest phase that contributes to 30% of the cycle. The phase II, is characterized by intermittent and irregular contractions, contributing to 60% of the total cycle length. Finally, the phase III is cadenced by intense and regular contractions that propagate from proximal to the distal intestine over 10 minutes [6]. This phase is the housekeeper of the gastrointestinal tract, and is essential to prevent bacterial overgrowth. The MMC seems to necessary for the clearance of residues from the gut lumen [74]. Moreover, studies have shown a reduction in propagation velocity of the MMC at night and the nearly absence of phase II, suggesting that the MMC has a circadian pattern [69].

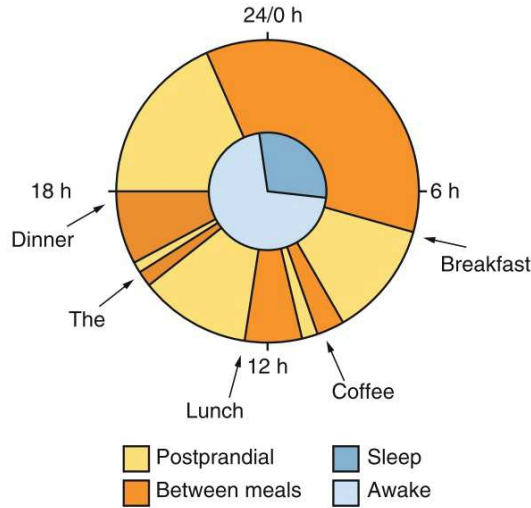


Figure 1.10: Representation of the intestinal contact activity in a daily life, froms Bredenoord *et al.* [73]

The presence of fluid and nutrients in the small bowel suppresses the intrinsic inter-digestive sequence, over the entire small bowel and activates reflexes that control the digestive process. This response is nutrient-dependant through stimulation of nutrient-specific gut receptors. Two main movement sequences are involved in the digestion, the peristaltic and segmental motion [72]. The segmental motion is a localized contraction of the intestine's wall in response to the increased diameter of the intestine due to the passage of chyme. This mechanical stimuli seems to activate sensory neurons, that in response induce a new rhythm to the ICCs of the deep muscular plexus, changing the movement sequence from propulsion to segmentation. The segmental motion increase the contact between the food and the mucosa to optimize the absorption [75].

The peristaltic motion is defined as a propulsive motor pattern that involves contraction of the intestinal segment above the chyme and relaxation below, propelling luminal contents in the aboral direction [68]. A schematic view of this dynamic is proposed in the *Figure 1.11*. This pattern necessitates a high coordination between the excitatory motor neurons that contract the upper segment of circular muscle while the inhibitory neurons simultaneously relax the lower intestinal segment [6]. This motor pattern is essential for the transport of the bolus through the GI tract and increases the absorption of the nutrients [73]. Interestingly, it has been shown that the peristaltic pattern of gut switches from a rather chaotic pattern (ripples) in the early postnatal period to a highly coordinated pattern after postnatal day 10 [65].

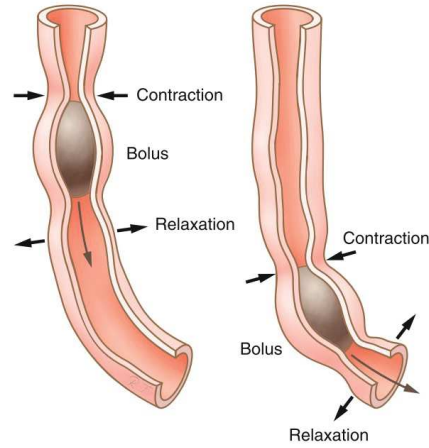


Figure 1.11: *Schematics of the peristaltic motion from Bredenoord et al. [73]*

Conclusion

In this first chapter, I tried to provide the reader with a complete picture of the intestine at various scale. As an organ, the intestine is elementary for life. It is in charge of the absorption of nutrients, while maintaining a barrier with the outside world. This function is supported by its complex geometry enhancing its absorption surface, an important cellular diversity made of intestinal cells, stromal cells, immune cells and neurons to ensure its proper functioning, and a contractile activity to maintain its integrity.

In my PhD work, I have focused on two main aspects of the gut. First, we aimed at recapitulate its complexity *in vitro* by developing a 3D gut-on-chip, as it will be discussed in the second chapter dedicated to the Organ-on-chip field. Then the chapter 3 and 4 will describe how I have developed and used specific tools to investigate the effect of stretching and geometrical constrains on intestinal cells behavior.

Chapter 2

The Gut-on-chip

Contents

2.1	The Emergence of the Organ-on-Chip field	29
i)	Introduction to the organ on chip field	29
ii)	The first Organ-on-Chip	32
2.2	State-of-the-art of the Gut-on-Chip models	34
i)	The 3D structured <i>Gut-on-chip</i> models	35
ii)	The mechanically active <i>Gut-on-chip</i> models	38
2.3	Development of our Gut-on-Chip platform	42
i)	Discussion	57
ii)	Materials and Methods	58

Introduction

The first chapter has described the gut complexity. Despite a large knowledge on the underlying mechanisms of the gut physiology, there are still open questions to be addressed regarding gut related mechanisms. In this context, *in vitro* models appear as relevant tools to address biological and biophysical questions. Among the different *in vitro* models, organ-on-chip provides the researchers with an unprecedented level of control.

An organ-on-a-chip is a microfluidic cell culture device created with microchip manufacturing methods that contains continuously perfused chambers inhabited by living cells arranged to simulate tissue- and organ-level physiology.

Sangeeta N. Bhatia and Donald E. Ingber, Microfluidic organ on chip, Nature Biotechnology, 2014

To illustrate the potential of this field, I will in the next section explain the emergence of this field and describe one of the pioneer organ-on-chip developed by Ingber team. Then, I will focus on my organ of interest, the gut-on-chip, and investigate the cohort of existing models, discussing their advantages and limitations. Finally, I will present the proposed *Gut-on-chip* developed in our team to which I participated during my PhD.

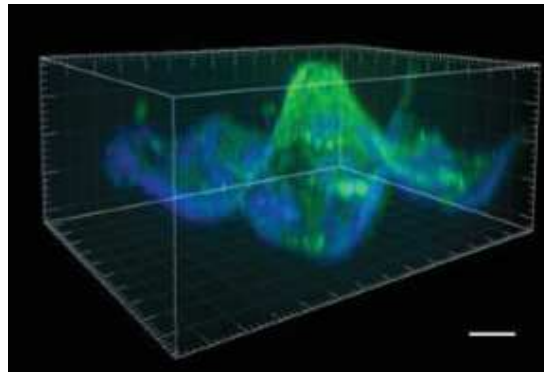


Figure : Picture of the 3D gut-on-chip developed during the PhD of Marine Verhulsel, after 7 days the primary epithelial monolayer colonized the whole structure (nuclei in blue and actin in green)

2.1 The Emergence of the Organ-on-Chip field

The emergence of the organ-on-chip field has been made possible thanks to the convergence of microengineering with microfluidics and cell biology. The unique development of micro-fabrication techniques inherited from the microelectronics industry, such as photolithography, etching and micro-milling, makes possible the generation of chips with structures of few microns with a complete control of the 3D architecture. The manipulation of liquids at such scale has given rise to the definition of Microfluidics. The laminar flow induced by these reduced dimensions allows the precise generation and control of fluid flows and spatio-temporal gradients with a high resolution. The adaptation of Microfluidics for cell culture has led to the development of micro-devices with relevant microarchitecture and microenvironment, in terms of biochemical signals in particular nutrients or other chemical cues to grow cells in a dynamics controlled manner [76–79].

i) Introduction to the organ on chip field

Today, the organ on chip toolbox is quite rich, various chip materials (plastic, glass, poly(dimethyl- siloxane) (PDMS)) can be used. Besides, this conventional chip materials, hydrogels can be also integrated in microfluidics devices (such as collagen, matrigel, agarose or laminin) in order to mimic on chip the organ ECM. Moreover, the integration of biosensors as tools to monitor cell behavior, electronics to generate electrical simulations has allowed an accurate control of cell behavior on chip. Besides, technological solutions have been proposed to reproduce on chip the physical forces applied on cells such as (shear stress, cyclic strain and/or mechanical compression). Altogether, these technological developments have allowed to reach an unprecedented level of biomimetism and control with these organ on chip platforms [76, 79–82].

Currently, almost every organ has been reproduced on-chip with various level of complexity such as the Lung-on-chip [83], Gut-on-chip [84, 85], Liver-on-Chip[78], Heart-on-chip [86], Skin-on-chips [87], Kidney-on-chip [88], Bone-on-chip [89], Brain-on-chip [90] or the specific Blood-Brain-Barrier-on-chip [91]. This plethora of examples is illustrated in the Figure 2.1, where they can be fluidically combined to a Human-on-chip.

Meanwhile, peculiar models have bloomed focusing on anatomical dysfunctions such as the Metastasis-on-chip [92] or Tumor-on-chip to screen and test the effectiveness of treatments. These models open up the possibilities to use these microfluidic systems in patient-specific applications where personalized therapeutic treatment options can be explored in order to quickly identify an optimal treatment [93, 94].

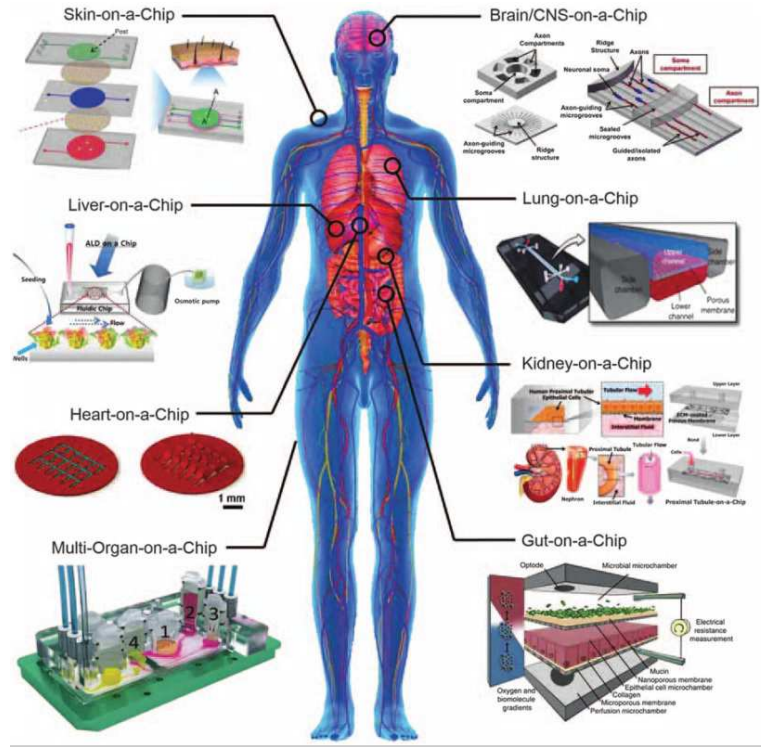


Figure 2.1: Representation of the multitude of organ-on-chip available, allowing the study of every organ composing the human body from Dhawan et al. [95]

The organ-on-chips are currently considered as promising tools for biology and biophysics, but also as screening drug platforms as an intermediary between the 2D cell culture and the animal models. Drug failures in clinical trials are mainly due to the poor predictive power of existing preclinical models and the limitations of inter-species physiological differences [94, 95]. Therefore important efforts have been deployed by the pharmaceutical industry to develop organ-on-chip for drug screening [96–98].

For example, liver toxicity is one major reason for drug withdrawal, therefore the liver-on-chip was one of the first commercially available systems: the LiverChip, developed by the Massachusetts Institute of Technology (MIT) [78]. The organ-on-chip field is expecting to answer to the critical need for new testing approaches, while following the 3R principle, postulated by Russel and Burch in the 1960s, becoming aware of the need for reduction, refinement, and replacement of animal experiments [78].

The needs of the pharmaceutical companies combined with the will to get a new generation of in vitro models for biology and biophysics has led to the emergence of at least 28 organ-on-chip companies in less than 7 years [99].

After the successful recapitulation of single organs on chip, the next step has been to move towards multi organ-on-chip systems. A first example was the Liver/Skin - on-chip platform [100]. This platform allows a cross talk between these two organs in order to estimate how the liver, the principal actor for drug metabolism, behaves to test the allergic potential of skin products, important for the cosmetic industry. Later Human-on-chip platforms were developed combining several organs within a human-like metabolizing environment with the potential to determine the toxicity caused by treatment and/or to study the drug pharmacokinetics and pharmacodynamics as well as the interplay between tissues physically separated in vivo but linked through circulation (the side effects) [78, 95, 101].

One striking example is the *Four-organ-chip* platform with a reconstructed human 3D small intestine, a skin biopsy, a 3D liver and a kidney proximal tubule compartment, *Figure 2.2*. The two first organs, the gut and the skin, allow either oral or dermal substance absorption. These compartments provide the barrier function between the apical side and the surrogate blood circuit. Then a micro-pump enables the distribution from the basolateral side of these compartments to the liver equivalent enabling primary substance metabolism. Finally, the microfluidic channel crosses a membrane seeded with renal proximal tubule cells, supporting metabolite excretion within a second excretory circuit. This four-organ-chip model was cultivated over 28 days and used to ensure good absorption, distribution, metabolism and excretion of drugs a primordial test in pharmacology [102].

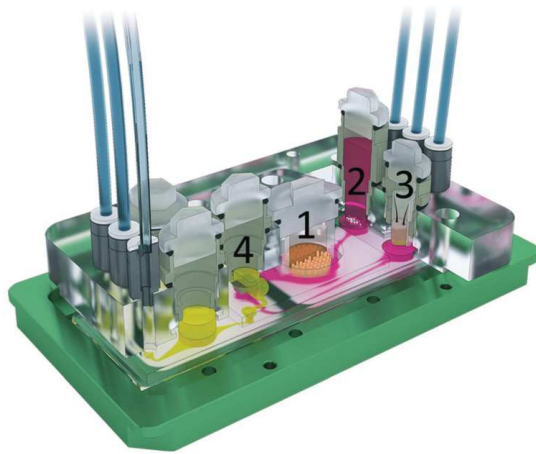


Figure 2.2: 3D view of the device with the blood (pink) and excretory (yellow) circuit. Numbers represent the four tissue culture compartments: intestine (1), liver (2), skin (3) and kidney (4).[102]

ii) The first Organ-on-Chip

As previously mentioned, the term organ-on-chip has been introduced by Donald Ingber, who developed for the first time a microfluidic chip to recapitulate the human lung features [83, 99].

This chip was made of PDMS and composed of three chambers. The central part is subdivided in two channels by an horizontal elastic porous membrane. This membrane is one of the major asset of this model: it allows the compartmentalization of the channel, while exchange is maintained through the pore of the membrane to allow diffusion between the channels to create biochemical gradients for example. The two external chambers are connected with a cyclic vacuum system, to induce a cyclic depression which in turn pulls on the main chamber's walls, inducing the stretching of the PDMS membrane.

The first version of this lung-on-chip model, illustrated in the *Figure 2.3*, manages to recapitulate the functional alveolar-capillary interface with the co-culture of alveolar epithelial cells and microvascular endothelial cells on opposite surfaces of the same porous membrane. The epithelial microchannel is full of air where the alveolar cells are maintained at an air-liquid interface. Moreover, cyclic stretching of the tissue-tissue interface was implemented to mimic physiological breathing movements [83].

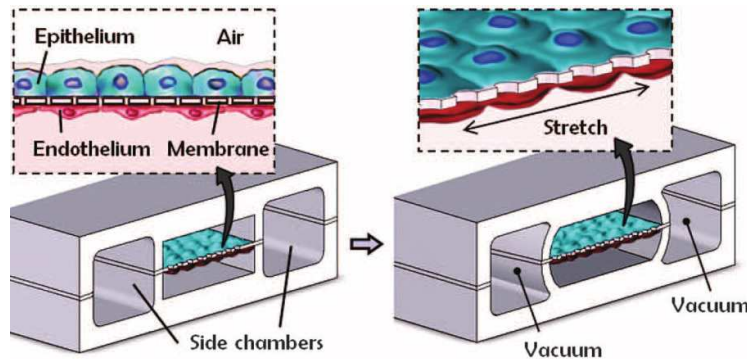


Figure 2.3: Illustration of the first Organ-on-chip, the Lung-on-chip developed by Donald Ingber [83]

Starting from this seminal work, this technology has been extensively used to study pulmonary pathology such as edema revealing the crucial role of breathing motions and the identification of potential new therapeutics [103] or inflammation and drug responses [104].

The latest version of this model was lined by human primary alveolar epithelium interfaced with endothelium to study human pathophysiology of pulmonary thrombosis, as illustrated in the *Figure 2.4*. Whole blood was used to perform quantitative analysis of organ-level contributions to inflammation-induced thrombosis and studies on the effect of toxin on the epithelium and endothelium have been studied [105].

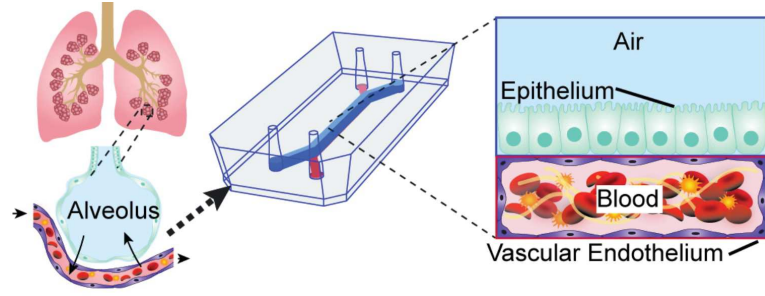


Figure 2.4: *Illustration of the last version of the pioneer Lung-on-chip [105]*

As mentioned at the beginning of this section, this first organ-on-chip model is very powerful, and quite simple looking at the fabrication protocol [106]. Therefore, it has been adapted barely two years after its first publication, to develop the first mechanically active model of gut-on-chip [84]. Only few modifications have been done to the initial design, playing with the size of the central chamber. Today, this technology is one of the most used in the organ-on-chip field allowing the study of the physiology or pathophysiology of different organs.

2.2 State-of-the-art of the Gut-on-Chip models

In the previous chapter, we have identified several key properties of the intestine, namely (1) its unique geometry, (2) its underlying complex stroma, (3) its complex interaction with the microbiota and (4) its mechanical dynamics. In the Gut-on-Chip field these properties have been targeted on their own or combined to create relevant models to study the intestinal physiology and pathophysiology. Two main strategies to develop a Gut-on-Chip can be distinguished, the first one reproduces the geometry by designing a 3D scaffold for cell culture and while the others applies mechanical forces on cells seeded in 2D to induce a 3D structure of the tissue [107]. These two strategies will be discussed in more details in the following.

Initially, the Gut-on-chip platforms are based on the use of intestinal cancer cell lines, such as Caco2 cells. These cells possess a myriad of advantages but lack some physiological properties as well as the stem ability to recreate the whole lineage of the native intestinal epithelium. This limitation was swept away by the "Organoids revolution".[108]

Organoids

The organoids term is named from the Latin "oides" that means resemblance [109]. An organoid is a miniaturized and simplified *in vitro* version of an organ produced by cell self assembly in three dimensions that mimics, at least partially, the native structure and function of the organ.

The first intestinal organoids were obtained by Sato *et al.* [110], they isolated mouse intestinal crypts and cultivated them in matrigel with a rich culture medium made of Noggin, R-spondin and EGF. Under these conditions, the isolated crypts sealed and buds appear as a reminiscence of the crypt-villus axis. These buds represent the proliferative niche, with Paneth cells and stem cells. Fully polarized enterocytes lined the inter-crypt domain, namely the villus domain, the four main cell types are scattered throughout the organoid structure and the lumen is filled with apoptotic cells [110].

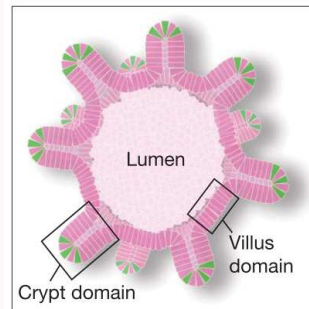


Figure 2.5:
Representation of an organoids.[110]

This spontaneous three-dimensional structure orchestrated by external factors is a faithful reproduction of *in vivo* characteristics of the gut and represents a powerful *in vitro* model. Nevertheless, the lack of relevant physical micro-environment, interplay with the stroma and their enclosed lumens limit their value for transport studies and coculture with pathogens [109]. The combination between the micro-engineered environment of the *Organ-on-chip* field and the stem cell-derived organoid technology holds great promises for disease modeling and toxicity testing as well as personalized therapy [111].

Furthermore, commercial platforms of gut-on-chip are also available such as the epithelium tissue of primary human small intestinal epithelial cells on a microporous membrane of EpiIntestinal platform or the multi-stack model with a microbial and an epithelial compartment separated by a nanoporous membrane of HuMiX, as well as the model of Mimetas inducing, thanks to a phaseguide, the formation of a barrier-free epithelial tube supporting the perfusion of medium in its center. These models "easy-to-use" represent the first advances from the academic labs to the pharmaceutical industries. Even though they are simple models, they allow to address respectively drug delivery and toxicity as well as host-microbiome interaction without any use of animal testing.

i) The 3D structured *Gut-on-chip* models

In the 3D structured approach the essential element recapitulated on chip is the unique geometry of the intestine. Several models can be found [107, 112–114], nevertheless in the following we will only discuss four examples, and how the intestine 3D structure has been reproduced on chip and how it has been used to develop biomimetic gut on chip devices. The three first models have been developed respectively by the team of John C. March [115, 116], Nancy L. Allbritton [117] and Jong H. Sung [118]. The main features of these models are summarized in the Table 2.1 while the last model relies on the use of ex-vivo intestinal fragments and will be discussed separately [119].

The three first models are based on a similar fabrication protocol. First the fabrication of a master mold reconstituting the geometry of the gut, namely the crypts and villi, is achieved using photolithography or laser ablation techniques. This first mold is then replicated to create a backing mold, most of the time in PDMS. The backing mold is the mold used to create replicate of the chip, to protect the master mold from degradations induced by the replicate process. The backing mold is again replicated to do a sacrificial mold, in either PDMS or alginate. This sacrificial mold is used to model the ECM to obtain properly speaking, the 3D scaffold used for culture. This scaffold is in poly(lactic-co-glycolic acid) (PLGA) for the first model and in collagen for the models 2 and 3. All of them are seeded with either organoids or intestinal cell line and allow to use two different media between the apical and basal compartment for biochemical gradients. Once reported the similarities of these platforms, we will discuss them more in details in order to better understand their advantages and limitations.

Model 1. The first model reproduces the villi architecture in PLGA and is covered by mouse primary cells from organoids [115]. They demonstrate that the combination of the 3D structure with a basal stimulation by growth factors, such as EGF, is essential to reproduce the spatial cellular pattern of the small intestine, including paneth cells near the base and goblet cells on the villus [116].

We can underline in this model the lack of the crypt niche for a complete reconstitution of the intestinal geometry and the poor characterization of the differentiated population, indeed the presence of paneth cells has only been justified by low quality images. Moreover, even if PLGA is biocompatible it presents biochemical and mechanical properties quite far from the in-vivo ECM.

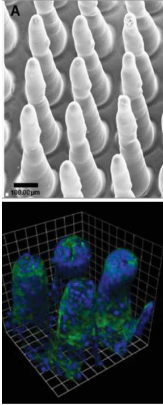
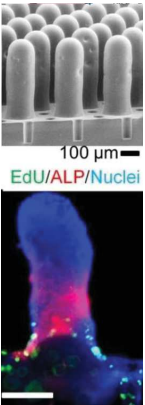
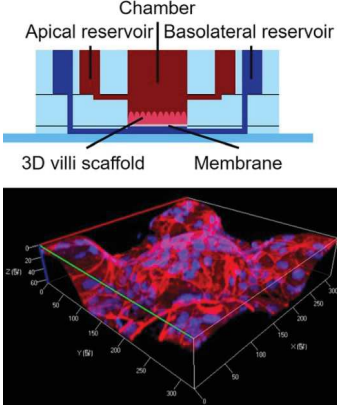
	Model 1	Model 2	Model 3
	 Blue(Dapi) Green(Actin)	 Enterocytes (ALP+)	 Blue(Dapi) Red(Actin)
Ref	[115, 116]	[117]	[118]
Mold fabrication	Laser ablation on Polymethyl methacrylate (PMMA)	2 steps photolithography	Photolithography
Scaffold	Porous PLGA	Cross-linked collagen I	Collagen I
Villi	500 µm	500 µm	100 µm
Crypt	x	100 µm	x
Cell	Mouse Organoids	Human organoids	Caco2
Culture	7 days	14 days	21 days
Gradient	✓	✓	✓
Shear stress	x	x	✓

Table 2.1: Summary of technological characteristics of three Gut-on-Chip platforms

Model 2. These limitations were overcome in the second model with a 3D scaffold made of collagen I. This scaffold contains both crypts and villi and reproduces the dimensions of the human intestine. Moreover, this structure was seeded with human organoids. They established that even though the 3D geometry helped for the morphology and differentiation of stem cells the proper cellular segregation can only be achieved thanks to the application of external chemical gradients [117]. This model allows to reconstitute important characteristics of the intestine but misses the stromal interaction, indeed the use of chemicals to cross-link the collagen scaffold is incompatible with the survival of any stromal cells in this scaffold. It is a sacrifice made by this platform to be able to fully reconstitute the 3D geometry of the intestine leading to these interesting results.

Model 3. More recently, on new microfluidic device has been developed. It reproduces two major characteristics of the gut, the 3D villi structure and the shear stress applied on the cells. The scaffold is made of collagen I and is covered with Caco-2 cells. After two weeks of culture in the chip, the villi height was reduced, by a factor 3, to approximately $100\mu\text{m}$ because of the forces exerted by cells during spreading. Anyway, they show that the combination of shear stress and 3D tissue architecture induces further physiological changes, such as a more prismatic morphology, enhanced metabolic enzymes activity (P450 3A4) and has a significant influence on the transport of drugs across the gut epithelium [118]. This last model represents a more biomimetic platform regarding the physical constraints (shear stress) but it relies on cell lines and as previously the co-culture of epithelial and stromal cells is not achieved.

Model 4. All the previous models lack the stromal compartment including the stromal cells, the immune system, the neuronal network as well as the vascularisation. To circumvent these difficulties Yissachar *et al.* designed a culture unit which can support the ex vivo culture of intestinal fragments, with two paired inputs and outputs connected either to the intestinal lumen, to allow controlled introduction of molecules or microbes into the lumen, or to the external bath to introduce continuous medium to support viability of the cultured tissue. Illustration of this platform is proposed in the *Figure 2.6*. The authors observed spontaneous peristaltic-like contractions, during the first 8 hours of culture, indicating viability of the intestinal smooth muscle layer and ENS as well as some early neuronal activation induced by a range of microbial species. However these cultures do not survive more than 24 hours without epithelial degradations [119].

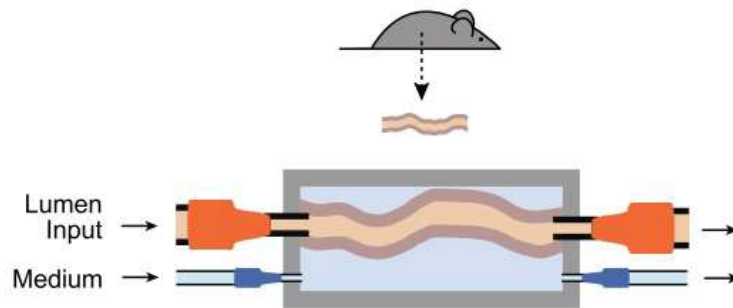


Figure 2.6: Representation of the culture unit developed to support ex vivo culture of intestinal fragments [119]

In resume the three home-made 3D Gut-on-Chip are made from a master mold, therefore the quality of this mold, in term of geometry, conditions the structure of the cells scaffold. Here, the fabrication techniques only allow the fabrication of straight geometry. As a result, all the villi are almost cylinders, no slopes are possible. Then to keep the high aspect ratio of the intestine the only solution is either to use a polymer, even though it is not biomimetic, or cross-link the ECM with chemicals.

This last solution can be discussed, indeed they start with a protein forming the native stroma (collagen I) but the use of chemicals increases its resistance but makes it toxic for cell survival. Therefore, this cross-linked collagen can still be considered similar to the native matrix ? The third model does not use any cross-link, in consequence the remaining villi are no longer physiologically relevant in terms of size. Finally, the possibility to induce a gradient between the apical and basolateral side of the cells is a real asset but, for all these models the vascularization through the stroma compartment is missing. We will now study the second strategy, where the dynamics of the intestine was the principal element to be recapitulated.

ii) The mechanically active *Gut-on-chip* models

The *Gut-on-chip* models focusing on the dynamics of the intestine, namely the peristalsis and the shear stress in the intestine, are dominated by the models developed by Donald E. Ingber [84, 106, 120, 121].

As previously mentioned, this chip was developed as a Lung-on-a-chip model then adjusted for the development of a Gut-on-a-chip where cells undergo peristalsis and shear stress, and can support growth of microbial flora [84]. The chip is composed of a central chamber subdivided in two channels (150 mm high x 1000 mm wide) by a 30 mm thick porous PDMS membrane (10 mm diameter circular pores). Two lateral channels, namely the vacuum chambers, are connected to a vacuum pump to exert cyclic mechanical strain to mimic peristaltic motions [85]. This configuration is illustrated in the *Figure 2.7*.

The first version of this model [84, 120] was used to study the influence of two physiological forces, namely the shear stress and the cyclic stretching on the intestinal barrier. To do so, the central membrane was, on the upper side, coated with an ECM solution containing rat type I collagen and Matrigel (to a ratio 1:1) and seeded with human Caco-2 intestinal epithelial cells on top of which normal intestinal microbes, *Lactobacillus rhamnosus* GG (LGG), are grown. The upper and lower channels represent respectively, the luminal and aboral side of the intestinal barrier, both are perfused with the same culture medium at a constant flow rate recapitulating the shear stress (luminal flow) undergone *in vivo*. In parallel, a cyclic stretching (10% mean cell strain, 0.15 Hz frequency) can be applied.

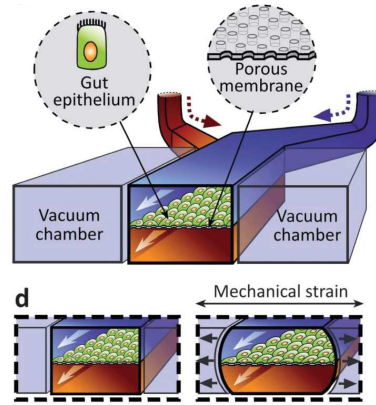


Figure 2.7: Schematic view of the adaptation of the Lun-on-chip into a Gut-on-chip by Donald E. Ingber [84]

This system allows the discrimination of the effect of the shear stress from the cyclic strain to study their individual and collective influence on the epithelium [84]. From these experiments, three main conclusions have been found:

- ***The intestinal epithelial barrier function of the gut-on-chip model is increased compare to static experiment.*** The shear stress accelerates cell differentiation, increasing the height and polarization of the Caco-2 cells, while the cyclic strain increased paracellular permeability and expression of intestinal differentiation-specific enzyme (aminopeptidases). Interestingly, measurement of the transepithelial electrical resistance (TEER) demonstrates an increase of the barrier integrity regardless cyclic strain application[84].
- ***The long term co-culture of microbes with host cells can not be achieved without cyclic straining.*** In static conditions, the influence of the microbes growing at the apical surface could not be evaluated due to the death of the epithelial monolayer. On the other hand, the epithelial cells undergoing cyclic stretching were not only able to maintain normal barrier functions under these co-culture conditions but barrier integrity measured by quantitating TEER actually improved from the one without bacteria. The cyclic strain prevents the microbial overgrowth, crucial for sustaining viable host-microbiome coexistence resulting in an increase barrier integrity [84].
- ***Under long-term cyclic strain the originally planar columnar epithelium spontaneously grew to form undulations and folds (Figure 2.8).*** Strikingly, these 3D undulating structures seem to recapitulate several properties of intestinal villi, such as the specialized-derived spatial restriction. Indeed, EdU labeled cells, namely the proliferative cells as well as the Paneth cells, have been found confined to the basal crypt-like regions between adjacent villi-like structures whereas the absorptive cells, enteroendocrine and Goblet cells produced by differentiation of the Caco-2 cells localized preferentially in the villus regions [120].

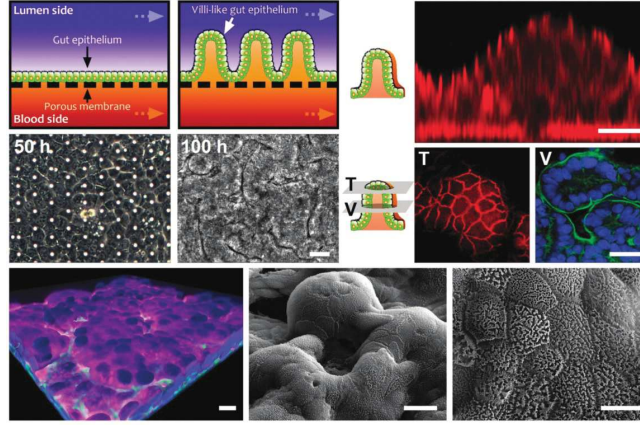


Figure 2.8: *Illustration of the villi-like structures observed in the Gut-on-chip after 100 hours of stretching [120]*

This original version was further improved to recreate the intestinal tissue-tissue interface. Therefore, the lower channel was assimilated to a blood channel seeded with microvascular endothelial cells, a more complex mixture of commensal microbes and biopsy-derived epithelium was used to better mimic the native intestinal compartment. This model ables to recapitulate the same important structural features than the "original version", including formation of elongated villi-like structures lined by a polarized epithelium expressing markers of enterocytes, goblet cells, enteroendocrine cells and Paneth cells, as well as basal proliferative cells, strong barrier function and brush border digestive enzyme activity [121].

Conclusion

If we recapitulate the efforts in the 3D side of the Gut-on-chip field, we found proofs of the influence of the topography on the cellular physiology through the increased expression of mucus, enzyme activity and differentiation. Nevertheless, the impressive achievements regarding the spatial arrangement of the proliferative and differentiated cellular compartment could not be obtained without the combination of the topography with chemical gradients. These gradients result from the separation of the apical and basal part of the chip in different channels, as a recapitulation of the *in vivo* signals emanating from the stroma. Here is the major weakness of these models. Even though the evolution from a PDMS scaffold to a biocompatible one, made of ECM-like protein, increases the relevance of these models, the lack of interaction between the epithelium and the stroma is missing to understand the underlying mechanisms in charge of the intestinal homeostasis. The attempts to recreate this cross-talk through the chemical gradients described above constitute a first step. However, the chemical cues sensed by the epithelium are secreted by the stromal cells but little is known about the multitude of proteins delivered, the cross-talk between stromal cells as well as the influence of the physical presence of these cells in the stroma.

It is from this observation that our team decided to create a 3D *Gut-on-chip* recapitulating the full structure of the intestine, crypts and villi, but adding the stromal compartment made of a collagen matrix, colonized by stromal cells (fibroblasts). This prototype was born and optimised during doctoral and post-doctoral research project of Marine Verhulsel [122]. My first year of PhD began by the formation to this complex platform, then I participated to the final improvements of the platform through fabrication by micro-milling of a more realistic 3D mold, as well as optimisation of the concentration of fibroblasts colonizing the stromal compartment and long term culture condition. The paper relating the scientific discoveries highlighted by this platform is currently under review and is the last part of this chapter.

From the other side of the *Gut-on-chip* scope, namely the active *Gut-on-chip*, the same limitation can be observed. Even though efforts have been made through the co-culture of epidermal cells with endothelial cells, the implementation of a full stromal compartment to a Gut-on-chip model remains technically challenging. Moreover, from the study of the current state-of-the-art in the *Gut-on-chip* field, it seems complicated to gather all these key properties to perfectly match the *in vivo* condition. Combinations have been tested such as topography/flow, cyclic strain/shear stress but the topography/cyclic strain seems devoid of models. It is in this gap that my own thesis takes shape, as we will see in details in the next chapter.

2.3 Development of our Gut-on-Chip platform

A biomimetic gut on chip replicating small intestine complexity

Marine Verhulsel^{1,2}, Anthony Simon², Davide Ferraro¹, Lauriane G  r  mie¹, Denis Krdnja², Laurence Talini³, Jean-Louis Viovy¹, St  phanie Descroix^{,1,#} & Danijela Matic Vignjevic^{*,2,#}*

¹Institut Curie, PSL Research University, CNRS, UMR 168, IPGG, F-75005 Paris, France

²Institut Curie, PSL Research University, CNRS, UMR 144, F-75005 Paris, France

³UPMC, Sorbonne-Universit  s, CNRS, ESPCI Paris, PSL Research University, UMR 7615, F-75005 Paris, France

these authors contributed equally to this work

Abstract

Organoids are widely used as model system to study gut pathophysiology. However they fail to reproduce the multi-component structure of the intestinal mucosa. Here we developed an original microdevice that recapitulates the topography, the molecular and cellular composition of the mucosa and the biomechanical constraints induced by the luminal flow. Each structural element was faithfully replicated; the stroma compartment was entirely made of microstructured collagen I containing fibroblasts while the basement membrane consisted in a thin layer of laminin on the collagen surface. These biomimetic features induced the spreading and organization of individual organoids seeded on the scaffold into a continuous polarized epithelial monolayer containing both proliferative and differentiated cells. In addition to its biological relevance, the flexibility of this platform was a powerful asset to identify and evaluate the relative role of different factors of the microenvironment including matrix, fibroblasts and shear stress on the epithelium organization. In particular, we demonstrated that primary intestinal fibroblasts are required to stimulate the efficient epithelialization of the scaffold while maintaining epithelial cells apico-basal polarity. Thanks to its unique features this microdevice paves the way to study epithelial-stromal interactions in gut homeostasis in normal or pathological conditions.

Introduction

The gut epithelium has a crucial role in the digestion and absorption of nutrients, while also acting as a barrier between the body and the outside world. It is the fastest renewing epithelial tissue in mammals, and the whole epithelium is completely renewed every 4 to 5 days (van der Flier and Clevers, 2009). To preserve homeostatic cell numbers, epithelial self-renewal has to be tightly regulated. Elucidating the mechanisms driving homeostatic renewal is challenging because of its complex tissue architecture, cell and extracellular matrix (ECM) composition and tissue dynamics.

Intestinal micro-topography can play an essential role in homeostasis as it underlines the spatial partitioning of cells: dividing stem cells are restricted to intestinal crypts, small invaginations that descend into the stroma, whereas differentiated cells populate villi, finger-like projections facing the gut lumen (Clevers and Batlle, 2013) (Fig. 1A). Epithelial cells are columnar and apico-basally polarized, with clear morphological and functional distinctions between the apical and basolateral sides. The basement membrane, a thin and dense sheet-like structure mainly composed of collagen IV and laminin, underlies the basal surface of the epithelium monolayer (Glentis *et al.*, 2014). It provides structural support for the epithelium, promotes cell adhesion, maintains cell polarity and has a role in the compartmentalization of the tissue by separating the epithelium from the stroma. The major components of the stroma are fibroblasts, myofibroblasts, immune cells, blood vessels and the ECM, which consists mostly of collagen I fibers. Fibroblasts play an important role in gut homeostasis by producing growth factors, cytokines and ECM proteins (Powell *et al.*, 1999), (Stzepourginski *et al.*, 2017).

Addressing the relative contribution of each of these factors in vivo remains challenging for several reasons. It is not possible to uncouple the different stromal components, high resolution imaging in the living animal is difficult and there is a need to reduce the number of animals used for research. In contrast, in vitro approaches allow an independent control of the different actors at play, in space and time. The most commonly used model, gut organoids, is derived from isolated intestinal crypts, which spontaneously form buds radiating out from a cystic luminal core after being seeded in laminin-rich hydrogel, Matrigel (Sato and Clevers, 2013a), (Sato *et al.*, 2009). Although organoids exhibit normal differentiation and localization of all types of intestinal epithelial cells, they fail to fully reproduce the crypt-villus architecture. Buds resemble the crypt regions, but the villi are represented, inadequately, by short, flat stretches of cells. In addition, due to their cystic organization there is a non-physiological accumulation of the secreted molecules into enclosed lumen. To overcome this, alternative microfluidic-based methods called gut-on-chip were devised. The pioneering one is based on human cancer cell lines (CaCo2 and HT29) growing on a porous PDMS membrane coated with ECM proteins. Under application of cyclic mechanical strain and shear stress formation

of folds resembling villi are observed (Kim *et al.*, 2012) (Kasendra *et al.*, 2018). Despite being an interesting model, the device does not fully recapitulate the complex topography of the gut and the stromal compartment is lacking. Another approach consists in growing cells on synthetic or biologically derived materials microstructured to resemble the gut topography (Costello *et al.*, 2014, Wang *et al.*, 2017). This is a major step, however, due to the nature of the chosen scaffolds all reported models suffer from several drawbacks. For example, the most commonly used material, polydimethylsiloxane (PDMS), is too stiff (0.8 to 4 MPa) and not porous (Salomon et al 2017). Biodegradable materials, such as poly(lactic-co-glycolic) acid have also been investigated however both the material mechanical and chemical features properties as well as the scaffold topography did not recapitulate the gut properties (Costello et al 2014). Finally, collagen I, the main component of the ECM, was also structured on a mold obtained by photolithography (Wang *et al.*, 2017). The main limitation of this approach is the necessity to use chemical treatment to limit structure deformation due to forces exerted by the cells that is not cytocompatible. More recently, a first proof of concept has been shown of villi like structures achieved by 3D bioprinting of collagen-based bioink (Kim et al 2018). Despite being a very active field with cutting edge technologies, none of the current gut-on-chip approaches provides physiological cell substrates that allows in particular the incorporation of a major cellular component: stromal cells.

Here, we developed a novel gut-on-chip model that reproduces the topography of the intestinal lining and, for the first time, the molecular composition of the basement membrane and the underlying stroma. This physiological/biomimetic scaffold allows incorporation of primary mouse intestinal fibroblasts that support the growth and organization of mouse organoids seeded on the scaffold into a cohesive epithelial monolayer. Thanks to this device, we have been able to make the following observations: 1) material characteristics of the scaffold determine the morphology of the epithelium; 2) fibroblasts improve epithelialization process; and 3) long-term culture requires dynamic culture conditions.

Results

Engineering a cytocompatible scaffold for gut on chip

To engineer a biomimetic relevant model system, we first replicated the composition and architecture of the mucosal extracellular matrix. Because collagen type I is the main constituent of the intestinal stroma, we developed a microfabrication strategy compatible with type I collagen molding. We choose micromilling over conventional photolithography to produce the molds, as it offers the possibility to adjust the villi slope and avoid square angles. Pushing the technical limits of micromilling we have been able to achieve molds with high aspect ratio and dimensions close to the mice gut 3D structure. We first micromilled an array of structural units on a brass master, with each unit being composed of one villus surrounded by six crypts, respecting the dimensions of the murine small intestine (Fig. 1B). Villi were 350 μm in height and 300 μm in diameter at their base; crypts were 150 μm deep and 100 μm wide with distance of 50 μm between villi and crypts.

Employing soft lithography techniques, we then produced an intermediate silicon (PDMS) replica of the brass master and used this replica to cast collagen I into structural units with high fidelity (Fig. 1C, D). Collagen hydrogels have a low stiffness that can be increased by increasing collagen concentration (Verhulsel *et al.*, 2016). To generate a scaffold that will resist cellular traction forces, we selected the highest collagen concentration that was still compatible with reproducible microstructuring, namely 10 mg/ml of native type I collagen. This corresponds to shear modulus of 1.21 ± 0.1 kPa in its polymerized state, measured by Surface Fluctuation Specular Reflection Spectroscopy (Verhulsel *et al.*, 2016).

Despite being made of highly concentrated collagen, this scaffold only partially resisted the traction forces exerted by epithelial cells. After 7 days of culture the scaffold was dramatically flatten retaining only $57 \pm 16\%$ of the original height. To preserve the 3D structure, we developed a cytocompatible cross-linking approach to achieve a scaffold able to support the growth of both stromal and epithelial cells. We selected glycation over other stiffening processes for two reasons. First, like every post-polymerization treatment, it preserves the fibrillar structure of the collagen. Second, glycation is a physiological process that normally occurs in vivo with aging, especially in connective tissues of people with diabetes (Brownlee, 2001). Thus, in contrast to collagen scaffolds treated with other cross-linkers such as glutaraldehyde or EDC-NHS (Wang *et al.*, 2017), we expected threose-treated collagen scaffolds to allow cell seeding inside the bulk. To test the cytocompatibility of the cross-linked scaffold, we added mouse intestinal fibroblasts in the collagen solution before its injection in the mold.

One day post polymerization, collagen was treated with threose at 1mM for 24h. We showed that fibroblasts retained their characteristic spindle shape and were highly dynamic, which showed that cross-linked collagen is indeed cytocompatible (Supp. Movie 1). Regarding scaffold topography, threose cross-linking limited drastically the scaffold flattening as $74 \pm 17\%$ of its initial height was maintained after 7 days of cell culture. This observation was further confirmed by rheological measurements as a 1.6-fold increase of the shear modulus was measured in threose treated collagen scaffolds compared to control.

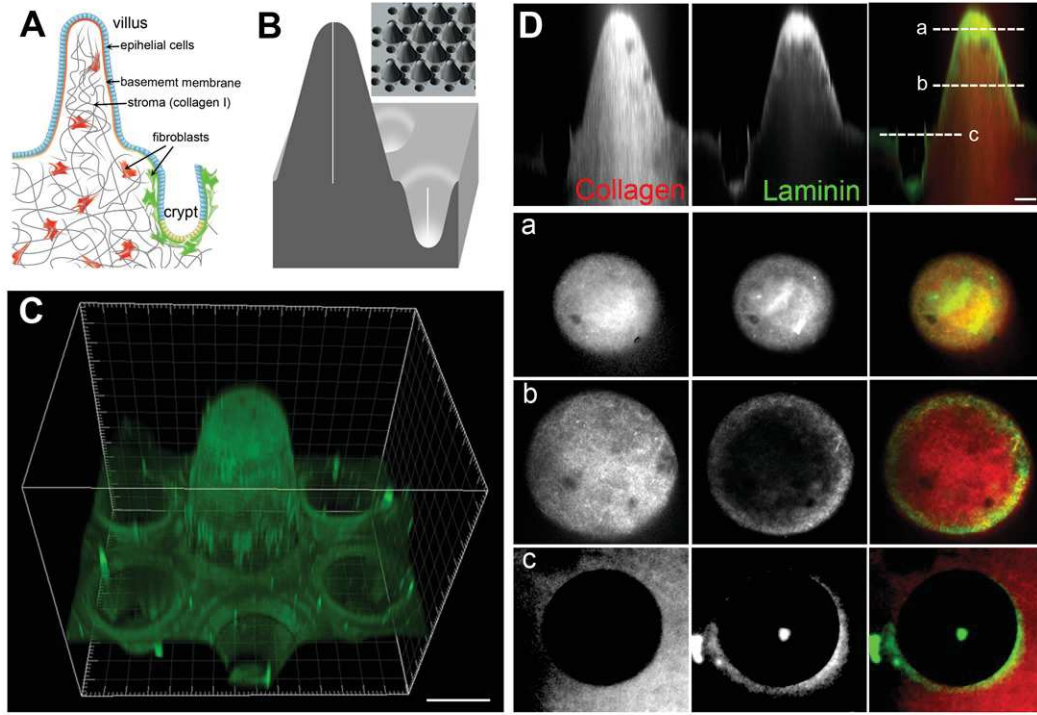


Figure 1. Engineering microstructured scaffold

A. Schematic organization of the small intestine. Simple epithelium (blue) covers finger-like projections - villi and invaginations - crypts. Epithelial cells are attached to the specialized sheet-like structure, the basement membrane. Stroma, mostly made of collagen type I (gray) contains fibroblasts (red) and myofibroblasts (green).

B. Schematics of the brass mold used to prepare PDMS intermediate mold. Villus height $350 \mu\text{m}$, crypt depth $150 \mu\text{m}$. Inset, arrays of villi and crypts.

C. PDMS mold coated with laminin (green) showing one unit consisting of a villus surrounded by 6 crypts. Scale bar, $150 \mu\text{m}$.

D. Scaffold made of Cy5-labelled collagen type I (red) overlaid with Cy3-labeled laminin (green). Side view. Cross sections at the top (a) and middle (b) of the villi and plateau (c). Scale bar, $50 \mu\text{m}$.

Reproducing the stromal compartment was the initial step but, *in vivo*, epithelial cells do not interact directly with collagen. They are anchored at their basal side to the basement membrane, which overlays the collagen-rich stromal compartment. To mimic the basement membrane, we developed a simple coating approach of the 3D collagen structures with laminin, the main component of basement membrane. We obtained a laminin coating limited to the surface of the scaffold (Fig. 1D). Altogether, thanks to cutting edge technologies of microfabrication and cytocompatible cross-linking of collagen, we have developed a biomimetic scaffold that replicates both the architecture and molecular composition of the extracellular matrix of the mouse intestinal mucosa.

Reconstitution of the gut mucosa

To direct the self-organization of cells in a coherent tissue *in vitro*, it is crucial to reproduce both the microstructure of the organ and the associated spatial partition of the different cell types (Laurent J *et al.*, 2017),(Verhulsel *et al.*, 2014). To reconstitute the intestinal mucosa and in particular the spatial segregation of epithelial and stromal cells, mouse intestinal organoids were seeded on top the scaffold while mouse intestinal fibroblasts (MIF) were embedded inside (Fig. 2A and Supp. Movie 2). Mouse intestinal organoids were cysts of around 100 μm in diameter and they were deposited into the crypt regions. Soon after seeding, organoids attached to the scaffold via actin-rich protrusions (Fig. 2i, ii and Supp. Movie 3) and started spreading on the surface while maintaining partially their 3D organization (Fig. 2B and Supp. Movies 4-5). Cells were mostly migrating collectively. The leaders of the clusters exhibited an elongated mesenchymal phenotype with broad lamellipodia-like protrusions at the migration front. Frequent exchanges of cells between adjacent organoids were also observed. Upon collision, organoids fused (Supp. Movies 4-6). At earlier time points, however, fusion was unstable and resulted in rapid cell segregation. At the later time points, when cell density was increased, fusion was stable and resulted in a cohesive monolayer (Fig 2C, Supp. Movie 7). This transition from cystic organoids to a flat monolayer resembles the wetting transitions of cellular aggregates on 2D surfaces (Doeznan *et al.*, 2012). This analogy suggests that the newly formed cell-matrix adhesions on collagen scaffold were stronger than existent cell-cell adhesions, resulting in organoid spreading.

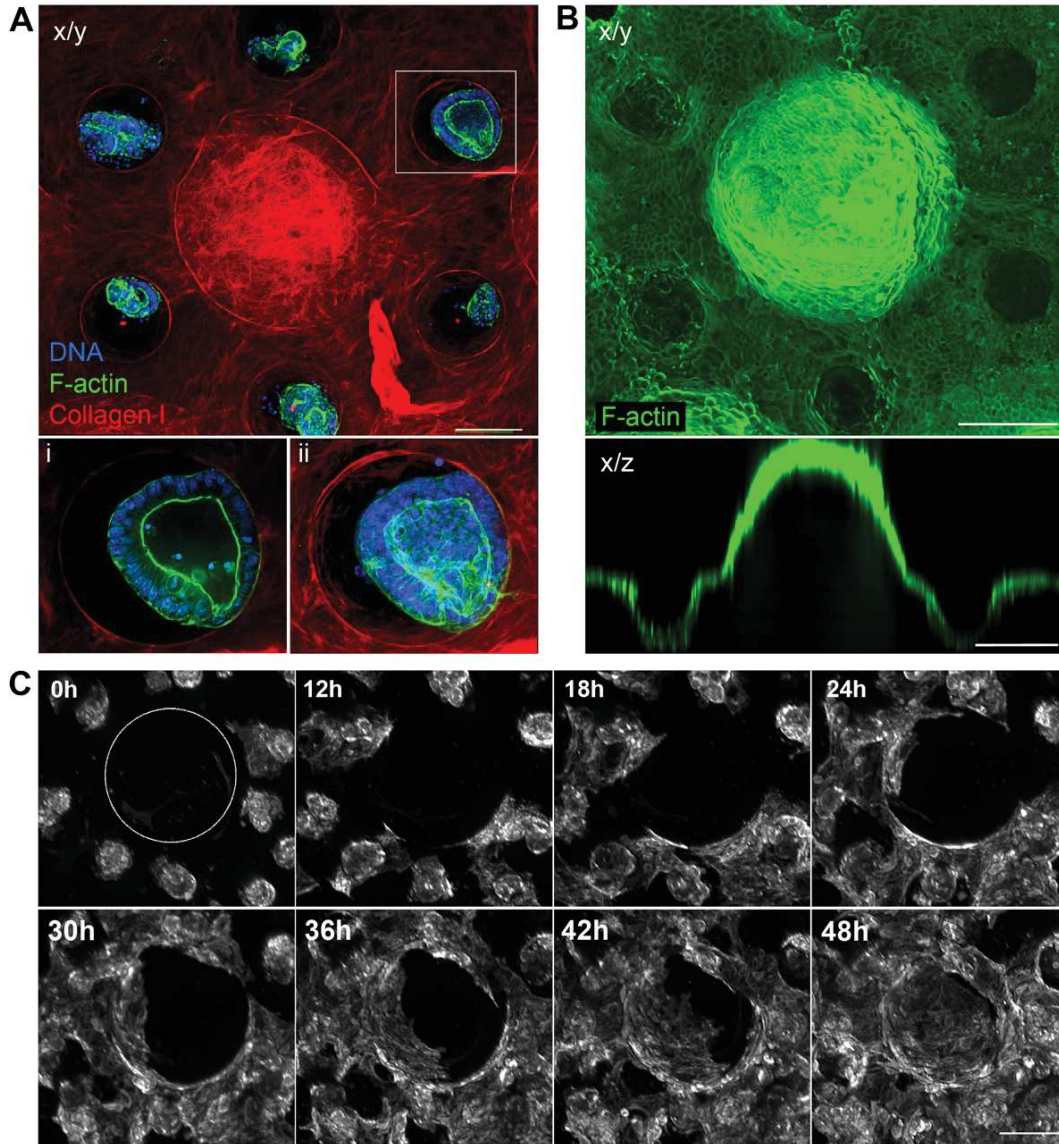


Figure 2. Epithelialization of the scaffolds

A. The unit consisting of one villus and 6 crypts. 3 hours after seeding the organoids on the collagen scaffold. Collagen type I (TAMRA-labeled, red); F-actin (phalloidin, green), DNA (DAPI, blue). Top view, maximal projection of 343 μm . Scale bar, 100 μm . Insets, higher magnification of one crypt containing an organoid. Single plane (i), maximal projection of 152 μm (ii). Scale bar, 20 μm .

B. Organoids expressing LifeAct-GFP (F-actin label) spreading over collagen scaffolds. Time in hours. Top view. Dashed line outline villus. Scale bar, 100 μm

C. Continuous monolayer of epithelial cells over the collagen scaffold four days after seeding the organoids. Top view, maximal projection of 433 μm . Scale bar, 150 μm .

Preserving epithelium integrity with dynamic culture conditions

Although cohesive monolayer was formed on the 3D scaffold, the survival of the epithelium was limited to short-term culture. After five days, patches of epithelial cells had detached, indicating that intestinal homeostasis was not maintained. In vivo, the intestinal epithelium is constantly exposed to shear stress caused by nutrients progressing throughout the gut lumen.

To mimic luminal flow on chip, one day after cell seeding, when cells were successfully adhered to the scaffold, we applied on the microdevices a shear stress about 0.09 dyne/cm^2 by placing the device in a cell culture rocking plate. This is of the same order of magnitude as the shear stress observed in vivo (Kim *et al.*, 2012). For short-term culture (up to 4 days) no significant difference was observed between static (no flow) and dynamic (with flow) culture. After five days, massive cell detachment occurred on static samples, while no detachment was observed on microdevices subjected to dynamic culture. This effect was striking after 7 days of culture. The percentage of fully covered units on static scaffolds was reduced (Fig. 3B), and the remaining epithelial cells were less cohesive, more elongated and flat, resulting in an impressive decline in the percentage of villi with polarized cells (Fig. 3C). In contrast, the integrity of the epithelium was improved on microdevices submitted to shear stress, as the area of the scaffold covered with cells expanded and epithelial cells were densely packed (Fig. 3B-C). The differences were even more pronounced at longer time points. After 14 days around 80% of the units were covered with cohesive polarized epithelial monolayer (Fig 3A-C). Together, our data show that dynamic culture conditions improve epithelial coverage and help the maintenance of epithelial integrity. This improvement could be due to the shear stress itself and/or to related effects such as nutrients mixing and oxygenation.

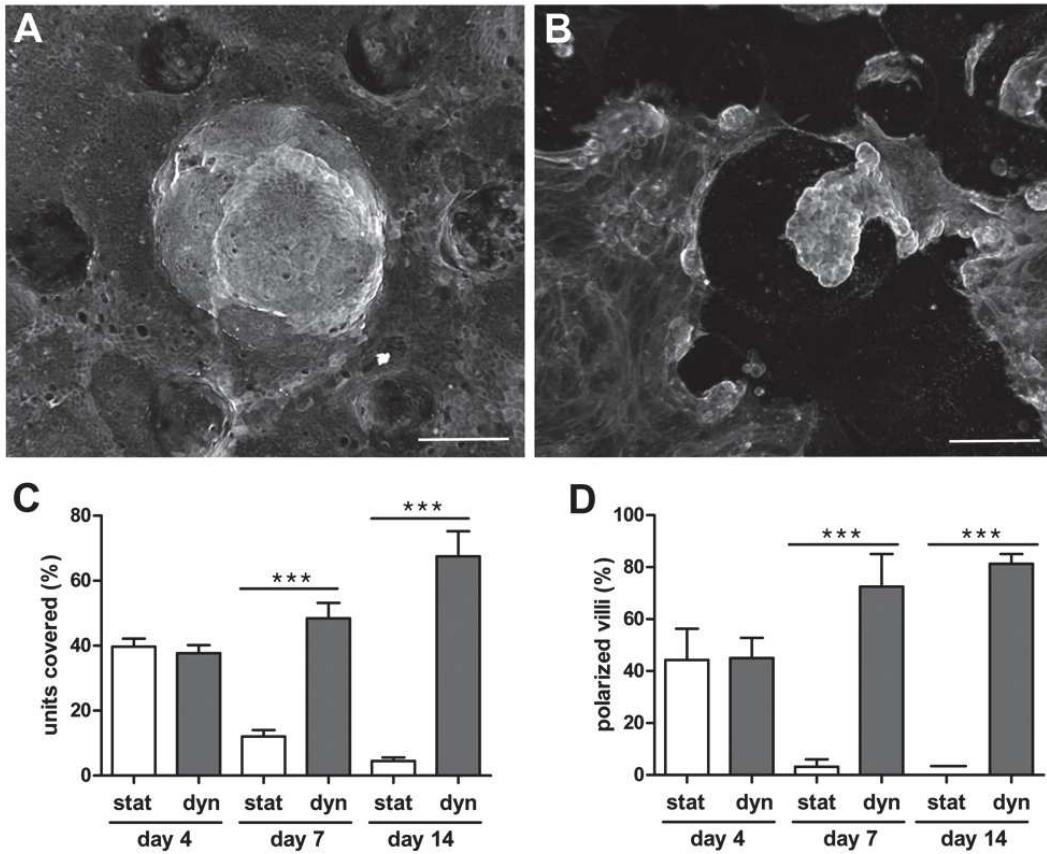


Figure 3. Shear stress improves epithelial integrity

A. Epithelial cells (F-actin, phalloidin) 14 days after seeding the organoids over the collagen scaffold containing mouse intestinal fibroblasts in the static conditions and with continuous shear stress. Top view, maximal projection. Scale bar, 150 μ m

B. Percentage of units covered with epithelial cells after 14 days after seeding the organoids on collagen scaffolds in the static conditions (stat) and with continuous shear stress (dynamic conditions, dyn). $n=128$ units, $N=3$ independent experiments. $Mean \pm SEM, t - test ***, p < 0,0001$.

C. Percentage of villi containing polarized epithelial cells 14 days after seeding the organoids on collagen scaffolds in the static conditions (stat) and with continuous shear stress (dynamic conditions, dyn). $n=128$ units, $N=3$ independent experiments. $Mean \pm SEM, t - test ***, p < 0,0001$.

Morphology and differentiation state of the epithelium replicates gut epithelium features

Our microdevice recapitulates the topography as well as the cellular and biochemical composition of the intestinal mucosa. To further validate the model, we investigated if epithelial cells on the device resemble an epithelium in the living mouse. First, we characterized the morphology of the epithelial cells. In the microdevice, the continuous cell monolayer was tightly packed with cells of hexagonal shape characteristic of intestinal epithelium (Fig. 4A, plateau). Cells were polarized, having well-defined apical domains rich in actin and nuclei oriented perpendicular to the cell base (Fig. 4A) as found *in vivo*. In addition, cells were columnar, with average width of $6.07 \pm 0.23 \mu\text{m}$ and height of $19.35 \pm 0.57 \mu\text{m}$ (Fig. 4B). To the best of our knowledge, this is the first time that epithelial cells grown on a biomimetic scaffold were polarized and exhibited characteristic hexagonal shape and dimensions similar to *in vivo*.

In vivo, intestinal stem cells differentiate in different cell types among which enterocytes, Goblet, Paneth and enteroendocrine cells (Clevers, 2013). To explore if differentiation of cells was achieved in our model, we performed immunostaining for markers specific for each differentiated cell type (Fig. 4C). The presence of functional enterocytes was demonstrated by positive villin staining. Villin was enriched at the apical pole of enterocytes, indicating mature brush borders. To identify Goblet and Paneth cells, we used a combination of Ulex Europacus Agglutinin 1 (UEA) staining, which binds to carbohydrates secreted by both Goblet and Paneth cells, and mucin 2 staining, which is specific for Goblet cells. Both, Goblet and Paneth cells were present in our model. A positive signal for Chromogranin A also confirmed the presence of enteroendocrine cells. Finally, we examined the proliferation in the microdevice. EdU labeling attested that the epithelium still contained proliferative cells after seven days of culture (Fig. 4D). We noticed, however, that the specific segregation of proliferative and differentiated cells (to crypt and villus, respectively) was not perfectly achieved. This could be due to the homogeneous distribution of fibroblasts inside the scaffold, which does not replicate the local difference in stromal composition specific to crypt and villus *in vivo*.

In conclusion, we found that cell morphology, size and differentiation state of the epithelium in the microdevice faithfully recapitulates mouse intestinal epithelium. This, together with the power of reconstituted *in vitro* models that allow independent control of all constituents, opened the possibility to investigate the influence of matrix composition and fibroblasts type on the epithelialization process.

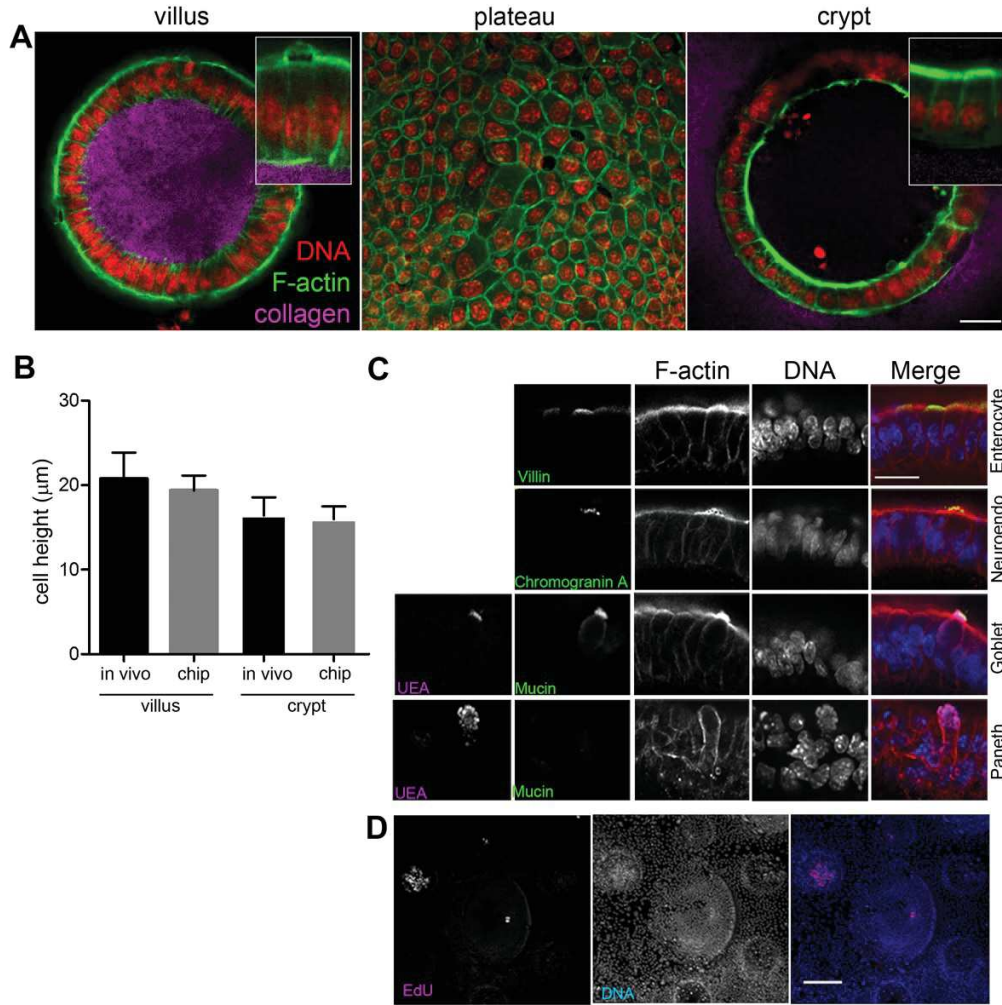


Figure 4. Cell morphology and differentiation on the microdevice recapitulate in vivo epithelium

A. Cross section through villus and crypt and top view of the region between villi and crypts (plateau) on collagen scaffolds. Collagen type I (TAMRA-labeled, pink); F-actin (phalloidin, green), DNA (DAPI, red). Scale bar, 20 μm . Inset, higher magnification of boxed region.

B. Comparison of epithelial cell height on the chip and in vivo in villi and crypts, $n=10-60$ cells, from $N=\text{chips}$ or mice.

C. Differentiation markers (green) on epithelial monolayer 4 days after seeding the organoids on the collagen scaffold containing mouse intestinal fibroblasts with continuous shear stress. Enterocytes - villin positive; Neuroendocrine cells positive for chromogranin A; Goblet cells positive for UEA and Mucin; Paneth cells positive UEA and negative for Mucin. F-actin (phalloidin, red), DNA (DAPI, blue). Side view. Scale bar, 15 μm

D. Proliferative cells labeled with EdU (pink) on epithelial monolayer 4 days after seeding the organoids on the collagen scaffold containing MIFs with continuous shear stress. DNA (DAPI, blue). Top view of the unit. Scale bar, 100 μm .

The nature of the scaffold material determines the morphology of the epithelium

First, we asked whether the epithelialization process is dependent on the nature of the material scaffold. To answer this question, we compared organoids spreading on laminin-coated collagen or PDMS scaffolds of the same dimensions. We show that even though organoids opened up and spread on PDMS scaffolds (Fig. 5A), the spreading kinetics was drastically reduced, with only 1% of units being fully covered after 4 days of culture compared with 18% on collagen scaffolds (Fig. 5B). Furthermore, the morphology of cells differed depending on the scaffold nature. Cells cultured on laminin-coated PDMS scaffolds appeared non-polarized and flat with broad lamellipodia (Fig. 5C) while, as previously mentioned, the ones grown on collagen scaffold exhibit a characteristic hexagonal shape. Because both types of scaffolds had the exactly the same topography and were coated with laminin, the differences in cell morphology and their dynamics could be only explained by the nature of the underlying substrate. These differences could result from differences in substrate stiffness: even after cross-linking, collagen is still at least 100 times softer than PDMS. Moreover, the fibrillar structure of collagen, which is absent from PDMS scaffolds, could also affect cell behavior. Altogether, these results underline the importance of the molecular nature of the matrix used as a scaffold and demonstrates that collagen scaffold was essential to induce the spreading and organization of the primary epithelial cells derived from organoids into highly polarized monolayer.

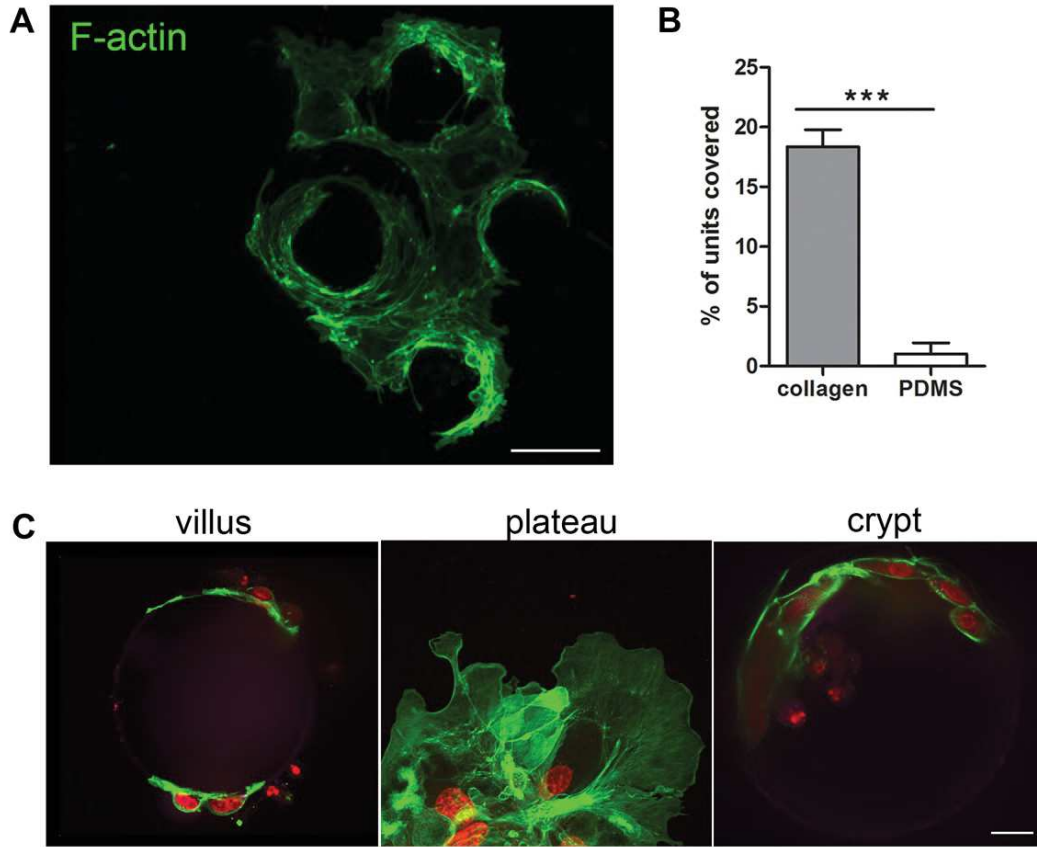


Figure 5. The nature of the scaffold material affects the morphology of the epithelium

A. Epithelial cells partially covered PDMS scaffold four days after seeding the organoids.

Top view, maximal projection of 230 μm . Scale bar, 150 μm

B. Percentage of units covered with epithelial cells after four days of culture on PDMS

and collagen scaffolds. $n=128$ units, $N=3$ independent experiments. *Mean* \pm *SEM*, *Unpaired t-test* ***, $p < 0,0001$.

C. Cross section through villus and crypt and top view of the region between villi and

crypts (plateau) on PDMS scaffolds. F-actin (phalloidin, green), DNA (DAPI, red).

Scale bar, 20 μm .

Stromal fibroblasts improve epithelial coverage

Second, we addressed the role of fibroblasts on epithelialization process. Intestine fibroblasts were isolated from the intestine of 12 days-old fluorescent reporter $\alpha SMA : mT/mG$ mice. We estimated that about 85 % of isolated fibroblasts were αSMA positive as they expressed green fluorescent protein (GFP), while about 15% were αSMA negative and expressing red fluorescent protein Tomato (figure SI supp data). A mix of both types of fibroblasts were embedded in the collagen scaffold.

After four days of co-culture with organoids, the number of units covered with epithelial cells increased as a function of fibroblast concentration (MIF) reaching about 70% for the highest concentration (Fig. 6A-C, Supp. Movie 8). In contrast, in the absence of fibroblasts the scaffold coverage was rather limited to 20% (Fig. 6C). These results demonstrate that fibroblasts markedly enhance the epithelialization process, possibly by increasing cell proliferation. However, high concentrations of fibroblasts also disrupted the apico-basal polarity of the epithelium. The proportion of villi with polarized cells dropped dramatically from over 40% to about 15% by doubling fibroblast concentration (Fig. 6D).

To determine whether the effect on epithelium coverage and polarity were specific to intestinal fibroblasts, we investigated the effect of adding fibroblasts from a different source. We isolated mouse embryonic fibroblasts (MEF), which are pluripotent fibroblasts extracted from the entire embryo. When embedded in the collagen scaffold, they increased epithelialization more efficiently than intestinal fibroblasts at the same concentrations. At high MEF concentrations, for example, more than 80% of the units were fully covered by epithelial cells, compared with 65% at high concentrations of intestinal fibroblasts (after 4 days of culture) (Fig. 6C). However, epithelial cells completely lost their characteristic columnar shape even at low concentrations of MEF, suggesting that MEF inhibit cell polarization (Fig. 6D). Instead, epithelial cells adopted a mesenchymal-like phenotype; they were elongated and flat (Fig. 6E). Conversely, epithelial cells co-cultured with intestinal fibroblasts maintained the hexagonal shape typical of intestinal epithelium (Fig. 6E). These data show that fibroblasts were not essential to initiate the spreading of the epithelial monolayer on the collagen scaffolds. However, the presence of primary intestinal fibroblasts at an optimal concentration in the scaffold is crucial to achieve an efficient epithelialization combined with physiological apico-basal polarization.

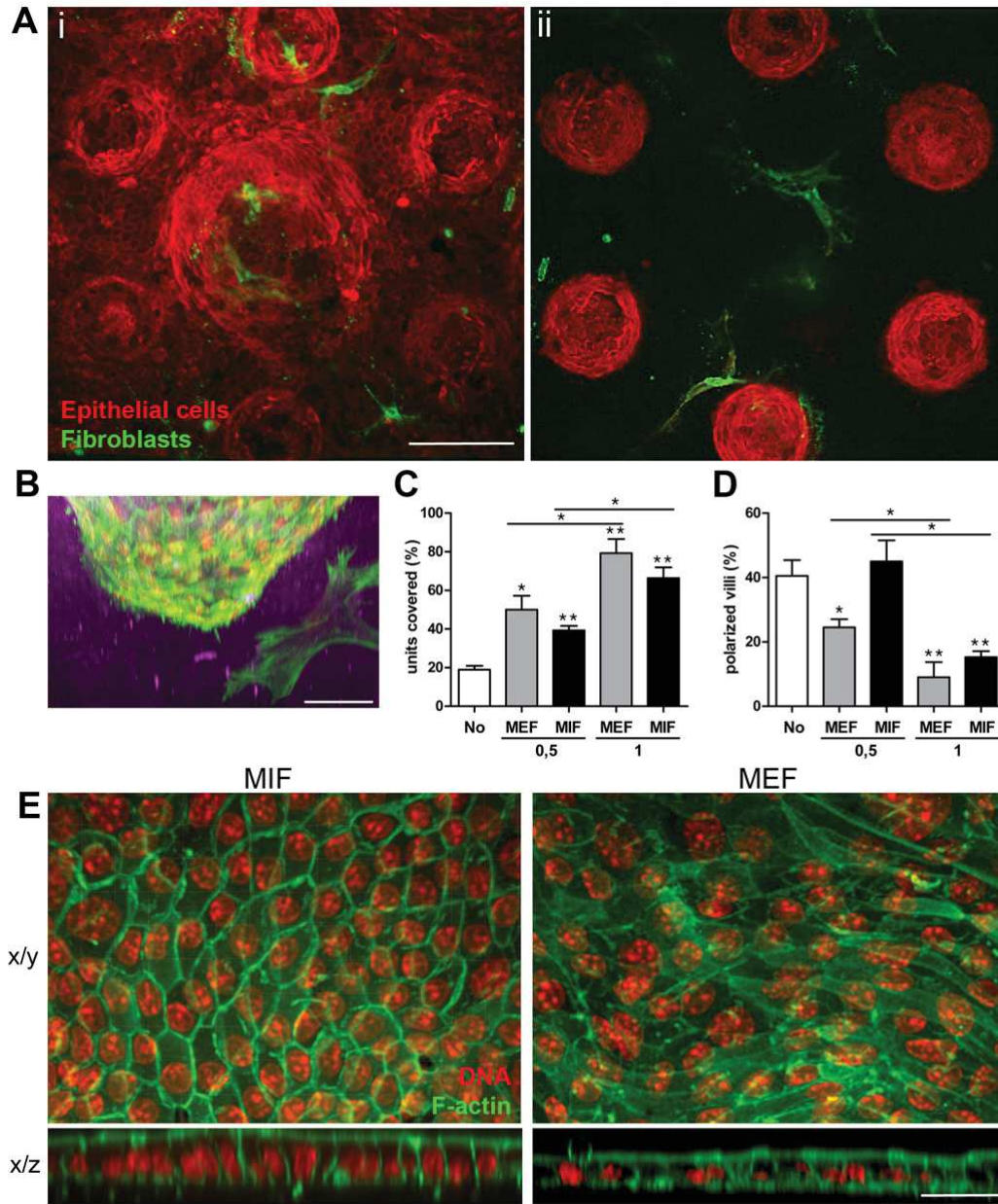


Figure 6. Intestinal fibroblasts improve coverage of the scaffold by the epithelial cells

A. Continuous monolayer of epithelial cells (F-actin labeled, red) four days after seeding the organoids over the collagen scaffold containing primary mouse intestinal fibroblasts (expressing αSMA , green). i, Top view, maximal projection of 493 μm . ii, cross section through crypt region 348 μm from the top of the scaffold. Scale bar, 150 μm

B. Side view of the crypt. Epithelial cells and fibroblasts (F-actin, green; DNA, DAPI, red), collagen (TAMRA-labelled, pink). Maximal projection of whole crypt. Scale bar, 50 μm

C. Percentage of units covered with epithelial cells four days after seeding the organoids on collagen scaffolds in the presence of primary mouse intestinal fibroblasts (MIF) and

mouse embryonic fibroblasts (MEF). Low = 0.5×10^6 of fibroblasts, high = 0.5×10^6 of fibroblasts. $n=128$ units, $N=3$ independent experiments. All bars were compared to control (collagen scaffold with no fibroblasts) or between different concentration of fibroblasts. *Mean \pm SEM, t -test $**$, $p < 0,001$; $*$, $p < 0,05$.*

D. Percentage of villi containing polarized epithelial cells four days after seeding the organoids on collagen scaffolds in the presence of primary mouse intestinal fibroblasts (MIF) and mouse embryonic fibroblasts (MEF). $n=128$ units, $N=3$ independent experiments. *Mean \pm SEM, t -test $**$, $p < 0,001$; $*$, $p < 0,05$.*

E. Top view (x/y) and side view (x/z) of epithelial monolayer on the region between villi and crypts (plateau) 4 days after seeding the organoids on collagen scaffolds in the presence of primary mouse intestinal fibroblasts (MIF) and mouse embryonic fibroblasts (MEF). F-actin (phalloidin, green), DNA (DAPI, red). Scale bar, 20 μm .

i) Discussion

Organoids are widely used as an alternative model to in vivo studies because they are easy to manipulate and closely replicate the intestinal epithelium. However, organoids grown in mouse-sarcoma-derived hydrogel (Matrigel) lack the composition and structural features of tissue from which they originate. Besides, current gut-on-chip devices lack physiological stromal components and normal epithelial morphology, and exclusively depend on exogenous morphogens in the medium.

Here, we have developed a microdevice in which we have cultured an intestinal epithelium monolayer derived from mouse organoids on laminin-coated microstructured collagen I scaffolds containing intestinal fibroblasts. Our device possesses several unique features. First, it has the typical topography of the mouse gut, consisting of an array of villi surrounded by crypts with dimensions mimicking in vivo structures. Second, our 3D scaffold is generated entirely from collagen I, the major constituent of the mouse gut stroma. To maintain the topography of the scaffold, we have developed a specific procedure to cross-link the collagen scaffold while maintaining its cytocompatibility. Consequently, this permits, for the first time, incorporation of stromal cells such as fibroblasts into the collagen scaffold. Third, the collagen scaffold is covered with a thin layer of the ECM protein laminin, mimicking a basement membrane, which is necessary for the survival and function of the epithelial cells. Seeding cystic mouse intestinal organoids on the surface results in the formation of a columnar epithelium monolayer that contains both stem cells and differentiated functional cells with morphology closely resembling intestinal epithelium in vivo. Finally, the integrity of the epithelium over two weeks is maintained by growing cell in a dynamic configuration.

Finally we showed that our device succeeds to recapitulate on chip the topography and endogenous molecular and cellular composition of the gut. Furthermore, the ability

to uncouple the contribution of different components has allowed us to highlight the importance and necessity of a physiological environment for the establishment of correct epithelial cell polarity and morphology. In particular, we demonstrate that primary intestinal fibroblasts are crucial to stimulate an efficient epithelialization of the scaffold while maintaining the morphology of the epithelial cells. We also show that the nature of the scaffold material impacts the epithelium coverage and the cells' morphology, as the collagen scaffold was much superior to the one made of PDMS.

All together, we have developed a microdevice that recapitulates mouse intestinal mucosa on the chip. The device could have a wide range of further applications. In particular, by adapting the dimensions of the device to match the size of the human crypts and villi, the device could also be used to study the pathophysiology of a human gut. For example, using epithelial cells and/or fibroblasts extracted from colorectal cancer, one could study the interplay between the stroma and cancer cells during tumor growth or invasion. Finally, the device could provide a reliable physiological pre-clinical tool for drug screening in order to replace efficiently animal models.

ii) Materials and Methods

Microstructuring collagen scaffold

Collagen I was extracted from rat tails as described previously (Schoumacher *et al.*, 2013) and labeled with Tetramethyl Rhodamine (TAMRA, Invitrogen) as described (Geraldo *et al.*, 2012, Geraldo *et al.*, 2013). TAMRA labelled collagen was mixed to non-labelled collagen in weight ratio of 1:10. The neutralizing solution (1x PBS, 10% FBS, DMEM glutamax, MEM non-essential amino acids (Gibco), 1mM sodium pyruvate (Gibco)) was prepared in another tube and pH was adjusted to pH of 7.4 with 1M NaOH. The solution of neutralizing reagent was mixed on ice and added on the top of collagen solution. The gel was gently mixed on ice with a sterile spatula to avoid bubble formation. If bubbles formed, the mixture was centrifuged at 1000g at 4 °C for 1 minute. The pH of the solution was controlled to be at 7.4 before cells were added. For scaffold containing fibroblasts, 2×10^5 cells/mL were mixed with neutralized gel before injecting into the chip. Microstructuring of collagen to replicate the 3D gut of the mouse gut, consisted of several steps. The first step consisted of creating brass mold. This was achieved by micromilling (Minitech). To maintain sterility collagen was not molded directly on to the brass but instead on to a PDMS replica prepared with PDMS (Sylgard 184, Dow Corning). The PDMS mold was made of two parts. One part (mold 1) consisted of a chamber (1cm x 2cm x 3mm) that permits both collagen injection and the handling of the collagen structure as the collagen structure was covalently grafted on the bottom part of this chamber. The second part (mold 2) consisted of a replica of gut 3D structure and was used to mold the collagen. To allow collagen

covalent bonding on the bottom of the PDMS chamber, the surface of the mold 1 was plasma activated (Plasma cleaner, Harrick). This was done by filling the microfluidic chamber with 2% v/v of 3-aminopropyl-triethoxysilan (APTES) at for 30 min. After removing the APTES solution, the chamber was washed in water for 5 min, followed by incubation in 0.5% v/v glutaraldehyde for 30 min. Finally, the microfluidic chamber was washed twice in water and incubated in water overnight at 4 °C . To prepare mold 1 for collagen injection, its lower and upper parts were punched with a 4 mm puncher. The structured area of mold 2 was plasma activated, with the area around the microstructures screened with scotch tape. This activation improved the structure wettability and decreased the likelihood of trapped air bubbles. Molds 1 and 2 were then assembled and sealed by two clips. The collagen solution was injected into the mold assembly through a Tygon tube using a conventional 1mL syringe topped with a cut pipette tip as a needle. Once the collagen had polymerized for 30 min at RT, the clips were removed and the collagen structure was unmolded. One day after unmolding, the collagen microstructures were incubated with 10 mM threose (Sigma) for 1 day. The collagen scaffold was then rinsed 3 times for 30 minutes in DMEM medium.

Laminin coating

Laminin was labelled with Cy3 as previously described (Schoumacher *et al.*, 2013). Collagen scaffolds were incubated with 0.02 mg mL⁻¹ laminin in DMEM for 30min at 37 °C . A similar protocol was followed for the plasma activated PDMS structures. Finally, in both cases, laminin solution was removed and the scaffolds were washed with cell culture medium for 5 min.

Rheology measurements

PDMS rings of 1 cm inner diameter and 0,5cm height were cut out. Two holes (Ø0,75mm, Harris Uni Core) were punched in the wall of the ring and a small PTFE tube (O.D 1,07mm, Cole Parmer) was inserted in one of them. Since the hole of the tube was too thin to directly inject the collagen with the syringe, a larger tygon tube (I.D 0,031", O.D. 0,093", Cole Parmer Instrument Company) was adapted at the end of the thin tube to avoid any leakage during collagen injection. Two pieces of PDMS (1cm x1cm) were adjusted on the top and bottom of the ring to form an enclosed chamber, hermetically sealed with two clips. Collagen solution was prepared as described above and drawn into a 1mL syringe. A 1mL cone was cut and placed at the tip of the syringe. The solution was injected through the tubing in the PDMS enclosed chamber. The collagen was polymerized at RT. Before collagen unmolding, the chamber was filled up with PBS. Immediately after the PDMS ring containing the collagen was transferred into the PBS bath. The collagen was gently detached from the PDMS ring wall. The

PBS level was adjusted to reach the limit of the upper surface of the collagen gel to prevent the collagen from drying. The collagen was not completely immersed to avoid the recording of the fluctuations of the PBS solution instead of those of the collagen gel surface. Measurements of the viscoelastic modulus of the collagen at various frequencies were performed using the technique of surface fluctuation specular reflection (SFSR). The laser beam (diameter of laser beam: 41.3 μm , 27.5 μm or 3.5 μm) was reflected by a prism and focused on the surface of the collagen gels. The surface deviated the laser beam which was reflected a second time by the prism. The reflected laser beam was collected on the center of the detector composed of a two-quadrant photodiode. The difference in voltages between the two quadrants directly quantifies the fluctuations in height of the surface of the sample. The duration of the acquisition varied from 1 to 5 minutes to investigate a larger range of frequencies. Subsequently the diagram of viscoelastic modulus vs frequency was plotted.

Crypt isolation and organoid culture

Organoid cultures were prepared as described in (Sato and Clevers, 2013b).

Organoid seeding and culture on 3D scaffold

Cystic organoids of about 100 μm in diameter (3 days after embedding in Matrigel) were extracted from Matrigel by flushing the matrix in cold PBS several times followed by centrifugation at 200g for 5min at 4°C. The pellet made of organoids was resuspended in ENR medium 300 μL of organoid solution was seeded on laminin-coated collagen or PDMS scaffolds and gently shaken to make the organoids fall into the crypts. Organoids were left to adhere for 3h at 37°C. For culture under shear stress, samples were placed on a rocking plate (PMR-30 from Grant-Bioone) one day after seeding. Rocking parameters were fixed to apply a shear stress of 0.09 dyne/cm².

Isolation of intestinal fibroblasts (MIF)

Mouse intestinal fibroblasts were isolated from $\alpha\text{SMA} : mT/mG$ transgenic mice, which were obtained by crossing a mT/mG reporter mouse (Muzumdar *et al.*, 2007) with a mouse expressing CreERT2 recombinase under the αSMA promoter (Wendling *et al.*, 2009). Fibroblasts were isolated following the procedure described in (Lahar *et al.*, 2011), with some modifications. Intestine was isolated from a 12-day-old mice and incubated for 15min in HBSS solution without calcium or magnesium, supplemented with 20mg/mL of D-glucose (Thermofisher), 1% Glutamax (v/v) and 2% Anti-Anti (v/v). Tissue was diced into 0.5mm² pieces and transferred into the dissociation solution (0.31mg/mL dispase and 0.25mg/mL collagenase XI diluted in HBSS with calcium

and magnesium supplemented with 1% Glutamax (v/v) and 2% Anti-Anti (v/v)). After 30 minutes at 37 °C under slow agitation, 25mL of DMEM Glutamax supplemented with 5% FBS (v/v), 1% Glutamax (v/v), D-sorbitol (20mg/ml), 2% Anti-anti (v/v)) were added. The solution was spun down at 100g for 2 minutes at 4 °C and the pellet obtained was suspended into HBSS with calcium and magnesium and centrifuged at 200g for 3 minutes. Tissue pieces were resuspended into 10 mL culture medium (DMEM-Glutamax) supplemented with 10% FBS (v/v), 2% Anti-Anti (v/v), 1X ITS (v/v), 50 $\mu\text{g mL}^{-1}$ EGF and placed in 10cm diameter Petri dish to adhere. Medium was changed every 4 days. After 7 days cells that escaped tissue and adhered to the Petri dish were collected. Upon treatment with 0.09 dyne/cm² 0.09 dyne/cm² 1 μM 4-hydroxitamoxifen and Cre recombination, about 85% of isolated fibroblasts were αSMA positive: they expressed green fluorescent protein (GFP) (and so could be classified as myofibroblasts, based on αSMA expression), while about 15% were αSMA negative and expressed red fluorescent protein Tomato.

Isolation of mouse embryonic fibroblasts (MEF)

Mouse embryos at stage E16 were placed in cold cleaning solution (PBS supplemented with 2% Anti-Anti (v/v)). All red organs, arms, legs and tails were removed and tissues were cleaned twice quickly into the cleaning solution. Tissue was minced into 1mm² pieces and placed into a 50mL conical tube, containing a magnetic stirrer and 5mL of glass beads (Sigma Aldrich), with 10mL of Tryple (Thermofisher). Enzymatic digestion was performed at 37 °C under agitation and 10mL of Tryple were added every 30 minutes. After 1h30, Tryple was inhibited with 6mL of FBS and samples were spun down at 200g for 5 minutes. The pellet was suspended into 50mL of medium (DMEM-Glutamax) supplemented with 20% FBS (v/v) and 2% Anti-Anti (v/v)) and placed in cell culture flasks following the dilution of 106 cells per 150cm².

Immunostaining

For EdU staining, samples were pre-incubated with 10 μM EdU (Thermofisher) for 30 minutes at 37 °C. Prior to immunostaining, the culture medium was removed and the chip was incubated in 4% PFA in PBS (v/v) for 30 minutes at RT to perform cell fixation. The chip was washed 3 times for 15min with PBS. Cells were permeabilized with 0.5% Triton X-100 (v/v) for 5min at RT. The chip was rinsed 2 times 15min with PBS at RT. 400 μL of staining solution was injected and chips were incubated 30 min at RT for EdU detection or at 4 °C overnight for protein staining. The chip was rinsed 3 times 30 min with PBS at RT. Chips were incubated with 400 μL of secondary antibody solution for 2h at RT, in the dark and then rinsed 3 times with PBS for 30 min at RT. The chips were stored at 4 °C until imaged. The list of used antibodies

could be found in Supplementary Information.

Imaging

Collagen scaffolds were imaged using an upright spinning disk (Roper Zeiss) microscope equipped with 10x/0.3NA (working distance 5.2mm) objective, 405nm, 491nm, 561nm and 634nm lasers and controlled by Metamorph imaging software (Universal Imaging). Z stack acquisitions were set to start 20 μ m above the 3D scaffold and to end 20 μ m below the 3D scaffold. Z stacks were acquired every 2 to 5 μ m. Images were processed by Image J and Imaris software.

Quantifications and statistics

For the quantification of epithelialization process, units were considered covered if villus and all 6 crypts were fully covered with epithelial cells independently of their shape. For the quantification of polarity, villi containing at least one polarized cell were counted. All experiments were performed in triplicates in 1-3 independent experiments. All statistical analysis and graphic representations were performed using Graph Pad Prism software. Data are represented as mean+/- SEM. Statistical significance was determined with t-test as indicated; *** $p < 0,0001$; ** $p < 0,001$; * $p < 0.05$.

Acknowledgements

We thank all members of the MMBM team (UMR 168) and Vignjevic (UMR144) labs for helpful discussions. We acknowledge imaging facilities PICT-IBiSA Lhomond and PICT BDD and in particular O. Leroy, O. Renaud. We also thank all members of the animal house facility. We thank Remy Fert and Eric Nicolau (UMR168) for their support in micro-milling. We thank D. Metzger and P. Chambon (Strasbourg) for their generous gift of aSMA:Cre mouse line, and C. Rosse (Institut Curie) for providing collagen labeled Cy5. D.F. thanks the ARC foundation for young researcher fellowship. This work has received the support of Institut Pierre-Gilles de Gennes (équipement d'excellence and LABEX, "Investissements d'avenir", program ANR-10-EQPX-34). This work was supported by *ERC* – 2012 – *StG*20111109 grant STARLIN (D.M.V) and *ERC**adgCellOFP7–IDEAS–ERC–321107* (J.L.V) and ANR HOME-OGUT.

Author Contributions

JLV, SD and DV conceived the study. MV and AS performed the majority of the experiments. MV developed procedures to generate microstructured collagen scaffold, to stiffen collagen, to optimize fibroblasts survival in collagen bulk at this concentration, laminin coating, image analysis. MV and AS optimized organoid protocol, cell seeding, shacking and performed imaging. AS extracted fibroblasts and performed immunostaining. DF and LG microfabricated the brass molds. LG participated in the study of the influence of fibroblasts. LT performed rheology measurements and analysis. DK performed quantification of cell dimensions. MV, SD and DV wrote the manuscript with input from all authors. DV, SD, JLV supervised the project.

References

BROWNLEE, M. 2001. Biochemistry and molecular cell biology of diabetic complications. *Nature*, 414, 813-20.

CLEVERS, H. 2013. The intestinal crypt, a prototype stem cell compartment. *Cell*, 154, 274-84.

CLEVERS, H. & BATLLE, E. 2013. SnapShot: the intestinal crypt. *Cell*, 152, 1198-1198 e2.

COSTELLO, C. M., SORNA, R. M., GOH, Y. L., CENGIC, I., JAIN, N. K. & MARCH, J. C. 2014. 3-D intestinal scaffolds for evaluating the therapeutic potential of probiotics. *Mol Pharm*, 11, 2030-9.

DOUEZAN, S., DUMOND, J. & BROCHARD-WYART, F. 2012. Wetting transitions of cellular aggregates induced by substrate rigidity. *Soft Matter*, 8, 9.

GERALDO, S., SIMON, A., ELKHATIB, N., LOUVARD, D., FETLER, L. & VIGNJEVIC, D. M. 2012. Do cancer cells have distinct adhesions in 3D collagen matrices and in vivo? *Eur J Cell Biol*, 91, 930-7.

GERALDO, S., SIMON, A. & VIGNJEVIC, D. M. 2013. Revealing the cytoskeletal organization of invasive cancer cells in 3D. *J Vis Exp*, e50763.

GLENTIS, A., GURCHENKOV, V. & MATIC VIGNJEVIC, D. 2014. Assembly, heterogeneity, and breaching of the basement membranes. *Cell Adh Migr*, 8, 236-45.

KASENDRA, M., TOVAGLIERI, A., SONTHEIMER-PHELPS, A., JALILI-FIROOZINEZHAD, S., BEIN, A., CHALKIADAKI, A., SCHOLL, W., ZHANG, C., RICKNER, H., RICHMOND, C. A., LI, H., BREAUULT, D. T. & INGBER, D. E. 2018. Development of a

primary human Small Intestine-on-a-Chip using biopsy-derived organoids. *Sci Rep*, 8, 2871.

KIM, H. J., HUH, D., HAMILTON, G. & INGBER, D. E. 2012. Human gut-on-a-chip inhabited by microbial flora that experiences intestinal peristalsis-like motions and flow. *Lab Chip*, 12, 2165-74.

KIM, W.J., KIM, G. H. 2018. An innovative cell-printed microscale collagen model for mimicking intestinal villus epithelium. *Chem Eng*, 334, 2308-2318.

LAHAR, N., LEI, N. Y., WANG, J., JABAJI, Z., TUNG, S. C., JOSHI, V., LEWIS, M., STELZNER, M., MARTIN, M. G. & DUNN, J. C. 2011. Intestinal subepithelial myofibroblasts support in vitro and in vivo growth of human small intestinal epithelium. *PLoS One*, 6, e26898.

LAURENT J, BLIN G, CHATELAIN F, VANNEAUX V, FUCHS A, J, L. & M, T. 2017. Convergence of microengineering and cellular self-organization towards functional tissue manufacturing. *nat biomedical engineering*, 1, 939-956.

MUZUMDAR, M. D., TASIC, B., MIYAMICHI, K., LI, L. & LUO, L. 2007. A global double-fluorescent Cre reporter mouse. *Genesis*, 45, 593-605.

POWELL, D. W., MIFFLIN, R. C., VALENTICH, J. D., CROWE, S. E., SAADA, J. I. & WEST, A. B. 1999. Myofibroblasts. II. Intestinal subepithelial myofibroblasts. *Am J Physiol*, 277, C183-201.

SALOMON, J., GASTON, C., MAGESCAS, J., DUVAUCHELLE, B., CANIONI, D., SENGMANIVONG, L., MAYEUX, A., MICHAUX, G., CAMPEOTTO, F., LEMALE, J., VIALA, J., POIRIER, F., MINC, N., SCHMITZ, J., BROUSSE, N., LADOUX, B., GOULET, O. & DELACOUR, D. 2017. Contractile forces at tricellular contacts modulate epithelial organization and monolayer integrity, *Nat Comm*, 8, 13998

SATO, T. & CLEVERS, H. 2013a. Growing self-organizing mini-guts from a single intestinal stem cell: mechanism and applications. *Science*, 340, 1190-4.

SATO, T. & CLEVERS, H. 2013b. Primary mouse small intestinal epithelial cell cultures. *Methods Mol Biol*, 945, 319-28.

SATO, T., VRIES, R. G., SNIPPERT, H. J., VAN DE WETERING, M., BARKER, N., STANGE, D. E., VAN ES, J. H., ABO, A., KUJALA, P., PETERS, P. J. & CLEVERS, H. 2009. Single *Lgr5* stem cells build crypt-villus structures in vitro without a mesenchymal niche. *Nature*, 459, 262-5.

SCHOUMACHER, M., GLENTIS, A., GURCHENKOV, V. V. & VIGNJEVIC, D. M. 2013. Basement membrane invasion assays: native basement membrane and

chemoinvasion assay. *Methods Mol Biol*, 1046, 133-44.

STZEPOURGINSKI, I., NIGRO, G., JACOB, J. M., DULAUIROY, S., SANSONETTI, P. J., EBERL, G. & PEDUTO, L. 2017. CD34+ mesenchymal cells are a major component of the intestinal stem cells niche at homeostasis and after injury. *Proc Natl Acad Sci U S A*, 114, E506-E513.

VAN DER FLIER, L. G. & CLEVERS, H. 2009. Stem cells, self-renewal, and differentiation in the intestinal epithelium. *Annu Rev Physiol*, 71, 241-60.

VERHULSEL, M., SHIVOKHIN S, SIMON A., DESCROIX S., C, F. & L, T. 2016. High bandwidth non invasive measurements of the linear viscoelasticity of collagen gels.

WANG, Y., GUNASEKARA, D. B., REED, M. I., DISALVO, M., BULTMAN, S. J., SIMS, C. E., MAGNESS, S. T. & ALLBRITTON, N. L. 2017. A microengineered collagen scaffold for generating a polarized crypt-villus architecture of human small intestinal epithelium. *Biomaterials*, 128, 44-55.

WENDLING, O., BORNERT, J. M., CHAMBON, P. & METZGER, D. 2009. Efficient temporally-controlled targeted mutagenesis in smooth muscle cells of the adult mouse. *Genesis*, 47, 14-8.

Chapter

3

From static to dynamic

Contents

3.1	The influence of the mechanical environment	69
i)	At the cellular level	69
ii)	At the tissue level	72
3.2	Stretching platforms, the <i>State-of-the-art</i>	74
i)	Different stretching technologies	74
ii)	Biological responses to cells stretching	80
iii)	Focus on : intestinal epithelial stretching	84
3.3	Peristalsis-on-chip	87
i)	Stretcher	87
ii)	3D stretching chips microfabrication	92
iii)	Calibration	94
3.4	Conclusion	97

Introduction

Mechanical stimuli occur on a daily basis in cell life, modulating cells functions such as migration, proliferation, differentiation and apoptosis as well as the structure, composition and function of living tissues [123–125]. These mechanical signals come from a wide variety of sources scattered in our body, through passive activation such as the substrate rigidity [126] and gravity, or active mechanical stimulation by fluid shear stress in blood vessels [127] or stretching induced by breathing. These stimulations are crucial for the homeostasis of our body, and their disruption can be involved in various pathologies such as cancer, atherosclerotic lesions or osteoporosis, related respectively to lost in the touch sensation, disturbed laminar shear stress and decreased mechanical stimulation [124, 128]. Besides this, mechanical stimulations are also involved in development. During embryogenesis the mechanical stimulations are involved in crucial developmental steps, such as the left-right body asymmetry induced by fluid shear forces [129].

In this chapter, I will first describe briefly how external forces can be internalized by the cells and trigger specific cell responses. The specific case of cyclic stretching will be then discussed both from a technological and biological point of view. Finally, I will describe the technological solution developed during my PhD.

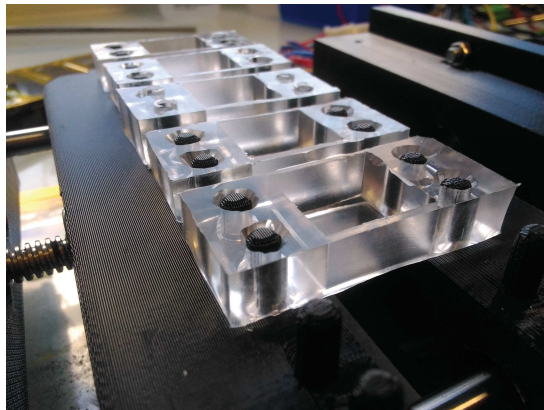


Figure 3.1: *Picture of one of the first version of the stretcher developed during my PhD*

3.1 The influence of the mechanical environment

Each cell of our body lives in a complex and dynamic micro-environment. To ensure the cohesion at a tissue level, the cells need to sense external stimuli from the substrate and from the other cells. This ability of the cells to "sense" forces is named: mechanotransduction.

*The mechanotransduction is the mechanotransmission
of forces between the outside and the nucleus
through mechanosensitive elements [130].*

The mechanotransduction is a two-way communication channel. Indeed cells receive extracellular stimuli, which are internalized through their cytoskeleton, and emit appropriate physiological responses. But they can also induce mechanical loadings on the substrate to sense the rigidity, for example [130]. This ability of cells to actively remodel and change physically and biochemically their environment is primordial for cell motility and spreading [131]. Moreover, it has been proposed recently that cells do remodel the ECM as a communication path for synchronous behaviours [132]. A striking example on how cells are impacted by the substrate properties, is the case of mesenchymal stem cells tuning their internal stiffness to match that of the substrate, resulting in a rigidity-dependant lineage differentiation [126].

In the following sections, I will discuss how cells "sense" external stimuli from both the underneath substrate and the surrounding cells.

i) At the cellular level

Cells "sense" their substrate through a direct and an indirect mechanotransduction process. The direct process is the mechanotransmission of stimuli thanks to the mechanical continuity between the ECM and the cells, ensured by the integrins [133]. The integrins are transmembrane proteins with an external domain linked to ECM ligand and a cytoplasmic domain associated to the cytoskeleton. They are the main readouts of the environment for the cells.

The indirect mechanotransduction uses membrane mechanosensors, which change their conformation under mechanical loading altering their functions, such as the stretch-activated channels (SACs), the G proteins and the receptor tyrosine kinases (RTKs) [123]. A schematic view of the main sensors of a cell is proposed in the *Figure 3.2*.

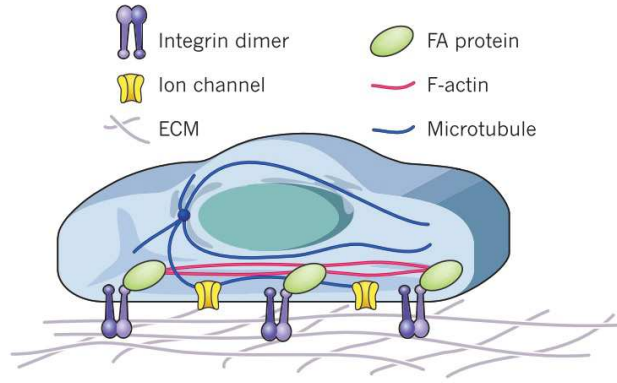


Figure 3.2: Schematic view of a cell with its main membrane detectors by Hoffman et al. [130]

Indirect mechanotransduction: the stretch-activated ion channels

The SACs termed comprises a large variety of ion channels; the degenerin/epithelial sodium channels (DEG/ENaC), the transient receptor potential channels (TRP), the two-pore domain potassium channels (K_2P) [134] and the piezo ion channels [135]. The identification of the implication of each of these channels, in the mechanotransduction, is an on going research. Nevertheless, their role in specialized sensory cells such as ear hair cells and cutaneous mechanoreceptors have been highlighted for auditory and touch sensing [136]. Along with, the SACs are implicated in substrate rigidity sensing [131], cellular reorientation [127] through Ca^{2+} traffic via SACs and stretch-dependent mitosis through Piezo 1 ion channel [137] as well as, a coupling effect with the integrin pathway has been underlined to regulate ECM protein synthesis [138].

Direct mechanotransduction: the structural connexion

The connexion between the ECM and the cell is an essential instructional pathway, it relies on several elements and can be sum up has following:

$$ECM \rightleftharpoons Integrins \rightleftharpoons Focal\ Adhesion \rightleftharpoons Cytoskeleton \rightleftharpoons Nucleus$$

The integrins are heterodimers transmembrane proteins, composed of an α and a β subunit, restricted to the metazoa. So far, 24 combinations have been identified in mammalian from the assembly of 18 α and 8 β subunits, as illustrated in the *Figure 3.3*. Each of these combinations appears to have a specific, nonredundant function and is able to recognize specific sites in the ECM, called ligand, such as the tripeptide sequence RGD (present in fibronectin) or laminins [139].

Finally, the actin regulatory layer contains zyxin, a LIN-11, Isl1, and MEC-3 (LIM) domain proteins acting as a cytoskeletal adapter triggering local recruitment of α -actinin and vasodilator-stimulated phosphoprotein (VASP) to stabilize the elongation and reinforce stress fibers [146, 147].

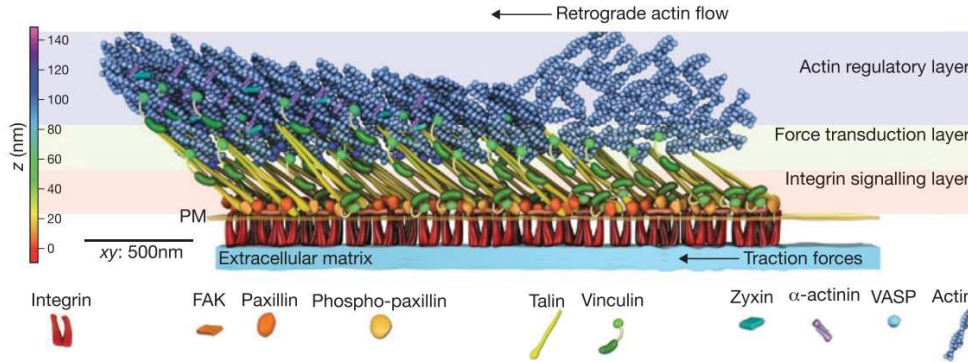


Figure 3.4: Structure of the focal adhesions from Case *et al.* [145]

Here, the focus has been made on the main mechanosensitive proteins composing the FA, but more than 150 proteins are recruited and understanding their function and interplay is an ongoing research field [125]. The FA assembly is the first cellular response to external stimuli, followed by genetic activation or ECM synthesis possibly helped by SACs [148]. It represents one way for a cell to adapt and respond to substrate stimulation, we will now see how cells respond to stimulation emanating from other cells.

ii) At the tissue level

In cohesive tissues, such as epithelium or endothelium, the tissue mechanical properties can not be defined as the sum of the individual property of its constituents, i.e. the cells. A study of a cell monolayer of Madin-Darby Canine Kidney (MDCK) measured its stiffness compared to individual cell rigidity and found a value two order of magnitude larger. Moreover, the separation force for cell doublet is nine times lower than the one evaluated from monolayer measures [149]. These differences rely in particular on the formation and maturation of active intercellular junctions.

In epithelium tissue, the cell-cell junctions have three main functions, sealing of the plasma membrane of adjacent cells to ensure the barrier function of the tissue, connection of the cytoskeleton of cells to promote integrity of the tissue in response to external stress and communication between cells to mediate passage of chemical signals [150]. This functional diversity reflects the morphological diversity of the cell junction in epithelial cells. In the following I will briefly introduce the general form of a cell-cell junction, then described some of them implicated the cellular response to mechanical stimulation.

Cell-cell junction

The cell-cell connexion is a spring composed of elements with variable responses to mechanical stimulation, namely mechanosensors [151]. Despite the variety of intercellular junctions, a unique binding chain has been identified forming the cadherin–catenin core complex (CCC) [152], composed of:

$$\text{Cadherin} \rightleftharpoons \text{p120 catenin} \rightleftharpoons \beta\text{-catenin} \rightleftharpoons \alpha\text{-catenin} \rightleftharpoons \text{F-actin}$$

This central link is the base of the cell-cell junction formation, namely the punctuate morphology. The stability of this link is tension-dependant, acting as a catch bond, it reinforces its lifetime under force by conformational stabilization and proteins recruitment to the F-actin site [153]. These stabilization and maturation processes induce the extent of the lateral distribution of cadherins to form linear adherens junctions [154]: such as the zonula adherens (ZA), also known as adhesion belt, and the desmosomes [151]. These two conformations, punctuate and linear adherens junction, are illustrated in the *Figure 3.5*.

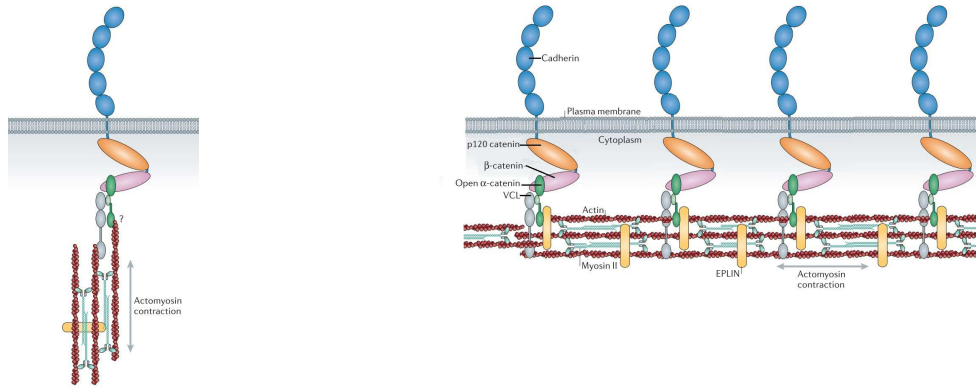


Figure 3.5: Representaion of the punctuate (left) and linear (right) morphology of cell-cell junction adaptated from Takeichi et al [152]

The formation of these adherens junctions establishes tissue tension through two complementary supracellular cytoskeletal networks [149]. The ZA bind the actin cytoskeleton of neighboring cells, setting the tissue tension, and the desmosomes bind keratin intermediate filaments governing the maximal deformation a tissue can withstand before failure [155]. The cells continuously rearrange the junctional network providing mechanical strength and tissue fluidity [156].

Moreover, the formation of tight junctions establishes a physical barrier between the apical and basolateral domain, sealing neighboring cells together [157]. This junction can be altered in order to permits flow of solutes, called paracellular transport, important for absorption of amino acids and monosaccharides from the lumen of the intestine [150].

3.2 Stretching platforms, the *State-of-the-art*

One of the first experiment using cyclic stretching, was performed in 1976 by Leung *et al.*, demonstrating the increased synthesis of ECM constituent by cyclically stimulated arterial smooth muscle cells [158]. In doing so, they demonstrated that external physical stimuli similar to chemical cues can induce a cellular response, premise of the mechanotransduction. Ever since, the number and diversity of cyclic strain experiments exponentially increases [123], multitude of cells have been studied such as mesenchymal stem cells, fibroblasts, muscle cells or endothelial cells. From these experiments both, common and unique responses can be extracted and will be discussed in the following, as well as the technological solutions developed to generate a dynamic biological environment.

The cyclic stretching is an asset for biophysics studies as well as, a promising solution for the generation of new grafts called the constructs. Constructs can be gelatin sponges [159] or decellularized tissue [160, 161], used as 3D matrix for cellular seeding. It has been shown that application of cyclic stretching on these matrix increases the cellular penetration and organization as well as, the differentiation of embryonic stem cell and bone marrow stromal cell in matured cardiomyocytes [159, 160] and toward tenogenic differentiation [161], respectively. Moreover, cyclic stretching also increases tissue vascularization [162] improving integration upon implantation [160, 162], getting closer to the generation of implants similar to native tissue. To apply cyclic stretching on cells different technological solutions can be used.

i) Different stretching technologies

A stretcher must deliver an adapted elongation to the cells depending on the cell type requirement and the physiology or pathology studied. Therefore, it has to be tunable in terms of frequency and amplitude as well as, compatible with culture conditions (inside an incubator). The elongation by itself can be uniaxial, biaxial or radial and constant or cyclic. In the following, only the cyclic stretching will be studied as it is the one we have been interested in during the PhD.

How to build a biocompatible stretching device ?

The almost unanimous response to this question is the use of a PDMS membrane. This soft, elastic (Young modulus : 2MPa), biocompatible and permeable to gases silicone elastomer, widely used in Biology and Biophysics, is a first choice of substrate for stretching applications [121, 128, 138, 159, 161, 163–183].

To stretch this silicon membrane two main strategies are currently used: the pneumatic and mechanical actuation, and will be described in the following [184]. Nevertheless, more exotic actuations have also been developed such as optical, electrothermal or dielectrophoretic ones for example [184].

The pneumatic actuation is the most popular technological solution. It can be direct, through positive or negative pressure that deforms the membrane on which cells are grown, or indirect by deformation of annex chambers linked to the deformable membrane.

- Direct deformation examples are illustrated in the *Figure 3.6*. The first example (*Figure 3.6 (a)*), can be seen as a balloon inflating under pressure, therefore stretching the cells seeded on the membrane. This device allows the application of a force on a cell or a specific area of its membrane. It is a tool to study mechanosensing at local scale, such as intracellular calcium influx [185] but is unable to produce a large homogeneous radial strain profile required to study tissue behavior. To overcome this limitation, a piston-like solution (*Figure 3.6 (b)*) was implemented to increase the area of the central homogeneous deformation. Therefore adapted to study mechanosensing for a group of cells [186, 187].

Nevertheless, this solution requires the use of lubricant between the piston and the culture film to decrease the frictions and the induced degradation of the culture film to enhance its lifetime. It is a questionable choice in term of possible contaminations and diffusion through the porous PDMS membrane restricting these technologies to local, short-term study of mechanotransduction.

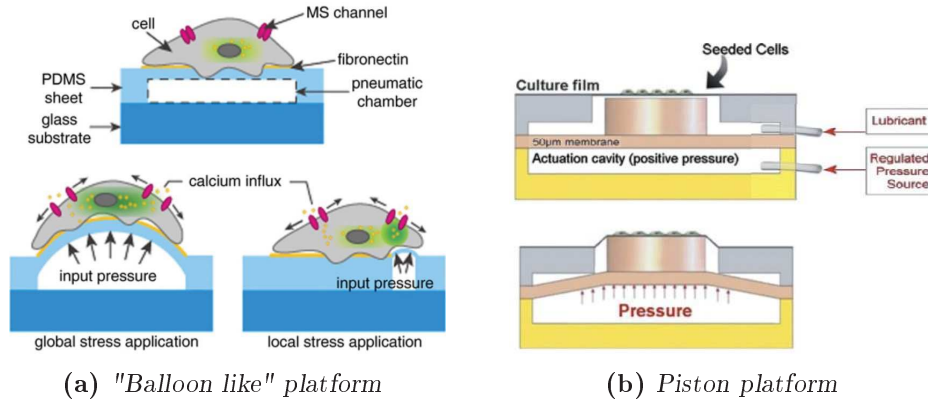


Figure 3.6: Schematic view of the chips developed by (a) Iwase *et al.* (adaptated from [185]) and (b) Moraes *et al.* (adaptated from [186])

- Indirect deformation is commonly used, commercial platforms are available, such as the one widely used in biophysics: Flexercell system (FlexCell International, PA) [128, 163, 167, 168, 179–182, 188–190]. This versatile platform allows uni- and bi-directional stretching using vacuum pressure to deform a circular elastic membrane on which cells are seeded (*Figure 3.7 (a)*). Along with, the popular *home made* model developed by Dongeun Huh and Donald Ingber in 2010 [83], it is an ingenious device allowing the stretching of a central membrane attached to side chambers submitted to negative pressure, as well as, shear stress and chemical gradients through the bottom and top channels (*Figure 3.7 (b)*). This pioneer platform has been duplicated and adapted for biaxial strain field [191] or combined into a multistretcher array [192].

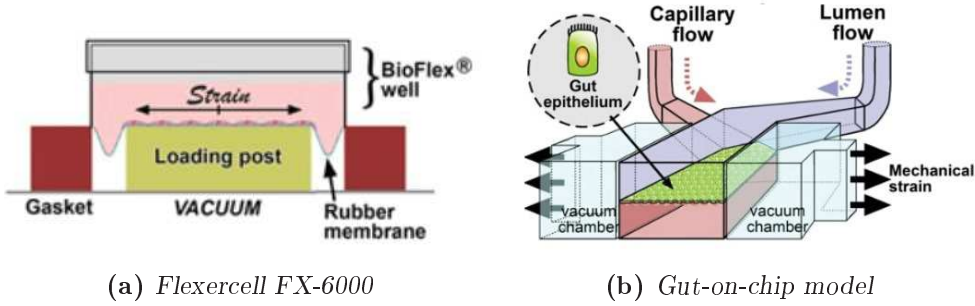


Figure 3.7: Schematic view of (a) the Flexercell system (<http://www.flexcellint.com/FX6000T.htm>) and (b) the chip developed by Dongeun Huh and Donald Ingber (adaptated from [120])

These platforms proposed an elegant solution to the previous restrictions regarding the small homogeneous area of stretching, they are perfectly adapted to studies at tissue scale. Nevertheless, fragility and complexity can be a concern, indeed the central membrane need to be as thin as possible ($\sim 10 \mu\text{m}$) to allow stretching with reasonable pressure, which increases possible manufactured defects over the complex protocol of Huh *et al.* [83]. This limitation can be overcome by the commercial platform, meanwhile losing the possibility to apply chemical gradients.

In brief, these platforms are suitable to study the influence of stretching on 2D tissue, with the possibility to study the co-effect of stretching versus flow. Nevertheless, the impossibility to tune the substrate geometry and properties, is a major limitation knowing the great impact of substrate stiffness on cellular differentiation [126] for example. Moreover, the need for an external pressure controller can be considered as non friendly-user and increases the complexity of this solution. All these platforms are based on pneumatic actuation, we will now focus on an alternative: the mechanical actuation.

The mechanical actuation can be either direct through micro-manipulators deforming the membrane on which cells are growing, or indirect using intermediate chips linked to linear translator.

- The direct deformation, even though is common for cell manipulation, such as micropipettes [184], is pretty rare at larger scale. The following examples are based on the deformation of the membrane by a narrow bump on a dynamic, piezoelectrically actuated [193], or stationary way [137]. These platforms, similarly to the previous "piston platform", possess a limited area of homogeneous stretching. The platform developed by Kamotani *et al.* studied few cells and is build as an array to allow parallel stretching for higher throughput screening. Therefore, it could be an appropriate solution for pharmacological studies for example.

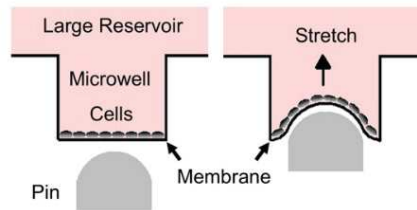


Figure 3.8: Cells cultured on flexible membranes at the bottom of the microwells stretched by the pin movements upward [193]

- Indirect deformation, on the other hand is widely used through commercial platforms such as the Strex Systems (STREX Inc.) [165, 172, 174] or *home made* ones [166, 170, 175, 194, 195]. All these platforms possess the same functioning, one fixed part and one translated part or two translated parts, the PDMS chip being attached between them and the linear motion of the translation stage is transferred to the substrate and results in the chip stretching (*Figure 3.9 (a)*). Another alternative, less common, is to induce stretching of the membrane through the vertical movements of the sides on which the extremity of the membrane is attached (*Figure 3.9 (b)*), similar the the Flexcell technology.

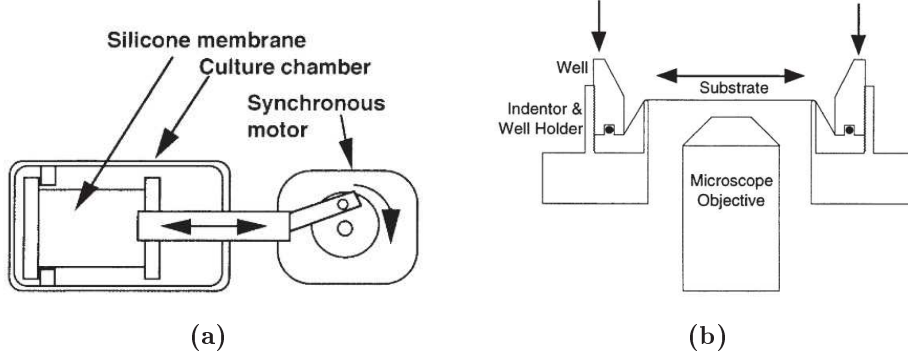


Figure 3.9: Schematic view of the mechanical principle of stretchers developed by Hayakawa *et al.* (a) [169] and Tschumperlin *et al.* (b) [196]

- Some platforms propose stretchable chips with peculiar shape such as the "V shape" of Deguchi *et al.* [195]. This geometry confines the cells within a rectangular cell culture area with a high-aspect ratio of $\sim 200 \mu\text{m}$ in lateral length (to be stretched) and 18 mm in longitudinal length, to induce a homogeneous strain on the cell culture area (Figure 3.10 (a)). Moreover, chips have been fabricated with channels parallel or perpendicular to the stretching direction, to impose one direction on the cell and maximise the effect of the stretching, to induce axon outgrowth [194] or tenocyte differentiation [197]. Besides the technological process developed by Ahmed *et al* [166] allows the study of the co-effect of the contact guidance and the stretching by patterning cell-adhesive lines of fibronectin, using micro-contact printing, with different orientations relative to the strain direction (parallel, perpendicular or oblique), Figure 3.10 (b).

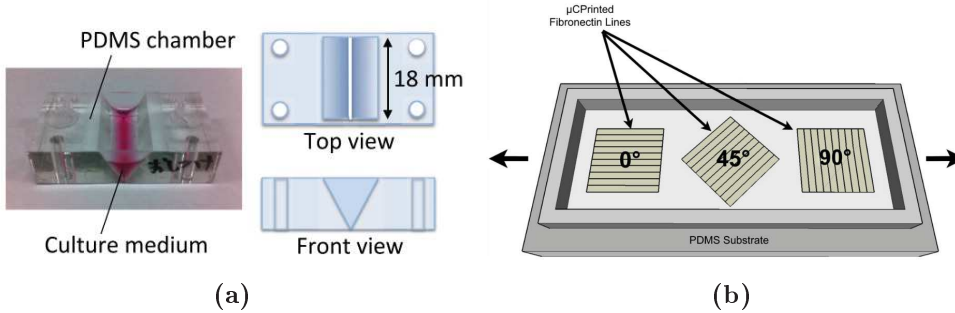


Figure 3.10: Schematic view of the chips developed by Deguchi *et al.* (a) [195] and Ahmed *et al.* (b) [166]

The mechanical actuation allows more versatility regarding the substrate geometry, however it usually remains a PDMS sheet, to fulfill the elastic property required to apply stretching. The lack of the compartmentalization, to control medium composition over time, is a major disadvantage compared to pneumatic actuation. Nevertheless, the important number of *home made* versions underlie its simplicity regarding the fabrication, calibration and every day use as well as, its possibility to tune chips geometry.

It is the solution that I chose to implement for my own stretcher that will be described in more details in the last section of this chapter.

ii) Biological responses to cells stretching

Interestingly, regardless the cellular diversity and stretching conditions differences, common cell responses to stretching emerge [123]. Among them we can cite the cells **morphological changes**, such as cellular reorientation [165, 166, 168, 169, 171, 172, 174, 176, 189, 198] being observed few minutes after the beginning of stretching, and **transcriptional activation** observed few hours later such as modulated cellular proliferation [127, 167, 173, 199–202] and differentiation [138, 163, 164, 172, 203, 204]. My PhD project being dedicated to the study of the cyclic stretching I limited this study to the cellular responses induced by cyclic stretching, mainly for cellular layer.

Morphological transformation

Under cyclic stretching, regardless frequency and amplitude, an universal cell response has been observed across cellular diversity; the cell reorientation for single cell and in tissue studies. This reorientation has been investigated with a wide range of cell types and in different stretching conditions. However it has been shown that in most of the studies cells reorient perpendicularly to the stretching axis. It has been shown in particular with smooth muscle cells [168], endothelial cells [174, 176, 189] (Figure 3.11), fibroblasts [171, 172] and myofibroblasts [166].

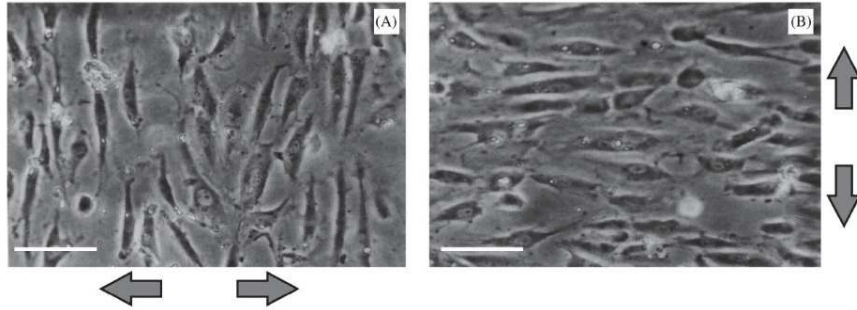


Figure 3.11: *Orientation of endothelial cells under uniaxial cyclic stretching (0.5 Hz, 3h, 10%) adapted from Wang et al. [176]*
Scale bar = 100 μ m

The cell orientation perpendicular to the stretching axis is driven by a dissipative process to relax the passively stored elastic energy [198], through disassembly of the stress fibers in the stretch direction and assembly of new fibers oriented in the direction of lower stress [171]. This cytoskeleton reorganization requires reactive oxygen species (ROS) which control actin dynamics, namely reorganization and contractility, through activation of proteins, such as cofilin [168], and actin-myosin interaction [175]. Moreover, this reorganization induces the modulation of the FAs assembly / disassembly through small GTPase Rho activation at cell-substrate [189] and cell-cell [174] adhesion site as well as, calcium influx through SAC [169].

Besides the main observation of cell reorientation perpendicular to the stretching axis, diagonal and parallel orientation to the stretching axis have also been observed with endothelial cells [169, 176], cardiomyocytes [159, 160] and bone marrow cells [161]. This divergence can be explained through the nature of the stretching. Indeed the work of Wang *et al.* [176] has shown that purely uniaxial stretching induces perpendicular reorientation whereas simple elongation induces diagonal reorientation.

Moreover, substrate mechanical properties can induced opposite responses. Indeed, the work of Tondon *et al.* [177] has shown that similar cells subjected to cyclic stretching will either align parallel or perpendicular to the stretching direction depending on the stiffness of the substrate materials. They align perpendicular while grown on stiff substrate (collagen-coated silicone rubber membrane) and they align parallel while grown on soft substrate (500 μ m-thick collagen gels). To get rid of cell type-specific response, the experiments were repeated using osteosarcoma cells and human mesenchymal stem cells subjected to 3 h of 10% cyclic uniaxial stretch at 0.01 Hz, 0.1 Hz and 1 Hz. The same observations was done; the cellular reorientation is substrate-stiffness dependent.

Transcriptional activation

Besides cells reorientation that have been observed (in few hours), another cell response to stretching can be the activation of some specific signalling pathways with a myriad of induced effects that depends on cell type and the time of stimulation.

Proliferation vs. apoptosis

Interestingly, cyclic stretching can active in a same cell type, pathways related either to cellular proliferation or apoptosis. For instance stretch-induced proliferation and apoptosis have been observed in vascular smooth muscle cells [167, 199–201], fibroblasts [187, 205] and endothelial cells [127, 202] depending on the stretching characteristics (amplitude, frequency).

For vascular smooth muscle cells (VSMC) a proliferative response has been observed for physiological stretching [199], whereas pathological stretch induces either hyperproliferation resulting in atherosclerosis [201] or apoptosis leading to inflammatory cell infiltration into the subendothelial layer of the vessel wall [127]. Therefore, the stretching amplitude can induce different responses for a same cell type.

Moreover, the response to the stretching of a single cell is different from the one of a monolayer modulated by cellular junction. Therefore, the fact that cyclic stretching decreases endothelial cell proliferation may serve to stabilize the integrity of vessels [202], whereas single cells will proliferate and spread in a time-dependent manner [173, 205]. Also, pathological stretch has been observed to disrupt the tight junction structure in alveolar epithelium, therefore increasing the permeability of the tissue [178].

An other consideration to take into account is the age of the cells, indeed embryonic versus mature cells are not supposed to react the same way to mechanical simulation. For example the hypoplastic left heart syndrome (HLHS), which corresponds to an insufficient size of the left ventricle seems to result from the disruption of biomechanical stimuli *in utero*. The work of Banerjee et al on embryonic mouse cardiomyocytes (EMCMs), subjected to cyclic stretching, demonstrates a stretch-dependent increase in both proliferation and size as well as, a decreased expression of TGF- β signalling responsible to repress both EMCs contractile force and beating [206]. This work underlines the key role of mechanical stimuli in embryonic development and differentiation.

Cellular differentiation

To test the influence of cyclic stretching on differentiation, mesenchymal stem cells (MSCs) have been widely used, for osteogenic [128, 163], tenocyte [164], chondrogenic [138] and smooth muscle cells [204] differentiation. All of these studies underline the beneficial effect of the stretching onto the differentiation process, either by up-regulation of smooth muscle α -actin specific to smooth muscle cells [204] (Figure 3.12) or by a stretch-induced increase of the rate of glycosaminoglycans synthesis, a major component of cartilage [138].

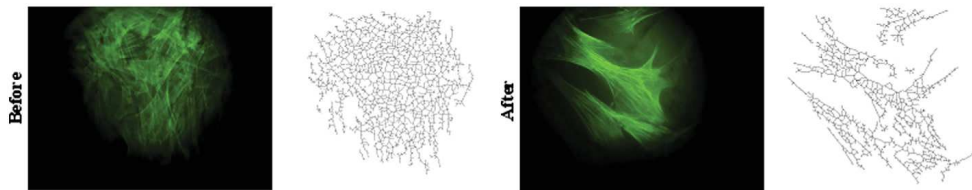


Figure 3.12: *F-actin filament reorganisation under cyclic stretching (1 Hz, 2h, 15%) adapted from Ghazanfari et al. [204]*

Moreover, optimized and tissue-specific stretching conditions can induce increased gene expression and protein synthesis levels, such in the case of tendon where the differentiation is strongly associated with the stretching [164]. Furthermore, the work of Morita *et al.* investigated the combination of microgrooves parallel to the cyclic direction to force the cells to stay in the direction of maximum elongation. Doing so, they optimized the differentiation process of mesenchymal stem cells to tenocyte conduction decreasing the differentiation time from more than 48 hours to 10 hours [165]. The stretching influence onto the differentiation process is tissue-dependent, it can be a major actor as in the previous example of MSCs-to-tenocyte differentiation or a mediator. Indeed, for osteogenic differentiation the stretching enhances BMP9-induced osteogenic differentiation and bone matrix mineralization but does not induce alone this differentiation [163]. Meanwhile, stretching increases the endogenous ROS production, which significantly decreases the osteogenic differentiation, especially in MSCs from older rats compared to young animals, suggesting a possible mechanism of age related osteoporosis [128].

Table 1 summarized different cell responses to stretching and illustrates the diversity of these cell responses. Even though some common responses have been observed, they can not be taken as a general rule, indeed the stretching response seems to depend on a combination related to the cells types, the stretching characteristics and the substrate properties.

Cell type	Stretching characteristics				Observations	Ref
	Type	Dur.	Amp.	Freq.		
Mesenchymal stem cells	/	2h	2.5%	1Hz	(l) ↗ of the osteogenic differentiation	[128]
	/	12h	6%	1Hz	(l) ↗ BMP9-induced osteogenic differentiation	[163]
	Uniaxial	1-48h	5%	1Hz	(l) ↘ of the time needed to tenogenic differentiation	[164 165]
	Uniaxial	7 days	10%	1Hz	(t) ↗ synthesis of glycosaminoglycan (GAG)	[138]
Skeletal myofibroblast	Uniaxial	4 days	7%	0.5Hz	(s) Competitive effect on cellular alignment from patern guidance vs cyclic strain	[166]
Vascular smooth muscle cells	Biaxial	24h	10%	1Hz	(s) Reorientation perpendicular	[168]
	/	90min	1.2 X	1Hz	(l) Reorientation oblique (60 deg)	[169 170]
Fibroblasts	Equi- and uni-axial	2h	16 ↔ 32%	/	(s) Stress fiber disassembly in the stretch direction	[171]
	Uniaxial	3h	6%	0.1Hz	(l) Reorientation and time-dependant genes upregulation	[172]
	Radial	1-6h	1-15%	0.01↔10Hz	(l) ↗ spreading and proliferation optimum at 0.1 Hz	[173]
Endothelial cells	Uniaxial	1h	20%	1Hz	(l) Reorientation perpendicular	[174]
	Uniaxial	3h	10%	0.5Hz	(l) ROS affect stress fiber remodeling and cellular reorientation (⊥)	[175]
	Elongation	30min	5%	0.5Hz	(l) Reorientation to 70 deg	[176]
	Uniaxial ↓	↓	↓		(m) Reorientation ⊥	
	Equiaxial	3h	10%	1 Hz	(l) Random orientation	
	Early reorientation response increases with stretching magnitude and is independent of the rate					
	Uniaxial	20min	18%		(l) Differential effect of shear stress and cyclic stretch on focal adhesion redistribution and actin cytoskeletal remodeling	[189]
Uniaxial	3h	10%	1Hz	(s) Reorientation dependant on the underlying collagen thickness	[177]	
Alveolar epithelial cells	Uniaxial	1h	25 ↔ 37%	/	(l) Disruption of the tight junctions	[178]
Epithelial cells (Caco2)	Biaxial	2- 6h	12%	0.1Hz	(l) Disruption of the apical junctional complex	[190]
	Uniaxial	1h	10%	0.15Hz	(l) Increased proliferation	[179]
	Uniaxial	1h	10%	0,15Hz	(s) Mitogenic activation	[180]
		24h			(s) Promotion of motility on fibronectin	[181]
	Uniaxial	15min		(s) Induced motility through activation of RhoA	[182]	
Organoids	Uniaxial	100h	10%	0.15Hz	(l) Control of the microbiome proliferation	[183]
	Uniaxial	12 days	10%	0.2Hz	(l) Polarization and differentiation of organoids inside a intestine-on-chip	[121]

Table 3.1: Summary of stretching parameters and influence on cell layer with (s) representing the single cell and (l) the layer results

iii) Focus on : intestinal epithelial stretching

In the literature related to cells stretching, intestinal epithelial cells represents a tiny proportion of the published articles. From these articles, two studies are distinguishable by their extent and relevance. They have been done by the group of Lakshmi S. Chaturvedi, Harold M. Marsh, and Marc D. Basson [179–182] and the group of Hyun Jung Kim, Dongeun Huh, and Donald E. Ingber [84, 107, 120, 121, 183].

The first group used the commercial platform of Flexcell International Corp, to expose Caco2 cells, plated on a PDMS membrane coated with type I collagen, to one hour of cyclic stretching (0,15 Hz, 10%). They focused on the impact of cyclic stretching on the cell proliferation and cell migration rates. They successfully identified several pathways implicated in the stretch-induced proliferation response, such as the strain-induces ERK1/2 phosphorylation, requiring α -actinin-1 activation [179] and/or Src-Rac1 phosphorylation and translocation to the nucleus of the cells [180]. These first experiments, performed on a collagen I coating on PDMS membrane, demonstrate the coating-dependant response of cyclic stretching. Indeed, later on switching to a fibronectin coating, they show that the cycling stretching induces a striking modification of the cells response, changing from a proliferation to a migratory phenotype related to wound healing and to the maintenance of the mucosal barrier [181]. Interestingly, the migratory behavior induced by the fibronectin coating relies on both dedicated signalling pathway, such as the RhoA-ROCK activation [182], and joint signalling pathway with the proliferation response, such as the pivotal Src activation [181], as illustrated in the *Figure 3.13*.

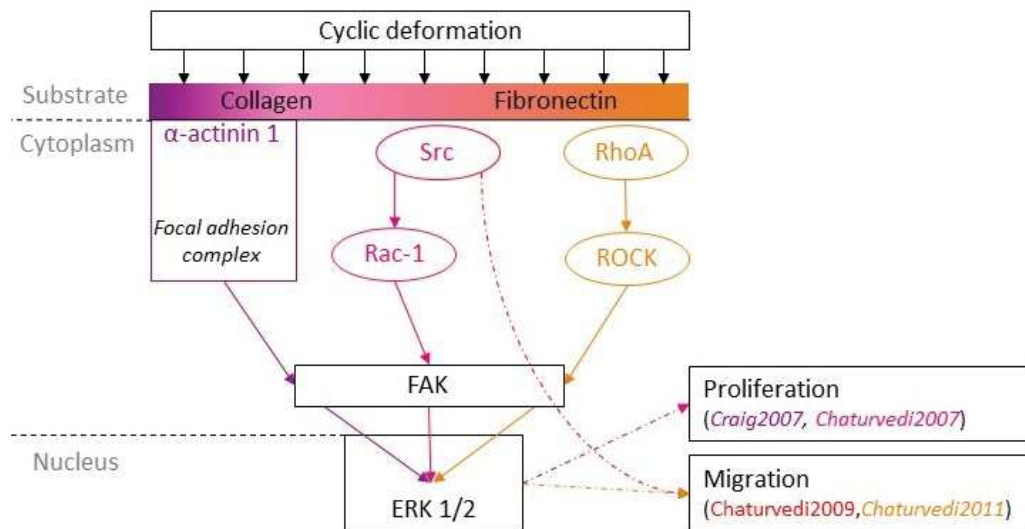


Figure 3.13: Graphic representation of the strain-induced signalling pathways, involved in the cellular response of proliferation and migration, progressively unraveled by the group of Lakshmi S. Chaturvedi, Harold M. Marsh, and Marc D. Basson [179–182]

On the other hand, the second group developed its own stretching platform in combination with biochemical gradient. This platform was already discussed previously. Briefly, it is composed of a central porous membrane separating an upper and lower channel, allowing the development of two communicative compartments representing, respectively, the external lumen with commensal bacteria and fluid shear stress [84] and the blood side with constant flow of culture medium [120]. This platform was used to study the co-culture of bacteria and epithelial cells, to underline the need of peristaltic motion to control the overgrowth of bacteria [84, 106]. Moreover, development of villi-like structure was achieved under peristaltic motion [120]. The last implementations of this platform consist: in the lumen compartment, to use primary epithelial cells isolated from healthy regions of intestinal biopsies, and in the blood vessel compartment, to use human intestinal microvascular endothelium. Similarly to the previous models, formation of villi-like projections is observed over 8 to 12 days of stretching, exhibiting average major and minor axes of 232 ± 17 and $122 \pm 7 \mu\text{m}$ (mean \pm SEM), illustrated in the *Figure 3.14*.

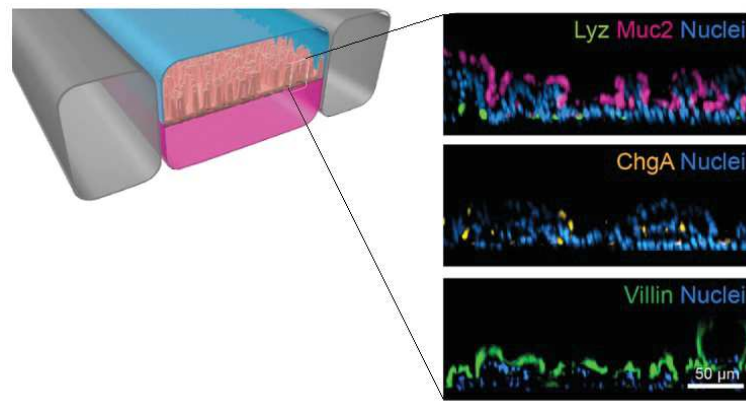


Figure 3.14: A schematic cross-sectional representation of the 3D intestinal epithelial tissue architecture developed on chip (left) and confocal immunofluorescence micrographs (right) showing vertical cross-sections of the differentiated epithelium in Intestine Chip stained for lysozyme (Lyz, green) for Paneth cells, mucin 2 (Muc2, magenta) for goblet cells, chromogranin A (ChgA, yellow) for enteroendocrine cells, villin (green) for endothelial cells and the nuclei were counterstained with DAPI (blue). Adapted from [121]

These villi are lined by polarized epithelial cells that undergo multi-lineage differentiation similar to that of intestinal organoids, with proliferative Ki67-positive cells limited to basal regions whereas lysozyme-positive cells along with chromogranin A-containing enteroendocrine cells, mucus-producing goblet cells and enterocytes with positive villin-stained apical brush borders were present primarily along the apical regions of the villi-like structures. These cells exhibit an apical brush border containing F-actin and NHE3 and a basolateral membrane containing Na^+/K^+ ATPase, as well as ZO-1 and E-cadherin demonstrating a well-formed tight and adherens junctions [107, 121].

This level of complexity can only be achieved thanks to the cyclic stretching inducing the formation of the villi-like structures enhancing the cellular polarization and differentiation.

Conclusion

Cells stretching occurs at different stage of the development as well as, in adults animals and humans. To better understand the effect of this mechanical constraints on cells, many academic groups and companies have developed technological solutions to investigate how cells stretching affect cells behavior. Among the main responses, we can cite in particular cellular reorientation, signalling pathways activation and differentiation. These responses are multiple and vary, in particular, as a function of the cells types, the stretching characteristics and the cell substrate properties. Regarding, the studies on intestinal cells stretching, they have shown that they can induce cell proliferation and migration as function of coating conditions, and that cells can self-assembled in 3D when subjected to stretching combined with shear and biochemical gradients.

It seems therefore, that no 3D-stretching of intestinal cells have ever been developed in the literature. Therefore, we decided to develop a stretcher allowing the stretching of 3D-gut-on-chips to answer the question of the interplay between topography and mechanical activation in the context of an intestinal epithelium.

3.3 Peristalsis-on-chip

The literature on intestinal epithelium stretching is not so abundant and the intestinal cells stretching has been mainly used to induce villification on a 2D flat PDMS membrane. During my PhD project, I aim at better understand *how stretching affects intestinal cells* and *does the cells response depends on the 3D structure of the scaffold* ?.

To address these questions, I needed first to build a stretcher compatible with cells culture conditions, i.e. conditions of humidity and temperature (37°C) inside an incubator. Moreover, this stretcher has to be tunable regarding its speed, amplitude and frequency. Simultaneously, I had to develop an original microfabrication approach to generate 3D structures that can be compatible with cells culture and stretching.

i) Stretcher

The Peristalsis-on-chip platform we will develop should present some specific features, the first one is to induce an uniaxial cyclic stretch on several microfluidic chips at the same time. As previously explained, various technical solutions are available, they can be pressure based or mechanically actuated and work in a direct or indirect mode. We chose, regarding the available material in the laboratory and our bill of specifications, to work with a direct mechanical actuation. During my thesis, I developed four main versions of the cells stretcher, each of them to answer a new issue uncovered by the previous version, until reaching the current one, used for all the experiments presented in the last chapter.

All of the stretcher versions are based on the same production line, a *Strength block*, made of a step by step motor bringing the driving force to deform the PDMS chips. This motor is controlled, for the forth first versions, by an Arduino microcontroller and an integrated controller for the last version. The two codes used to induce the cyclic stretching can be found in Annex. To reproduce the intestinal conditions the continuous cyclic movement imposed to the chips has a frequency of 0.1 Hz and an amplitude of deformation of 10%.

Then, a *Coupling block* composed of a coupler, binding the motor axe to a endless screw, on which a trapezoidal nut is positioned. These two blocks are highlighted in the *Figure 3.15*. The trapezoidal nut is a pivotal element, it transforms the rotation movement into a linear translation. Indeed, this nut will move forward and backward along the endless screw depending on the rotation sense of the motor.

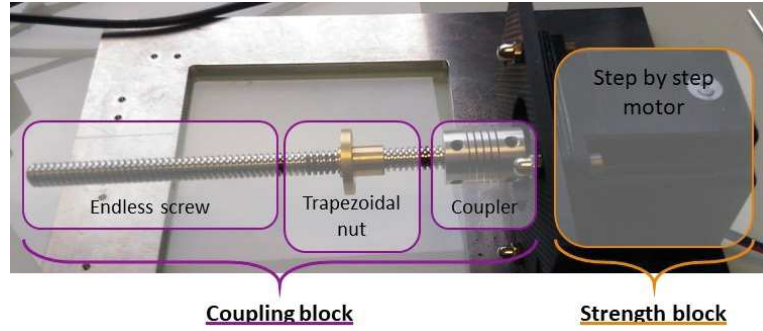


Figure 3.15: Picture of the first version of the stretcher during fabrication, only the *Strength block* and the *Coupling block* had been assembled.

Then, the *Guiding block* is composed of two rectified rods with linear ball-bearing on it, to ensure a linear guiding of the carriers. Finally, the *Carrying block* is composed, depending of the version, of one fix and one movable carrier or two movable carriers. A picture of the first version of these two blocs (highlighted) is proposed in the *Figure 3.16*. The movable carrier(s) is(are) screwed to the trapezoidal nut, therefore subjected to the translation movement of this one controlled by the rotation speed and sense of the stepper motor.

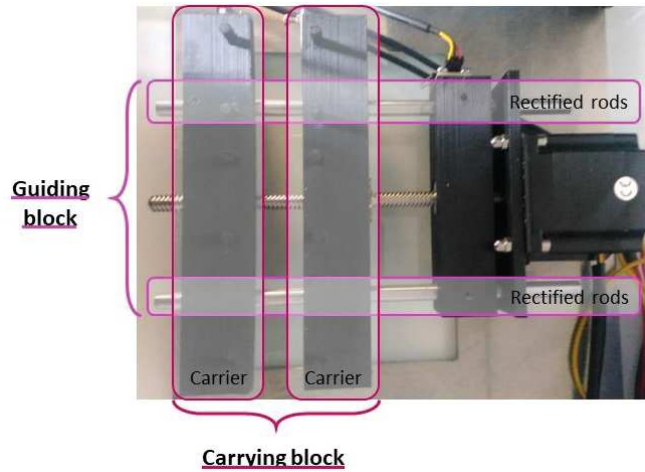


Figure 3.16: Picture of the first version of the stretcher after complete assembly, the *Guiding block* and the *Carrying block* are underlined.

The first version of the stretcher, represented in the *Figure 3.17*, helped me to find the appropriate design of the microfluidic chip. It was composed of one fixed carrier and one movable, at that time we wanted to have the possibility to observe continuously the deformation. However, the stretching of only one side of the chips moved out of the camera field the area of interest, we decided to build a new version implementing two movable carriers.

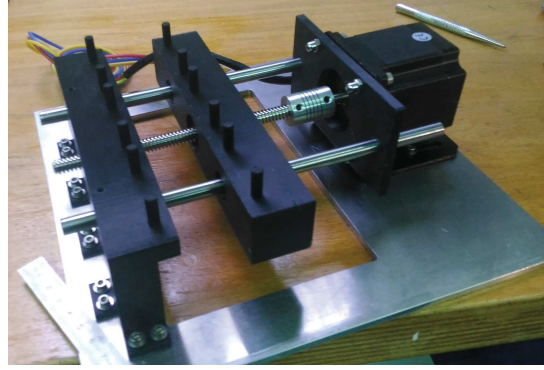


Figure 3.17: Picture of the first version of the stretcher

The second and the third versions of the stretcher, represented in the *Figure 3.18*, possessed two movable carriers with their own strength and coupling blocks. They were both symmetrical to the center of the stretching, allowing the record of the deformation area without any displacement issue any more. They had been both build the same way. The only difference relies on the carrying block material. The second version was 3D printed whereas the third version was made in aluminium. The evolution from 3D printed material to more rigid material was motivated by the need to control perfectly the alignment of the different blocks.

Indeed, after only few weeks of use, the trapezoidal nut of the second stretcher version broke. It seems that the endless screw (made of steel) sands the inside thread of the trapezoidal nut (made of brass) until nothing left. To correct this defect, we changed the nature of the carrying blocs, hoping to get rid of the lack of precision induced by the resolution of the 3D printer. In parallel, we had a look to the materials of the trapezoidal nut used in commercial stretcher. However, only brass was available, as it is an auto-lubricant material, it is often used for pivot pieces. Unfortunately few weeks later the third version of the stretcher broke as well with a similar diagnosis: a premature wear of the trapezoidal nut.

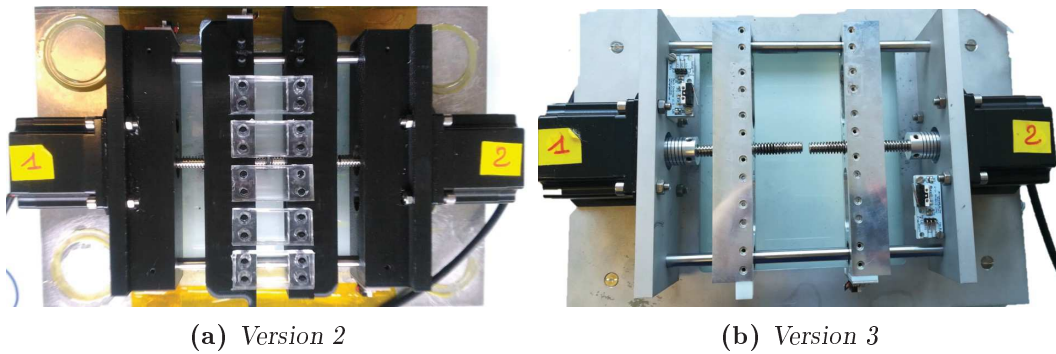


Figure 3.18: Picture of the second and the third versions of the stretcher, positioning of the PDMS chip can be observed on the second version.

To overcome these difficulties, we moved to a semi-commercial version, looking at a translation platform following the same production line than the previous versions, but with an industrial alignment to protect the trapezoidal nut from wear. We found an appropriate product at Zaber Technologies Inc, through the model ZAB-X-LSQ075A-E01-KX14C. This platform consists in a strength block, a coupling block and a guiding block, therefore only the carrying block was missing. To do so we 3D-printed carrying block to adapt this model to my chips (*Figure 3.19*). Moreover, I implemented the movable carrying block design by adding a "swimming pool" (~ 10 mL) to have a better control on the humidity level near my chips.

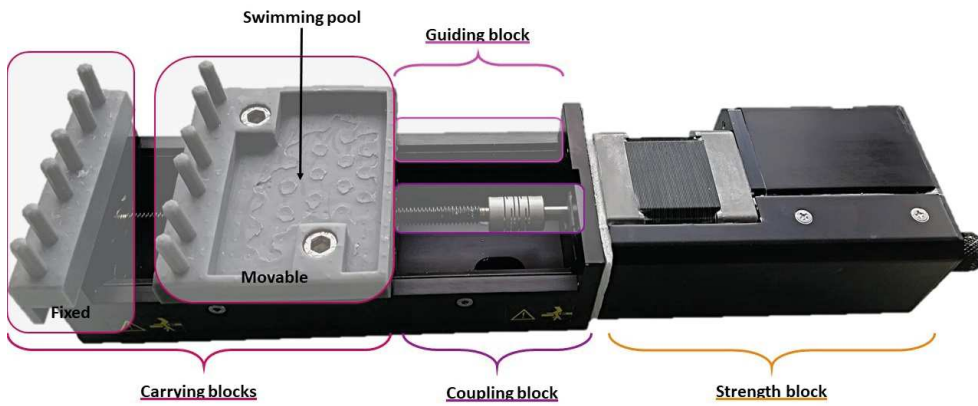


Figure 3.19: *Picture of the current version of the stretcher*

To validate the potential of this stretcher last version, we performed a series of test experiments by stretching chip for period of 48 to 72hours. These experiments show a huge increased of the motor temperature up to 80°C in the incubator. This increased of temperature could be deleterious as it can be transmitted to the carrying blocks and consequently to chip. We showed that this induced a rapid evaporation of the cell culture medium. This increased in temperature is thus absolutely not compatible with cell survival.

To overcome this issue, we implemented a dedicated cooling system (*Figure 3.20*). This cooling system does not rely on a fan system, as it is not compatible with cells culture in the incubator. So we decided to wind up the motor part with first, aluminium to increase the conduction, then with a silicone tube (*diameter* $\sim 200\mu\text{m}$) filled with cold water ($\sim 25^{\circ}\text{C}$) in constant recirculation. The temperature of the cooling bath was calibrated to ensure a temperature near the chips of 37°C .

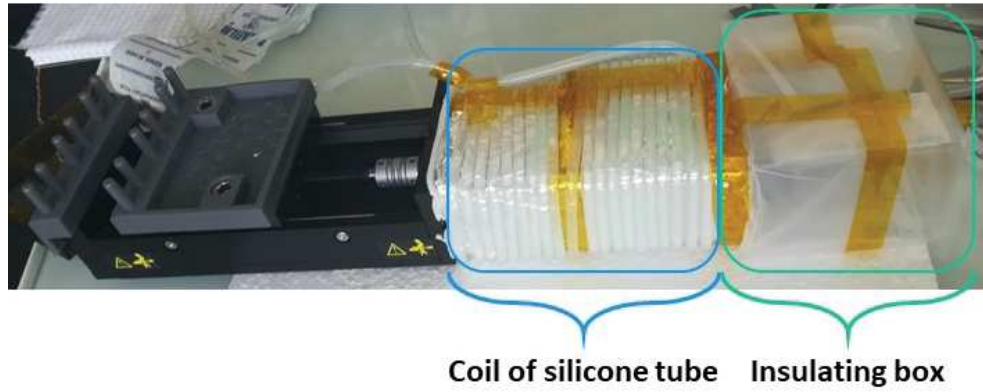


Figure 3.20: *Picture of the first version of the cooling system*

Thanks to this cooling system, we managed to control the motor temperature as well as, the cell culture chip temperature. However, the creation of a cold point inside the incubator induced condensation on the silicon tube, close to the electrical connections. To protect these connections, we enclosed them into an "insulating box". Moreover, we closed the all system using a home made polystyrene box, as shown in the *Figure 3.21*, to prevent variations of temperature inside the incubator prejudicial for the other users. To keep the chips in a sterile environment we 3D-printed a "roof" to confine them and avoid any contamination from the outside and between the chips.

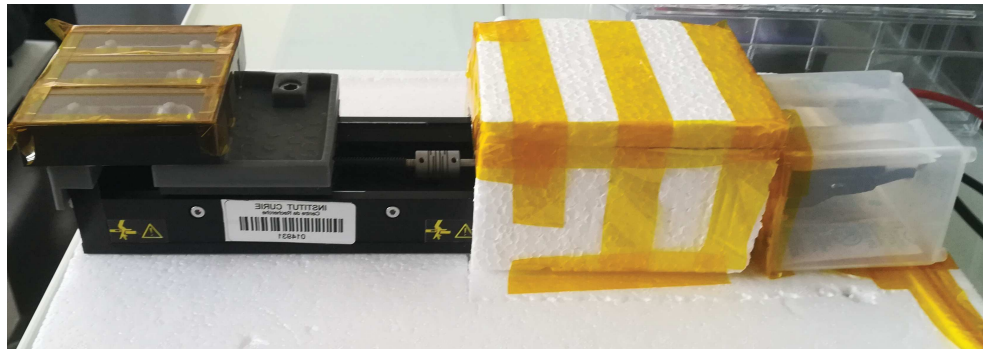


Figure 3.21: *Picture of the last version of the cooling system*

ii) 3D stretching chips microfabrication

Simultaneously to the development of the stretcher, I have been working on the development of an original protocol to fabricate PDMS chips compatible with the stretching system and offering the possibility to stretch cells seeded on 2D or 3D structures.

To develop a chip for cell stretching there are different specifications to be fulfilled by the chip :

- the cells culture chip should integrate a reservoir for cell culture medium mandatory for long term cells culture and this reservoir should be accessible to exchange culture medium if necessary
- the chip dimension should be constant whatever the 3D structure to be plugged in the
- the cells culture area should be flat or presents 3D structures to compare both conditions, and the dimensions of the 3D should be modifiable at will

From these functional specifications and few attempts later, I converged to original mold presented in the *Figure 3.22*. This mold is "all-in-one", it does not request any additional steps compared to other protocols. Once the PDMS cured, the chip is finished.

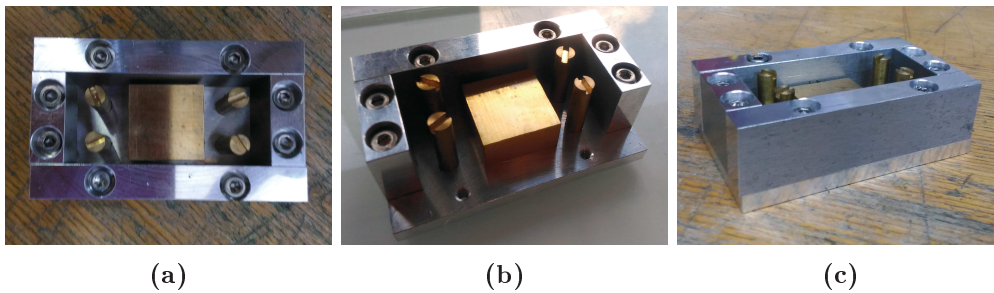


Figure 3.22: Pictures from various angle of the mold used to do PDMS chip

The bottom part and the external halls are made in aluminium, to prevent adhesion of the PDMS. The four columns have been made from a brass rod, their diameter of 5mm correspond to the diameter of the picks on the carrying blocks to plug the chips on the stretcher. These parts will give the external structure of the chip with plugging areas. At the same time to define a stretchable cell culture area, an original brass cube is positioned before curing PDMS to define both the reservoir area and eventually the cell area 3D structure. Examples of PDMS chips are proposed in the *Figure 3.23*, as well as a summary of the dimension of these ones.

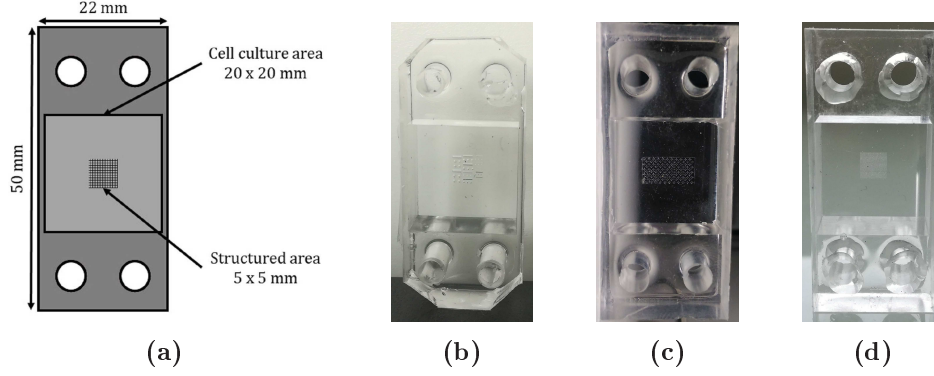


Figure 3.23: Schematic view of the PDMS chip (a) , recapitulating its main dimensions as well as examples of PDMS chips (b,c,d)

To achieve a good reproducibility, in particular for the brass cube positioning, all the parts of the mold are screwed to the bottom plate and the same volume of PDMS is cured in the mold ($V \simeq 7\text{ mL}$) to control the thickness of the bottom membrane of the chips ($e \simeq 1\text{ mm}$). Moreover, the thickness of the side walls of the chip has been set at 1 mm to reduce the elastic resistance of the chip therefore allowing the motor to stretch three chips in parallel.

To obtain the specific geometry of my central cube, I used micro-milling, this technology uses micro-drills to mill the brass with the given 3D structure. To do so, I first draw the 3D design of my piece (using Catia software), then I implement the path of my tools, meaning the speed of work, the depth of the working path, the strategy used to remove matter (using Fusion software). Finally, the program is translated into " a machine language" by a given software compatible with the Minitech machine. The complete process of production is illustrated in the *Figure 3.24*.

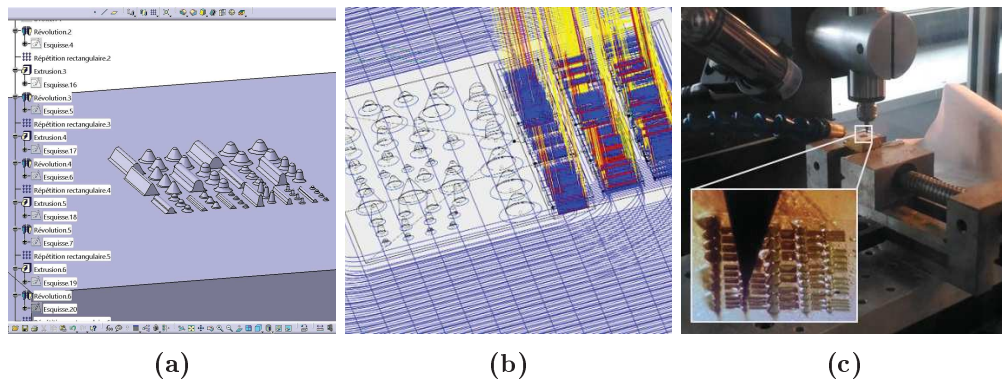


Figure 3.24: Representation step by step of the micro-milling process, from the drawing (a) and the implementation of the paths (b) to the machining (c).

After fabrication, the 3D mold was characterized using PDMS replica coated with a fluorescent protein to visualize the 3D structures with a confocal microscope. The initial design has $2D^{\frac{1}{2}}$ and 3D structures which will become grooves and crypts in the replicated PDMS chip. Originally, structures were milled with different heights, 100 μm , 200 μm and 300 μm , with different radii (50 μm , 100 μm and 150 μm) and two slopes (60° and 80°). The choice of these structures will be discussed in the next chapter. To be able to micro-mill this 3D mold, in an admissible lapse of time (less than a week), we had to use drills of 100 μm of diameter with a working step of 10 μm . Therefore, the first generation of 3D mold had steps with height similar to the size of a cell preventing the study of the effect of the slopes. So I developed, in parallel of the micro-fabrication process, an original approach of electropolishing. This electropolishing reduce the effect of roughness but significantly change the dimensions of the master mold and consequently the dimensions of the replica. The final dimensions obtained are presented in the Table 3.2.

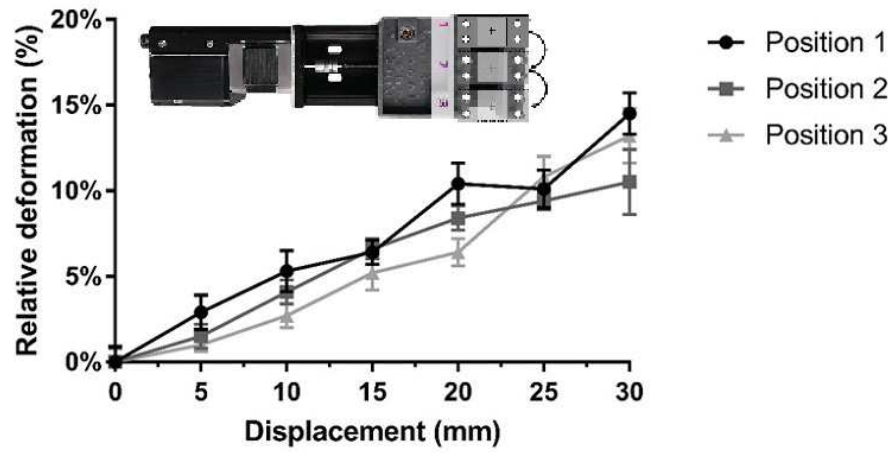
Original dimensions		Effective dimensions
Height	200 μm	$129 \pm 8 \mu\text{m}$
	300 μm	$250 \pm 5 \mu\text{m}$
Radius	50 μm	$51 \pm 5 \mu\text{m}$
	100 μm	$76 \pm 4 \mu\text{m}$
	150 μm	$98 \pm 4 \mu\text{m}$
Slope	60°	$53 \pm 6.55^\circ$
	80°	$74 \pm 7^\circ$

Table 3.2: Geometrical dimensions of the 3D structures

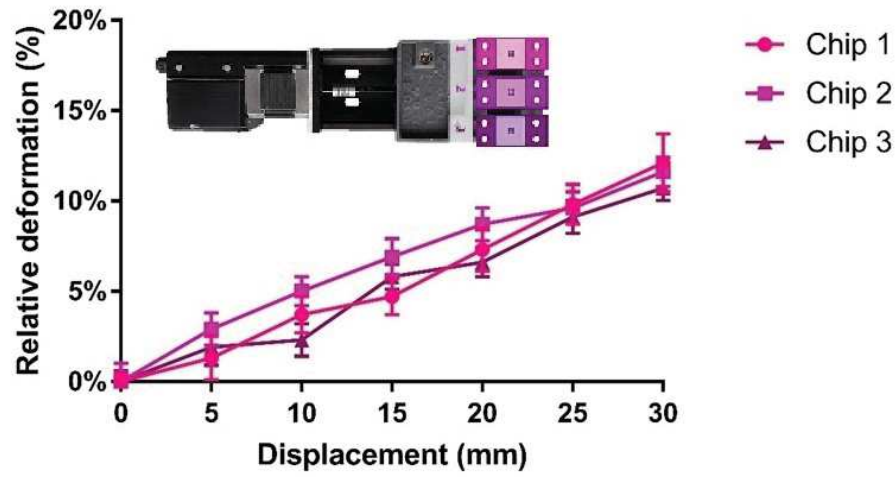
iii) Calibration

Before stretching cells, we have first calibrated the stretcher and the response of the microfluidic chip to the stretching. We looked at four criterion to guarantee the uniformity of the stretching over the different positions on the stretcher, between chips, inside the area of interest and over time. To do so, we micro-milled "calibration chips" with a central grid of 5 mm \times 5 mm with a square pattern of 200 μm long spaced 10 μm and measured the size of around ten squares in function of the strain applied to the chip.

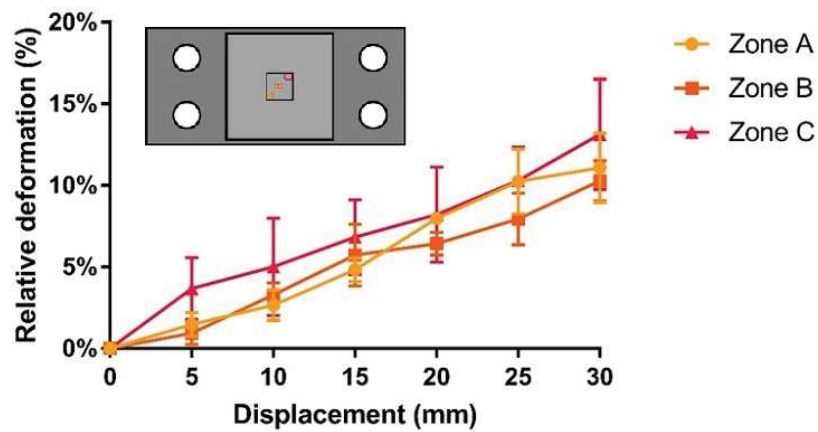
First, to ensure a uniform deformation over the different position on the stretcher, we performed this measurement on a same chip positioned on each of the chip positions on the three available positions of the stretcher, labelled 1, 2, 3 in the Figure 3.25 (a) . The variation of the of the relative deformation of the squares in function of the motor displacement shows no significant variations regarding his position on the stretcher (mean standard deviation $\sim 1.3\%$), therefore these ones can be considered similar.



(a)



(b)



(c)

Figure 3.25: Variation of the relative deformation of the squared (in the stretch direction) as a function of the applied elongation at (a) three different positions on the stretcher, (b) three different chips and (c) three different areas of the same chip

Secondly, to estimate the reproducibility of the protocol of fabrication of the microfluidic chips we measured the variability between chips. To do so we positioned three different chips on the three available positions of the stretcher and measured the deformation of the squared in function of the motor displacement. The results obtain (Figure 3.25 (b)) shows negligible variations between the chips (mean standard deviation $\sim 0.9\%$) validating the reproducibility of the fabrication protocol.

Thirdly, the deformation in the area of interest (the central $5\text{ mm} \times 5\text{ mm}$) needs to be homogeneous, so we looked at three area (labelled A, B, C in the Figure) in the central part and record the deformation of the squared in function of the motor displacement. The results, Figure 3.25 (c) , are matching regardless the area (mean standard deviation $\sim 1.9\%$) allowing us to consider the central part of the chip uniform in term of deformation.

Moreover, to go further in the characterization of the elongation induced by the stretcher and its effect over time. A study of the field of deformation for a period of 24 hours was performed with the help of Charles Cavaniol, PhD student of the team. We first studied the evolution of the speed tensor in function of the deformation, and in particular its component symmetric (the tensor of the rate of deformation) and antisymmetric (the tensor of the rate of rotation). The second component is null, as a result of the unidirectional deformation applied to the chip. To estimate the rate of deformation, the lateral and the longitudinal speed components have been plotted as a function of the associated direction of deformation at $T=0\text{h}$ (red) and $T=24\text{h}$ (blue) (Figure 3.26). The linearity of these curves demonstrates a constant rate of deformation similar for 0 hour and after 24 hours of stretching. Moreover, the low standard deviation for each point demonstrates the homogeneity of the deformation over the central area of the chip. From the slope of these two graphics, we can estimate the lateral and longitudinal contribution to the field of the deformation and calculate a rapport between their slope equal to 0,4. This transverse contraction is needed to increase the effect of the stretching on the cells [207].

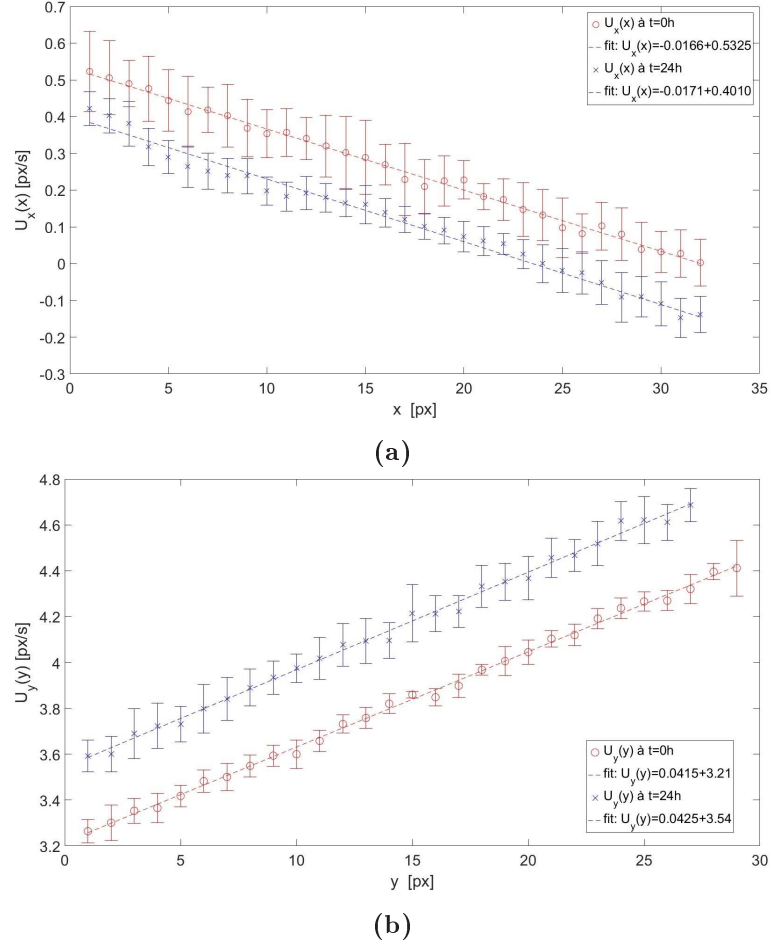


Figure 3.26: Variation of the lateral (a) and the longitudinal (b) components of the speed as a function of the deformation in the lateral and longitudinal direction respectively, with the help of Charles Cavaniol

3.4 Conclusion

We have developed a versatile stretching platform able to stretch three chips at the same time, with an homogeneous and linear field of deformation regardless the position on the stretcher, the chip fabrication, the area of interest and the duration of the experiment. Moreover, this platform has been optimized to support long stretching time for 2D and 3D chips. Therefore, we can now use this stretching platform to study the influence of the cyclic stretching on the behavior of Caco2 cells seeded on a 2D and 3D chip. The next chapter discusses the results obtain with this platform.

Chapter

4

How does stretching affect intestinal epithelium?

Contents

4.1	Determination of the operating conditions	101
	i) PDMS Chips	101
	ii) Coating of the chips	102
	iii) Seeding of the cells	103
	iv) Stretching of the chips	104
4.2	Influence of intestinal cells stretching on 2D experiments	105
	i) How does stretching affect the tissue state?	105
	ii) How does cell stretching affect the cell morphology?	111
	iii) How does cell recover the stretching influence?	120
	iv) How does stretching affect primary cell: Organoids ?	121
4.3	Influence of the stretching on 3D experiments	122
	i) How stretching does affect the covering of the patterns ?	124
	ii) Influence of topography on the cellular alignment in the grooves	127
4.4	Conclusion	134

Introduction

The first part of my PhD project was dedicated to the development and characterization of a new *Gut-on-Chip* platform. This work has shown that reproducing a 3D scaffold made of collagen I and embedding fibroblasts is already an achievement but it does not recapitulate all the gut complexity as the mechanical stress applied on epithelial cells is not reproduced in vitro. At the same time, some papers have shown the interest of subjecting intestinal cells to mechanical stress in order to reproduce their physiological behavior. In this context, I decided to study the influence of stretching (mimicking peristalsis) on intestinal cells cultured on 2D and compare this effect with cells grown on 3D scaffold.

To investigate how stretching affects intestinal epithelial cells as a function of the scaffold properties, I built my own stretching module compatible with 2D and 3D cell culture, following the fabrication steps described in the previous chapter. The chapter 4 will introduce the results obtained on the influence of stretching on intestinal cells, using all the previously described implemented tools.

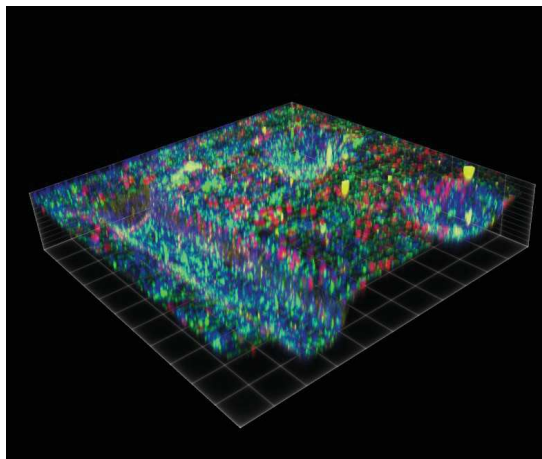


Figure: 3D reconstruction of one pattern covered by Caco2 cells
Nucleus (blue) Tight junction (green) Proliferative cells (red)

4.1 Determination of the operating conditions

To describe concisely and clearly my experimental conditions to study the effect of intestinal cells stretching, *Figure 4.1* reports the different conditions that have been screened in this first series of experiments. First of all, the PDMS chips are made thanks to the micro-fabrication approach previously described, and a coating is performed to allow cells adhesion and to mimic adhesion molecule present in the basement membrane. Cells are seeded at a given concentration on the PDMS chip. In this first series of experiments, the chips are flat. This series of experiments allows to evaluate the influence of cells stretching in 2D cell culture. Before starting the stretching, the cells are let to recover for 24 or 48 hours depending on the experimental conditions needed. Finally I stretch in parallel 3 similar chips. *Figure 4.1* presents the general setting of this experiments and in the following section, we will discuss why and how these parameters have been selected.

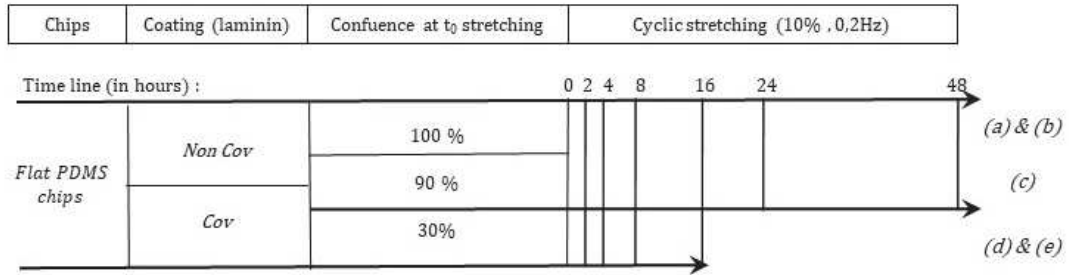


Figure 4.1: Sketch of the experimental protocols followed during my thesis: (a), (b), (c), (d) and (e) represent the various experimental conditions studied during my thesis regarding respectively the coating techniques used (covalent versus non-covalent) and the initial confluency at the beginning of the stretching experiment (from 30% to 100%)

i) PDMS Chips

The PDMS chips were prepared according to the protocol described previously. The first series of experiments has been performed with cells grown on 2D chip, meaning that the central part of the chip is free of micro-milling. This first series of experiments has been performed in order to optimise the operating conditions, and as a control condition to be compared with 3D experiments.

ii) Coating of the chips

A coating was performed to overcome the poor cell adhesion on PDMS and to induce a more biomimetic scaffold for intestinal cells culture [208, 209]. *In vivo* studies of the intestine basement membrane along the crypt-villus axis, have identified several proteins such as laminins, type IV collagens and fibronectin involved in the process of cell differentiation and undifferentiated proliferative pattern, respectively [210, 211]. Furthermore, *in vitro* studies have confirmed the influence of the basement membrane composition on the cellular behavior. For instance it has been shown that replacing collagen type I by fibronectin induces the switching from a proliferative to a migration behavior of Caco2 cells[179–182], while laminin coating was correlated with cells differentiation process [212]. Moreover, exhaustive studies of the intestine basement membrane reveal that laminin is its major component, as well as that laminin-integrin interaction plays a major role in cell adhesion, growth, polarisation and differentiation [213–215]. Therefore, the laminin appears as the best choice for recapitulating as faithfully as possible the basement membrane of the intestine in our *in vitro* model.

Besides, we also aimed at investigating the effect of the coating type on the cells behavior. Indeed, it has been extensively shown that cells are affected by the coating properties of the scaffold [216]. For instance the presence of a gradient of adhesion molecules on the scaffold, called haptotaxis, can play an important role in neurons growth cone guidance [217]. Studies on the cellular motility linked the surface ligand and concentration [218], and its spatial distribution [219–221] with the ability of cells to migrate on a substrate. In our case, we have investigated how cells will behave on laminin-coated PDMS according to different coating strategies: covalent and non-covalent coating.

Coating techniques

Non covalent coating requires first the activation of the surface by a plasma treatment, then a solution of laminin (0.02 mg mL^{-1}) is incubated for 1 hour. In this condition, the laminin coating mainly relies on electrostatic, hydrogen and Van der Waals interactions.

Covalent coating requires first the activation of the surface by a plasma treatment, then (3-aminopropyl) triethoxy-silane (APTES) and cross-linker glutaraldehyde are dropped on the surface, 30 minutes each, followed by the incubation of the laminin solution for 1 hour. This surface modification, illustrated Figure 4.2, induced a covalent binding of laminin to the PDMS surface.

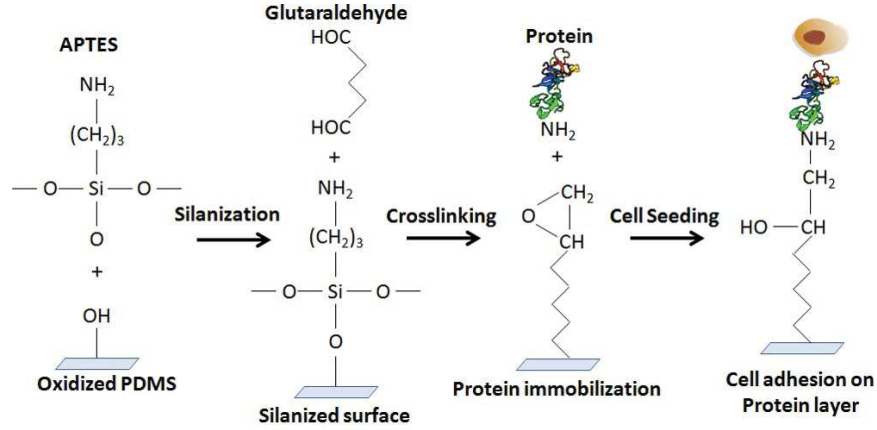


Figure 4.2: Representation of the covalent binding process adapted from [222]

These two coatings should induce difference in terms of laminin surface concentration and in the force between the adhesion molecule and the scaffold itself [223, 224]. From this perspective, we wanted to investigate the influence of the adhesion molecule coating on the cells response to stretching.

iii) Seeding of the cells

All the first set of experiments were performed using Caco2 cells. This cell line is commonly used in the gut-on-chip field, as a cellular model of the intestinal epithelium [84, 120, 179–183], it recapitulates most of the properties of a normal intestine. Indeed, these cells are undifferentiated when seeded, while at confluence they form polarized monolayers of cells joined by tight junctions and present a well-developed apical microvilli [225]. Moreover, they are able to differentiate into several intestinal cell types such as enterocytes, goblet, enteroendocrine and paneth cells [19, 120]. Nevertheless, even though this cell line has been often used in the field of gut-on-chip, pressure to move to a more biologically relevant model increases in particular by using intestinal organoids.

Besides investigating the coating effect, we also studied how the cells response to stretching depends on their initial surface density. To do so, we have been working with different initial cell density when starting cell stretching. After the seeding of 2×10^5 cells/chip the proliferation time was set either at 24 or 48 hours to allow the cells to recover and reach, respectively, a complete or a quasi-confluency (estimated to $\approx 90\%$) at the beginning of the experiment time. To investigate further the influence of the cell density, 5×10^4 cells/chip were seeded with a recover time of 48 hours to let them reach 30% of confluency at the beginning of the stretching experiment. This last set of experiments was performed and analysed by Bernheim-Dennery Moencopi, whom I supervised during her Master 2 internship.

iv) Stretching of the chips

In the literature, the influence of the stretching has been mainly studied at short time scale (below 1 hour) and long time scale (more than 100 hours), especially for gut on chip platforms but the intermediary scale is not as well documented. To fulfill this gap, stretching of the chips was performed over 6 time points : 2h, 5h, 8h, 16h, 24h and 48h. After stretching, the cells were directly fixed by PFA to perform immunostaining and imaging. Finally one set of experiments was performed to investigate the influence of "resting time"; in this case the fixation step was performed 24h after the stretching step.

During this study every experiment was performed in triplicate. Indeed, the design of the stretcher allows the simultaneous stretching of three chips, therefore every time point represents the sum of the data achieved with these three chips. In parallel, three others chips were seeded at the same time of the stretched ones, without being stretched and represent the control condition.

Staining and image analysis

After fixation, the protocol of immuno-staining described in the Annex A was performed. The chips were all stained with ZO1 antibody to stain the tight junctions and DAPI was used to stain cells nuclei. Images from 5 different fields per chip were taken using a 10x objective, on a confocal microscope. This wide field of view ($1163.64\mu\text{m} \times 1163.64\mu\text{m}$) allow us to study the tissue response, encompassing hundreds of cells. The following graphics, that will be discussed in the following, represent the distribution of all the data extracted from these 15 images for each time point and condition, the error bars representing the standard deviation. These measures were obtained using ImageJ software [226], and in particular the plugin Tissue Analyzer [227, 228].

Significant differences in cell parameters between groups were identified using ordinary one-way ANOVA followed by Holm-Sidak's multiple comparisons testing. In the following graphs **** correspond to $p < 0,0001$.

4.2 Influence of intestinal cells stretching on 2D experiments

Our study of the influence of the stretching on the cellular behaviour revolves around two main axes. The first one is a general consideration on the tissue regarding the confluence and the cell density to roughly estimate how cells stretching affect cells proliferation. The second axis encompasses several cell morphological characteristics such as, the cellular area, orientation, circularity as well as their aspect ratio. These observations have been performed within a wide range of experimental conditions, regarding the coating nature, the initial cell density and the scaffold topography over time. As a reminder, for all of these experiments the Caco2 cells were subjected to a cyclic stretching of 10% of deformation at a frequency of 0.2 Hz.

i) How does stretching affect the tissue state?

First of all, we aim at characterizing the global influence of the stretching at the scale of the tissue, before zooming in the individual cellular response. The first informations we looked at were the percentage of coverage of the cells and the cellular density. Before discussing quantitatively the experimental data, I would like first to illustrate how cells could look like in my experiments. *Figure 4.3* are presented some peculiar patterns that look alike flowers (encircled in the image a) possibly early events involved in extrusion processes, as well as the important cell shape diversity that can be observed in a same image, where tiny cells stand along side huge cells (in the image b) or even holes that should illustrate cells detachment (in the image c).

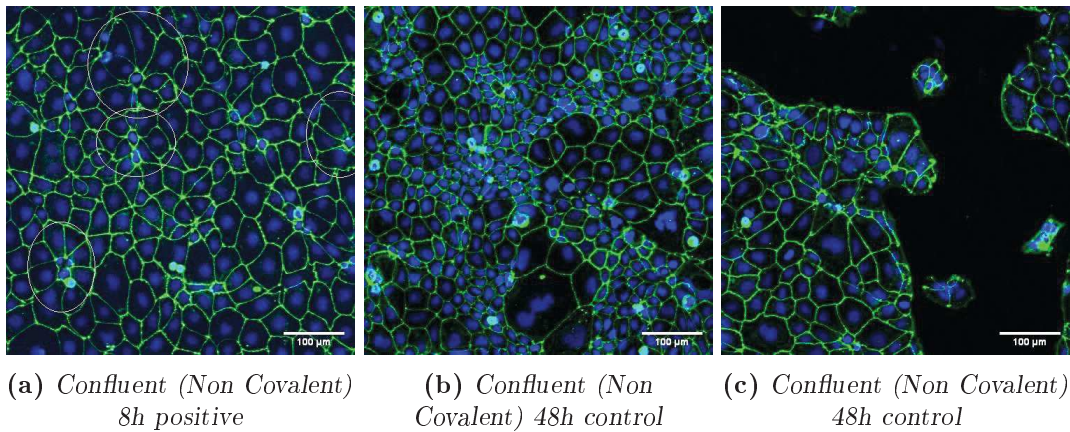


Figure 4.3: Pictures from various area of *Confluent, non-covalent chips* (Objective 10x, the tight junctions are stained with ZO-1 (in green) and the nucleus with Dapi (in blue))

Confluent, Non-Covalent experiments. The first set of experiments was performed on a non-covalent coating of laminin, where Caco2 cells were grown until confluency (48h of proliferation before starting the stretching step). The chips were then stretched during 2, 5, 8, 16, 24, or 48 hours. The experimental protocol is represented in the *Figure 4.4*.

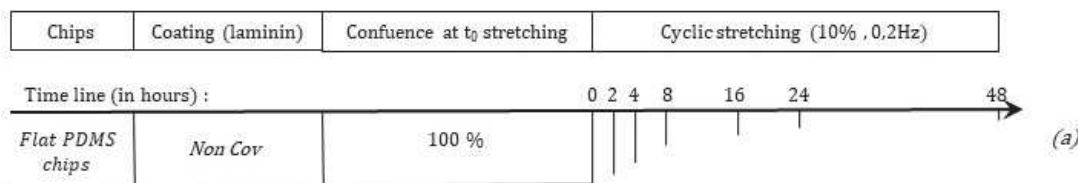


Figure 4.4: Sketch of the experimental protocol for the confluent, non-covalent experiments (a)

The distribution of the cellular density and the confluency are represented for each time point in the *Figure 4.5*, with the mean depicted as a black vertical line. At first glance, we can see a slight decrease over time of the confluency from 99% after 2 hours to 92% after 24 hours, this decrease is not significant (ANOVA) and seems to be independent of the stretching, except for the extreme condition (48 hours). Indeed, after 48h of stretching the percentage of the chips covered by the cells is around 70%, significantly different to the control conditions, this huge decrease in coverage is due to cells detachment, as we observed patches of cells detached for non covalent coated scaffold.

If we now look at the cellular density a more complex dynamics can be observed. For the control experiments, we observe a continuous decrease of the cellular density (by a factor of 4.7) during the first 24 hours. Then the cellular density increases until reaching again the same level than the one of the 2 hours experiment ($1,5 \times 10^5 \text{ cells/cm}^2$ represented by a dashed horizontal line on the graphic). When the experiment starts (0 hour) the cells are confluent, therefore the contact inhibition should decrease the proliferation rate of the cells without slowing down the cellular death, resulting in a slight decrease of the cellular density during the first 24 hours, while the cells proliferate accordingly to their population doubling time of approximately 32h [229], and reach again a similar cell density after 48 hours of culture.

On the other hand, for the stretched experiments, an increase of the mean cellular density is first observed, until 5 hours, then it seems to stabilize for the first 24 hours. In this lapse of time, only the data achieved for short (2h) or long time stretching (24h) display a significant density difference between the stretched and the control chips. Whereas for 5, 8 and 16 hours no significant effect of the stretching is observed individually, it is the global trend which differs from the control conditions, where a decrease of cell density with time is observed while it is not the case for the stretching conditions.

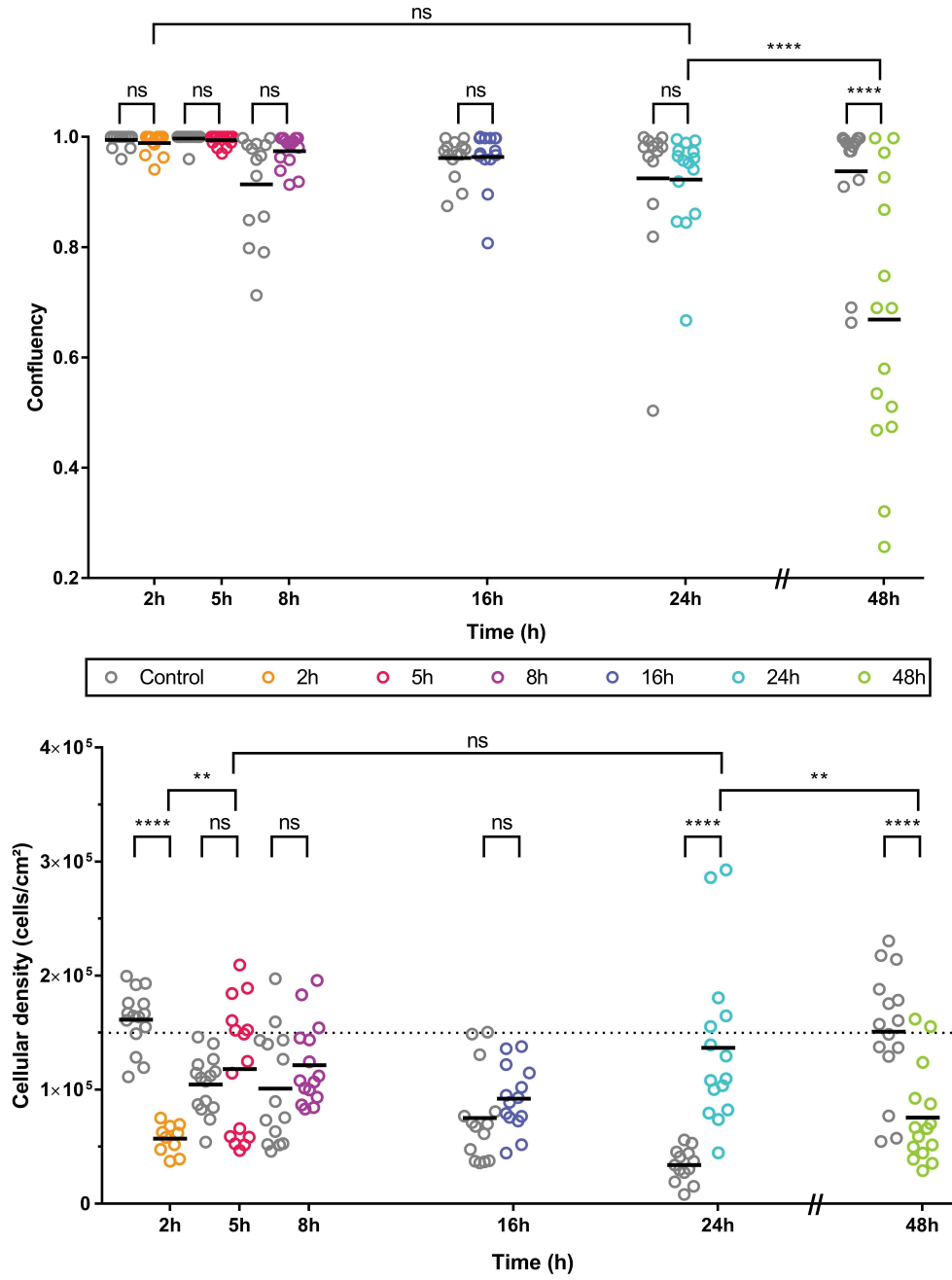


Figure 4.5: Variation of the confluency and the cellular density as a function of time. Comparing stretching and non-stretching conditions for the Confluent, Non-covalent experiments.

The first row of significant marks represents the result of the one-way ANOVA test performed between the control and stretched conditions, the two above rows represent the result between different stretched conditions. When one mark cover several time points it means that this value is the same for all the possible comparison between them. **** ($p < 0.0001$)

Could we interpret this difference as an unbalanced effect of the stretching on the contact inhibition ? To properly answer this question more experiments are needed, such as EdU and annexin V to be able to count proliferative and dead cells respectively, as well as we need to characterize the stabilizing effect of ECM creation by the cells for a better statistical analysis and to rule out experimental bias.

Confluent, Covalent experiments. The following experiments were performed on a covalent coating of laminin, where Caco2 cells were grown until confluency (48h of proliferation) then stretched for 2, 5, 8, 16, 24, or 48 hours. As previously, the cellular density and the percentage of confluency have been evaluated for each time point in the *Figure 4.7*. The experimental protocol is represented in the *Figure 4.6*.

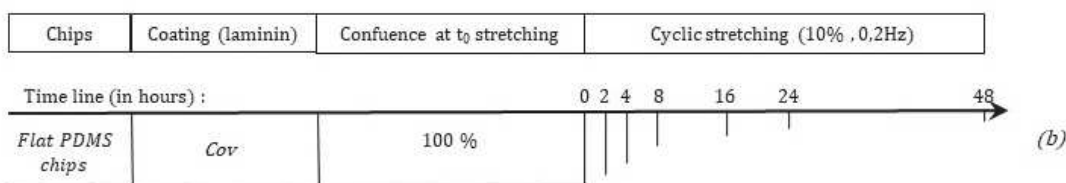


Figure 4.6: Sketch of the experimental protocol for the confluent, covalent experiments (b)

We can observe a difference between the percentage of cell coverage variation with the previous set of experiments. Indeed, for the covalent coating the confluency stays around 100% even in stretched conditions without the time-dependent cellular detachment observed for non-covalent coating. These results show that increasing the interaction force between the adhesion molecules and the PDMS scaffold can limit the cells detachment induced by stretching for long stretching time.

If we focus our attention on the cellular density we observe, that contrary to the non-covalent binding conditions, the similarities between the control and the stretched experiments are edifying. The cell densities measured in stretched and non-stretched conditions vary similarly. First, we observe a significant decrease of the density followed by an increase which stabilizes to a cruising value: $1.5 \times 10^5 \text{ cells/cm}^2$ this variation is also similar to what has been observed in non-stretched and non-covalent conditions.

Besides this similarity, one should mention that there is still a difference when comparing covalent and non-covalent-coating conditions, regarding the kinetics of the cell density variation. Indeed, in the non-covalent settings, cell density increase takes place around 24h and 48h hours, while in the covalent settings it takes place around 16h. This difference in cell behavior as function of the coating conditions, could be due to a difference in laminin surface concentration or to the conformation of the coated molecules. Indeed, it has already been shown that covalent coating may induce higher cell proliferation and migration [218, 223].

However at this stage, we are not able to identify if the surface concentration or the protein conformation are responsible of this behavior. Finally our main observation in the covalent coating conditions, is that neither the cell confluency nor the cells density are affected significantly by stretching. However one main observation, is for 48h of stretching cell detachment is negligible using laminin covalent coating while it is not with non-covalent coating.

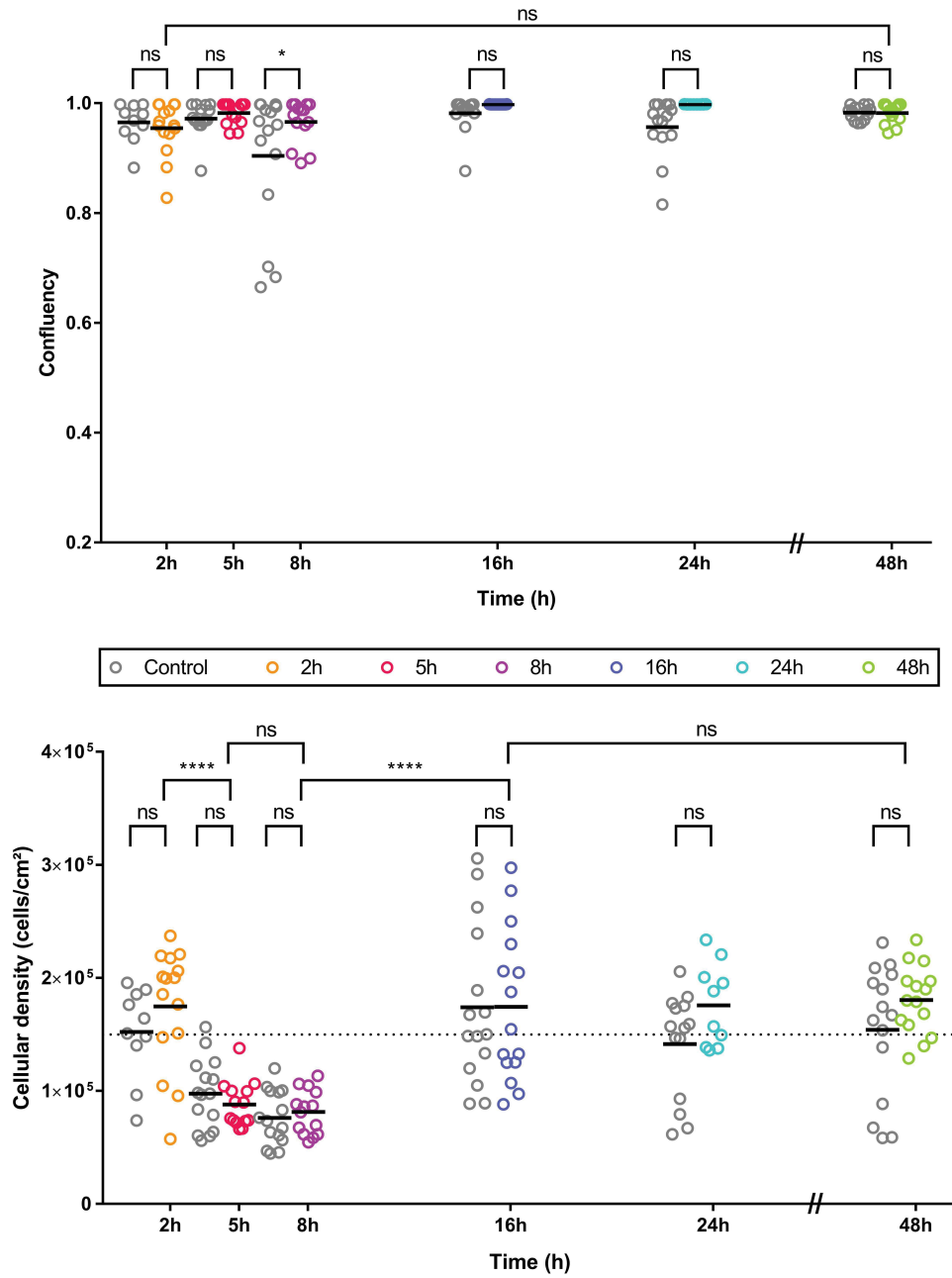


Figure 4.7: Variation of the confluency and the cellular density as a function of time. Comparing stretching and non-stretching conditions for the Confluent, Covalent experiments.

The first row of significant marks represents the result of the one-way ANOVA test performed between the control and stretched conditions, the two above rows represent the result between different stretched conditions. When one mark cover several time points it means that this value is the same for all the possible comparison between them. **** ($p < 0.0001$)

ii) How does cell stretching affect the cell morphology?

In the majority of the publications related to stretching experiments, one effect has been particularly observed: the cell reorientation. Therefore, it was one of the first effect we looked at along with the circularity and the aspect ratio of the cells. As expected, cell orientation is affected by stretching and will be described in more details in the following. To evaluate the morphological changes of cells as function of the stretching and laminin coating conditions, two shape descriptors have been measured. The first one is the circularity ($4\pi \times \text{area}/\text{perimeter}^2$), in case of perfectly circular cell it should be equal to 1. The aspect ratio is defined as (after adjusting the cell to an ellipse, major axis/minor axis). These two shape descriptors do not exhibit any obvious stretch- or coating- induced changes, as illustrated in the Figure 4.8. Moreover, no strong correlation values have been found between the angle and the circularity and the aspect ratio. Acquisition with different staining and a higher magnification could bring some clues on the structural change, i.e. the cytoskeleton arrangement, occurring during stretching and why this reorientation is free of morphological change.

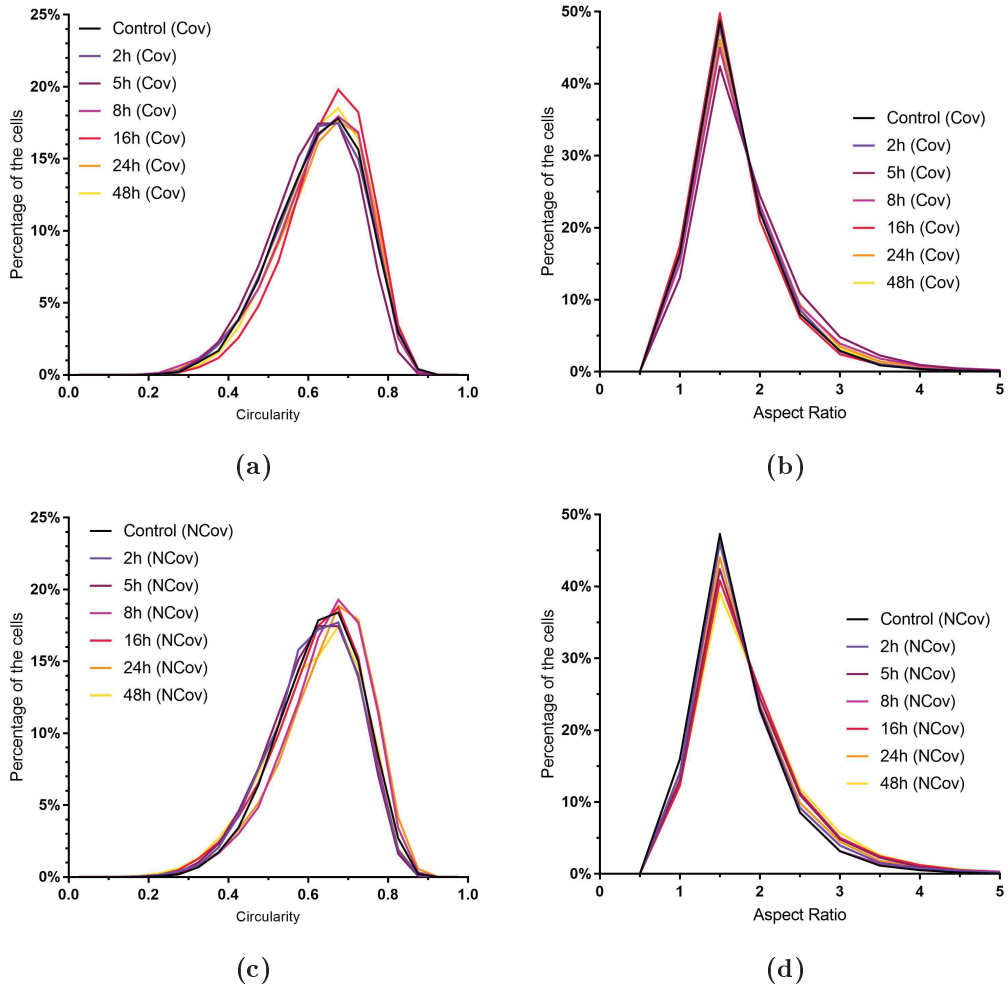


Figure 4.8: Distribution of the circularity and the aspect ratio over time for a covalent (a) & (b) and a non-covalent (c) & (d) coating

The Cellular Orientation

To evaluate the cellular orientation, images were analysed using ImageJ free software. In this image analysis, every cell is approximated by an ellipse, defining a major and a minor axis. The cellular orientation is defined as the angle between the major axis and the horizontal, as represented in the Figure 4.9 by the Greek letter θ . In my experiments, the horizontal axis and the direction of stretching are the same, therefore an angle of 0° or 180° represents a cell aligned with the stretching direction whereas an angle of 90° represents a cell perpendicularly oriented.

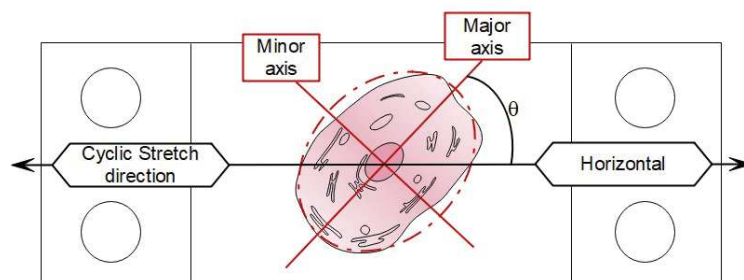


Figure 4.9: Representation of the ellipse approximation performed by ImageJ software on a cell represented inside a chip

The Figure 4.11 displays the distribution of the cellular orientation for all the time points and all the conditions studied. This distribution results of the cellular orientation for all cells, from the 15 images for each condition. All together, these results show that cells are affected by stretching in a time-dependent manner and that this stretching influence on cell orientation depends on both the coating conditions and the initial conditions of cell confluence. We will thus compare and discuss one by one these different conditions. Two representations of these results are proposed in the following:

- the complete distribution of cell angle orientation between 0° and 180° in the different conditions. This representation allows a complete view of cells response to stretching (Figure 4.11).
- the variation of the percentage of cells oriented along the main orientation axis ($90^\circ \pm 10^\circ$) as function of time allowing an easier comparison of the different conditions (Figure 4.12).

Besides these experiments and to better asses the influence of cells stretching as function of the operating conditions, we have fitted our data with a simple kinetic model [230]. This work was performed in collaboration with Mallory Carlu, PhD student at Aberdeen university, Scotland. The experiments (d) and (e) possessing only three time points, have been excluded from this study.

Kinetic model

The simple description for being in equilibrium between two states, A and B, is given by the following equilibrium.



Here, A and B represents the percentage of cells with an orientation comprised between 80° and 100° considered as the cells affected by stretching and the rest of the population, respectively. k_1 and k_2 represent the rate constants for changing from one state to the other. In this model, these rate coefficients do not explicitly depend on time and are assumed to be independent on previous events [230]. Therefore, the variation of A is function of time and can be described as:

$$\text{Variation of } A(t) = \left(\begin{array}{cc} \text{Total number of} & \times & \text{Fraction that} \\ \text{unchanged cells} & & \text{become A} \end{array} \right) - \left(\begin{array}{cc} \text{Total number of} & \times & \text{Fraction that} \\ \text{changed cells} & & \text{become B} \end{array} \right)$$

Which can be expressed as:

$$\frac{dA(t)}{dt} = B \times k_2 - A \times k_1 \quad (4.2)$$

The initial conditions of the system, at time $t=0$, are given by:

$$A(0) = A_0 \quad (4.3)$$

$$B(0) = B_0 \quad (4.4)$$

In our system, A represents the percentage of cells with an orientation ranging from 80° to 100°. At $t=0$, the cells are supposedly equivalently distributed, therefore:

$$A_0 = \frac{20}{180} = \frac{1}{9} \quad (4.5)$$

Moreover, to simplify our equation, we took advantage of a conservation law :

$$A(t) + B(t) = M \quad (4.6)$$

This simplification is the Achilles heal of this model. Indeed, the previous study of the cellular density demonstrated the non conservation of the total number of cells overtime. Nevertheless, here we are working with transformed data, where A and B are the percentage of cells oriented perpendicularly to the stretching axis and the non perpendicularly oriented cells in the population. To get the percentage of each cell population, the number of cells oriented (or non oriented) is divided by the total number of cells; the variation of the total number of cell is thus no more taken into account and M is constant ($A(t) + B(t) = M = 100\%$). In the future, we aim at improving this model by taking into account the variation of M by integrating the event of cell division or death in the model.

Anyway, the conservation law 4.6 allow us to rewrite the equation 4.2 as following:

$$\begin{aligned} dA/dt &= (M - A)k_2 - Ak_1 \\ &= -(k_1 + k_2)A + k_2M \end{aligned} \quad (4.7)$$

The differential equation 4.7 is verified by a solution with the general shape:

$$f(t) = \alpha(1 - \exp(-\beta t + \gamma)) \quad (4.8)$$

If we now replaced A by the previous expression, we obtain :

$$\begin{aligned} \frac{dA(t)}{dt} &= \alpha\beta \exp(-\beta t + \gamma) \\ &= -\beta(\alpha - \alpha \exp(-\beta t + \gamma)) + \alpha\beta \\ &= -\beta A + \alpha\beta \end{aligned} \quad (4.9)$$

To obtain an expression of the coefficient α, β and γ , we either replaced A by the previous expression in the equation 4.7, or calculate the limit of A when $t \rightarrow \infty$ and $t = 0$ we obtain :

$$\beta = k_1 + k_2 \quad (4.10)$$

$$\alpha = \frac{k_2 M}{\beta} = \frac{k_2 M}{k_1 + k_2} \quad (4.11)$$

and

$$\lim_{t \rightarrow -\infty} A(t) = A_\infty = \alpha \quad (4.12)$$

$$\begin{aligned} A(t=0) = A_0 &= \alpha(1 - \exp(\gamma)) \\ \Leftrightarrow \gamma &= \ln(1 - A_0/\alpha) \\ &= \ln(1 - A_0/A_\infty) \end{aligned} \quad (4.13)$$

The expression 4.8 was the one used to fit my experimental data in the following graphs, represented by a red dotted line, the coefficients obtained by theses fits are reported in the Table 4.1 and 4.2 .

To better understand the meaning of the parameters (α, β and γ) I plotted the function 4.8 in a simulator (<https://www.desmos.com>), the *Figure 4.10* represents this simulation with $a = \alpha$, $b = \beta$ and $c = \gamma$.

- α is equal to A_∞ in the model, it is the maximal cell response to the stretching (plateau).
- β is the sum of the transition rates (k_1 and k_2) in the model, it characterizes the slope of the first part of the fit, meaning the rapidity of the tissue to answer to the stretching. It is expressed in $Time^{-1}$, here h^{-1} .
- γ is an horizontal offset artificially introduced in the fit, to better resemble my experimental data. It has been added in the exponential because for $T=0$ my function is not null, indeed $A_0 = 1/9$.

To know when the cells start to respond to the cyclic stretching (t^*), we need to calculate when the function of the fit is equal to the control condition, meaning when the red and the black curves cross each other in the *Figure 4.10* respectively.

$$f(t^*) = f_{control} \quad (4.14)$$

$$\alpha(1 - \exp(-\beta t^* + \gamma)) = f_{control}$$

$$\exp(-\beta t^* + \gamma) = 1 - \frac{f_{control}}{\alpha}$$

$$t^* = \frac{\gamma - \log(1 - \frac{f_{control}}{\alpha})}{\beta} \quad (4.15)$$

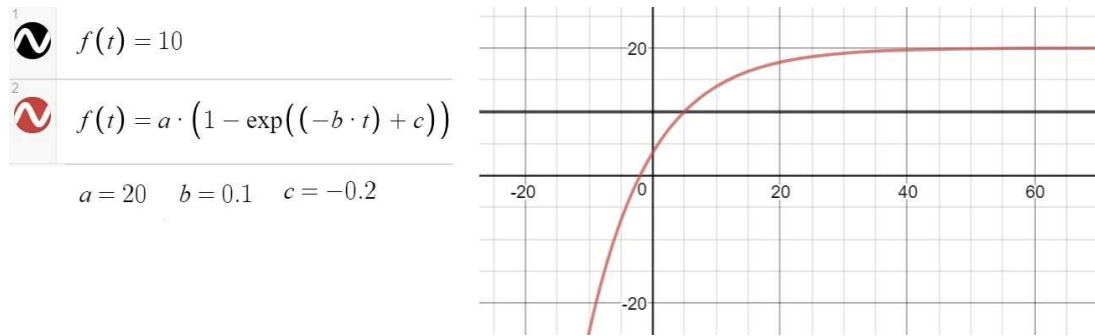


Figure 4.10: Simulation of the function 4.8 (in red) drawn on <https://www.desmos.com>

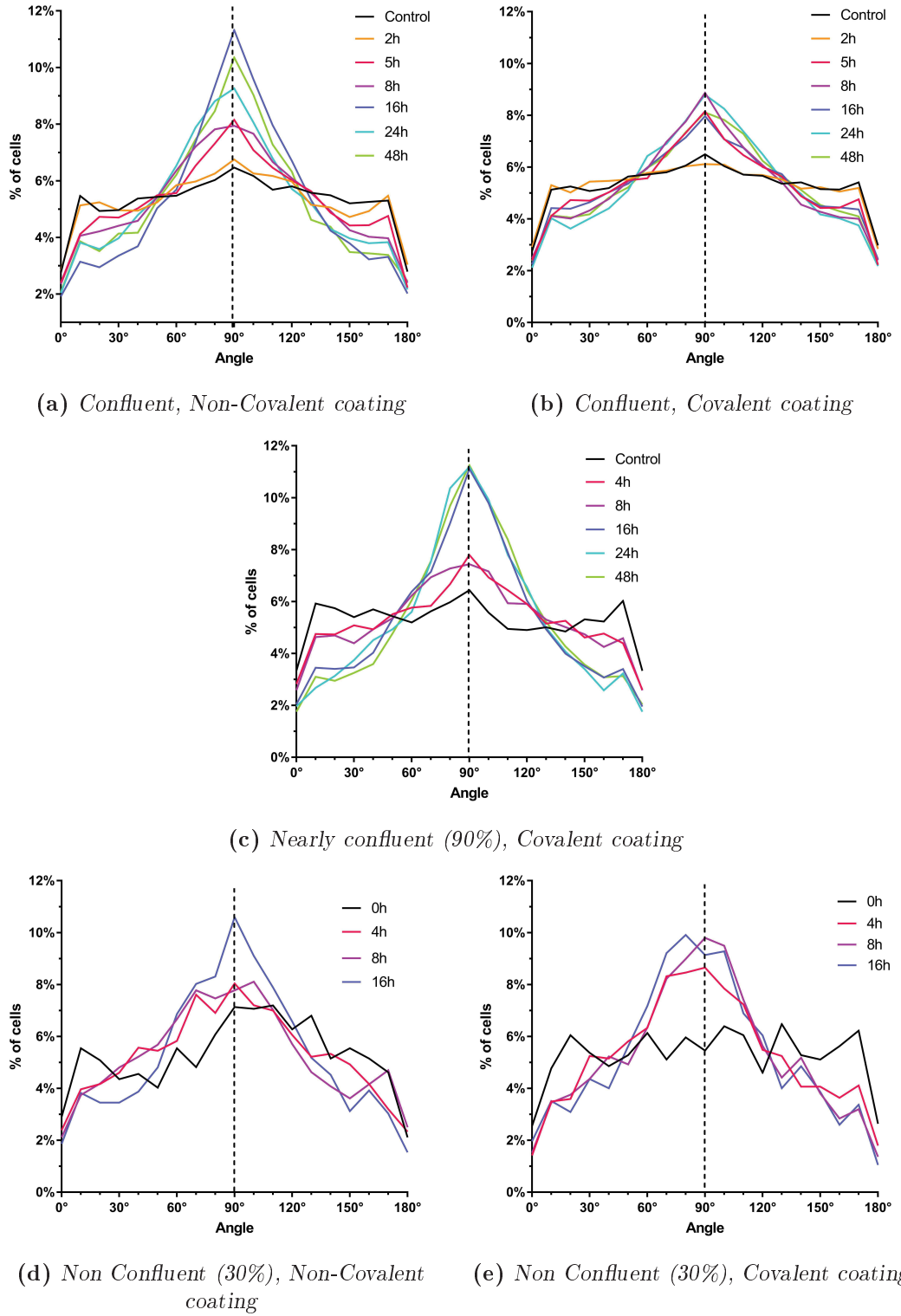
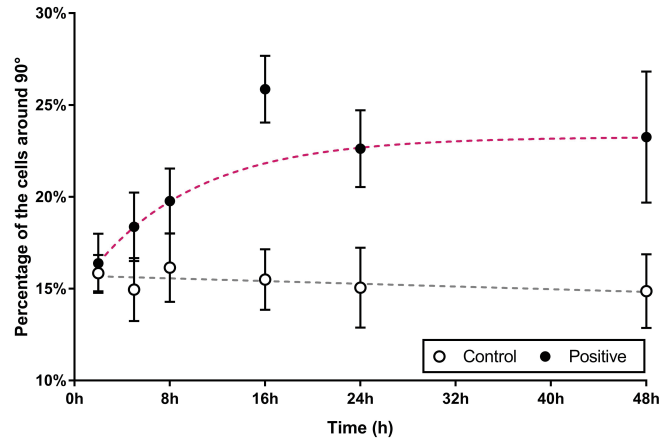
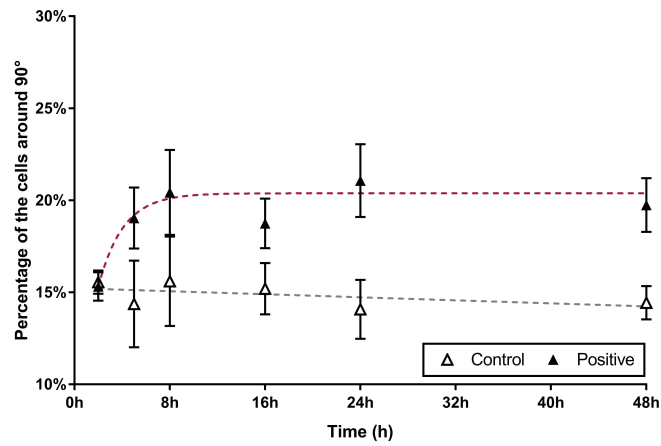


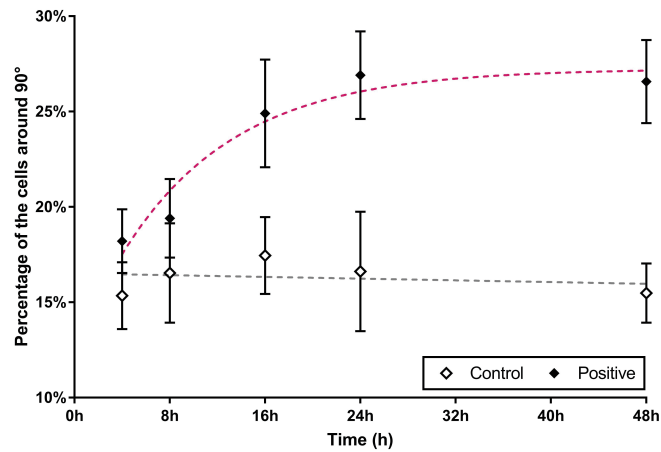
Figure 4.11: Distribution of the cellular orientation over time for a confluent monolayer with a non-covalent coating (a) and a covalent one (b), for a 90% confluent cellular layer with a covalent coating (c), and for a non-confluent (30%) cellular layer with a non-covalent (d) and a covalent (e) coating



(a) *Confluent, Non-Covalent*



(b) *Confluent, Covalent*



(c) *Quasi-confluent (90%), Covalent*

Figure 4.12: Variation of the percentage of cells perpendicularly oriented under the influence of the stretching for a initially confluent cellular layer on a (a) non-covalent and (b) covalent coating, as well as, a (c) quasi-confluent (90%) initial cellular layer on a covalent coating

As shown on Figure 4.11 whatever the coating conditions or the the initial confluency level of the cell monolayer, these data demonstrate that cells orientation is modified when cells are subjected to stretching. This data also evidences that cell response depends on the time of stretching, the longer they are stretched the more they get reoriented. And in all these conditions, the cells are mostly reoriented perpendicularly to the stretching axis. In terms of amplitude of the cells response, the maximal response corresponds to around 27% of the cells population oriented with an angle ranging from 80° to 100°.

In the following sections we will discuss both how the operating conditions (coating and confluency) will affect cell response in terms of percentage of the population affected by the reorientation and in terms of kinetics of the cells response.

Influence of the coating

Comparing *Figure 4.11* (a) and (b), we observe a difference regarding the cell response to stretching depending on the coating conditions. In both conditions, cells need at least 5 hours to start to reorient, but in the case of a non-covalent coating, this answer seems to increase with the stretching time, whereas it reached a plateau for a covalent coating after 5 hours. We can confirm this coating-induced difference by comparing the results obtained with cells initially stretched at subconfluency (*Figure 4.11* (e) and (d)) where the same trend can be observed. Another important observation is related to the amplitude of the reorientation, this data demonstrates that the percentage of cells reoriented in response to stretching is larger for non covalent coating than for the covalent coating conditions.

To quantify these observations we use the reduced percentages (*Figure 4.12*), corresponding to the cells with an orientation ranging from 80° to 100°, and the parameters (α , β and t^*) extracted from the fit reported in the Table 4.1.

The maximal cells response to the stretching is represented by α in the Table 4.1, these values show that an increased percentage of cells reorient during stretching for cells seeded on a non-covalent coating. The β parameter also depends on the coating conditions and shows that the covalent coating induces a cellular answer to stretching faster than a non-covalent coating. It is in agreement with previous studies where a covalent coating has been shown to transmit more efficacely the stretching to the cells than a non-covalent coating [223]. Finally, the lower t^* for the non covalent coating can be interpreted as an earlier response to the stretching for this coating compare to non-covalent condition. The response is in fact almost instantaneous ($t^* = 30mins$) for a non-covalent coating.

All together, these experiments have shown that a non-covalent coating will induce an instantaneous but slower cell reorientation to the stretching whereas a covalent coating will induce a delayed and faster answer. For these two coatings and for cells being initially confluent, the cyclic stretching induces an increase of cells aligned perpendicularly to the stretching axis of 53% and 33%, respectively $((N_{Stretch} - N_{Control})/N_{Control})$.

		Non linear Fit				Control
		α	β	γ	t^*	
(a)	Confluent, Non-Covalent	23 %	0,11 h^{-1}	-1 h	0.5 h	15 \pm 0,2%
(b)	Confluent, Covalent	20 %	0,48 h^{-1}	-0,4 h	2 h	15 \pm 0,3%

Table 4.1: Fit parameters and control for the Confluent, Non-covalent (a) and Covalent (b) experiments

Influence of the confluency

Comparing the *Figure 4.11* (b), (c) and (e) we will have access to the influence of the initial cell confluency. Indeed these graphs present the distribution of cells orientation for a covalent coating with different initial cells conditions, from 100% of confluency to 30%, over time. We observed the same kind of variations: a sudden response to the stretching followed by a plateau.

The similar value of t^* for the two sets of experiments (b) and (c) illustrates the same stretching time needed to trigger the cell reorientation, this time seems coating dependent as previously observed.

		Non linear Fit				Control
		α	β	γ	t^*	
(b)	Confluent, Covalent	20 %	0,48 h^{-1}	-0,4 h	2 h	15 \pm 0,3%
(c)	90% Confluent, Covalent	27 %	0,14 h^{-1}	-0,6 h	2 h	16 \pm 0,4%

Table 4.2: Fit parameters and control for the Confluent, Covalent (b) and Quasi-confluent (90%) covalent (c) experiments

Figure 4.12 shows that the cell response kinetics depends on the initial confluency of the cells as illustrated with the difference of β parameters obtained ranging from 0.14 to 0.48. The slower answer for the initial quasi-confluent (90%) experiments (c) can be interpreted as the possibility of the cells to relax through cell-cell junctions thanks to the lower confluency. The fact that the parameter β is similar for the set of experiments (a), confluent non-covalent, and (c), 90% confluent covalent, could be interpreted in terms of degrees of freedom. Indeed these two experiments possess one degree of liberty fewer than the set of experiments (b), either the non-covalent nature of the coating or the non-confluent initial configuration of the cells.

Therefore, to increase the rapidity of the cells reorientation under cyclic stretching we should decrease the degrees of freedom of the cells, meaning constrain them. This hypothesis will be tested and discussed in the results related to the 3D chips. Comparison of the parameter α (Figure 4.12 (b) and(c)) obtained on covalent coating with confluent or 90% confluent cells demonstrates an increase response for the quasi-confluent experiences with the highest percentage of cells oriented perpendicularly (around 27%) after 48 hours of stretching.

To summarize, starting the stretching on a confluent cell population induces a faster but limited cell reorientation compared to a quasi-confluent tissue and corresponds to an increase of 33% and 69% of the cells perpendicularly oriented respectively.

iii) How does cell recover the stretching influence?

After investigating cells response to stretching, we have been interested on how reversible is this response. To get a glimpse of the influence of the recover time on the cellular response, one set of experiment was performed with confluent cells on a covalent coating. After 24 hours of stretching we applied a resting time of 24 hours before fixation and staining. The results obtained are shown in the Figure 4.13. Strikingly, we show that if we allow the cells to relax after the stretching they almost go back to their initial situation. Indeed, after 24 hours of stretching 21% of the cell population has an orientation ranging from 80° to 100° while after 24 hours of recovery the perpendicularly oriented cells only represents $\approx 15,4\%$ of the population, which is close to the control condition where 14% of the population is randomly oriented around $90^\circ \pm 10^\circ$. Therefore, the recovery induces a lost of 80% of oriented cells. These preliminary data show that cell orientation in response to stretching seems reversible. More experiments should be performed to better characterize this recovery rate. In particular with this type of experiments we should be able to measure k_2 and consequently k_1 .

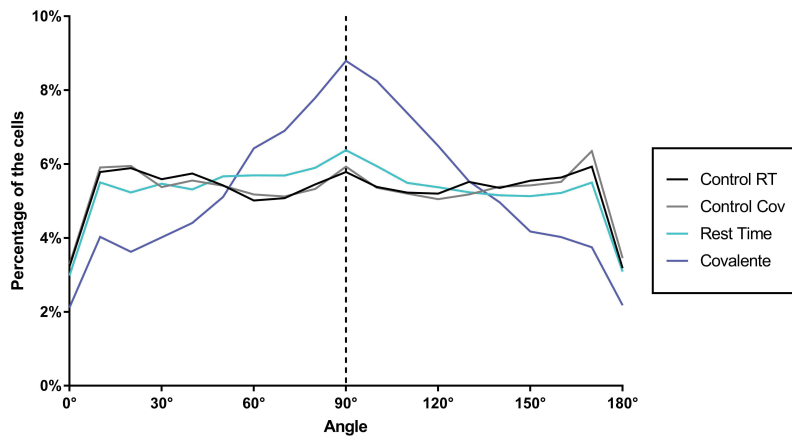


Figure 4.13: Distribution of the cellular orientations after 24 hours of stretching, with a direct or a delayed staining of the cells

iv) **How does stretching affect primary cell: Organoids ?**

To increase the potential of our stretching platform, a first set of experiments has been performed using primary cell; organoids. From this preliminary work we optimized the coating specifications, using a covalent coating of a mix of 1% Matrigel, collagen type I (0.2 mg mL^{-1}), and collagen type IV (0.4 mg mL^{-1}) as well as, the size of the organoids seeded on the chips (passaged one day before seeding) and the recovery time on the chips before stretching (2 days). From these preliminary results a slight decrease of the surface covered by the organoids after 24 hours of stretching has been observed (*Figure 4.14*). Nevertheless, more experiments are needed to properly characterize the influence of the stretching on the coverage.

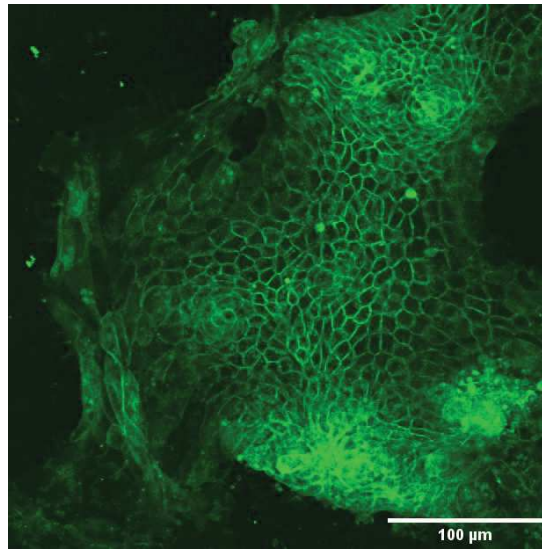


Figure 4.14: *Picture of no-stretched organoids on a 2D chip, with a staining of the plasma membrane*

In the next future, we will look at the cells density and orientation, using Lgr5-stained organoids to investigate how the stretching affect the positioning of the stem cells.

4.3 Influence of the stretching on 3D experiments

After having demonstrated that Caco2 cell lines are affected by stretching when grown on 2D, we aim at investigating how the 3D structure of their scaffold can affect their response to stretching. Because the subject of my PhD project is the intestine we designed 3D structures with shape and dimensions close to mice intestinal crypts. Furthermore we investigated the influence of the geometrical parameters by varying the crypt radius, depth and slope as illustrated in the *Figure 4.15*. The slope also conditions the exit diameter, indeed for a slope of 50° the exit diameter depends on the radius and the depth whereas for a slope of 75° it only depends on the bottom radius.

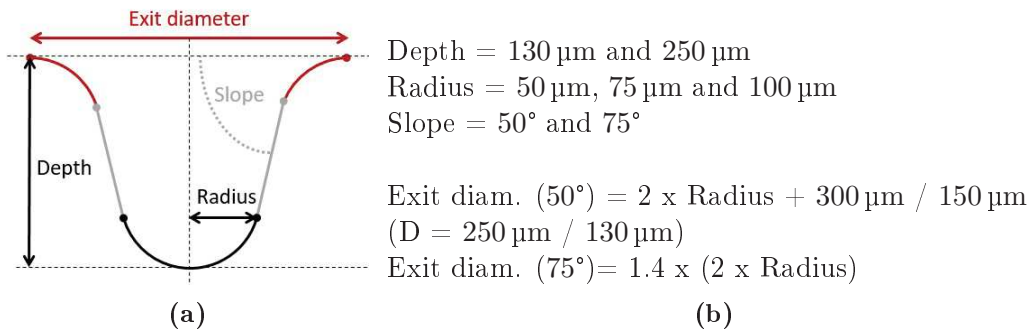


Figure 4.15: Representation of the geometric characteristics of the crypt (a) studied on the micro-fabricated scaffold with their variations (b)

Moreover, to study the influence of the confinement these set of parameters have been applied for the micro-fabrication of $2D^{1/2}$ and 3D patterns, called grooves and crypts in the following. The *Figure 4.16* represents the master mold, therefore the patterns obtained on the replicated chip are inverted.

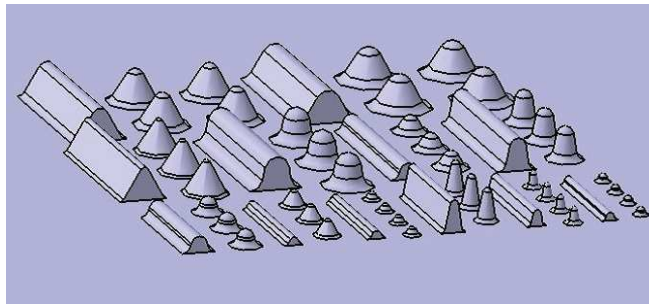


Figure 4.16: Representation of the $2D^{1/2}$ and 3D patterns of the 3D mold

Interestingly, whatever the shape and dimensions of the structures cells have been able to colonize the whole scaffold, as illustrated in the *Figure 4.17*, making these chips perfectly suited to study how cells respond to stretching when cultured on $2D^{1/2}$ and 3D patterns. For this set of experiments the stretching is applied perpendicularly to the axis of the grooves.

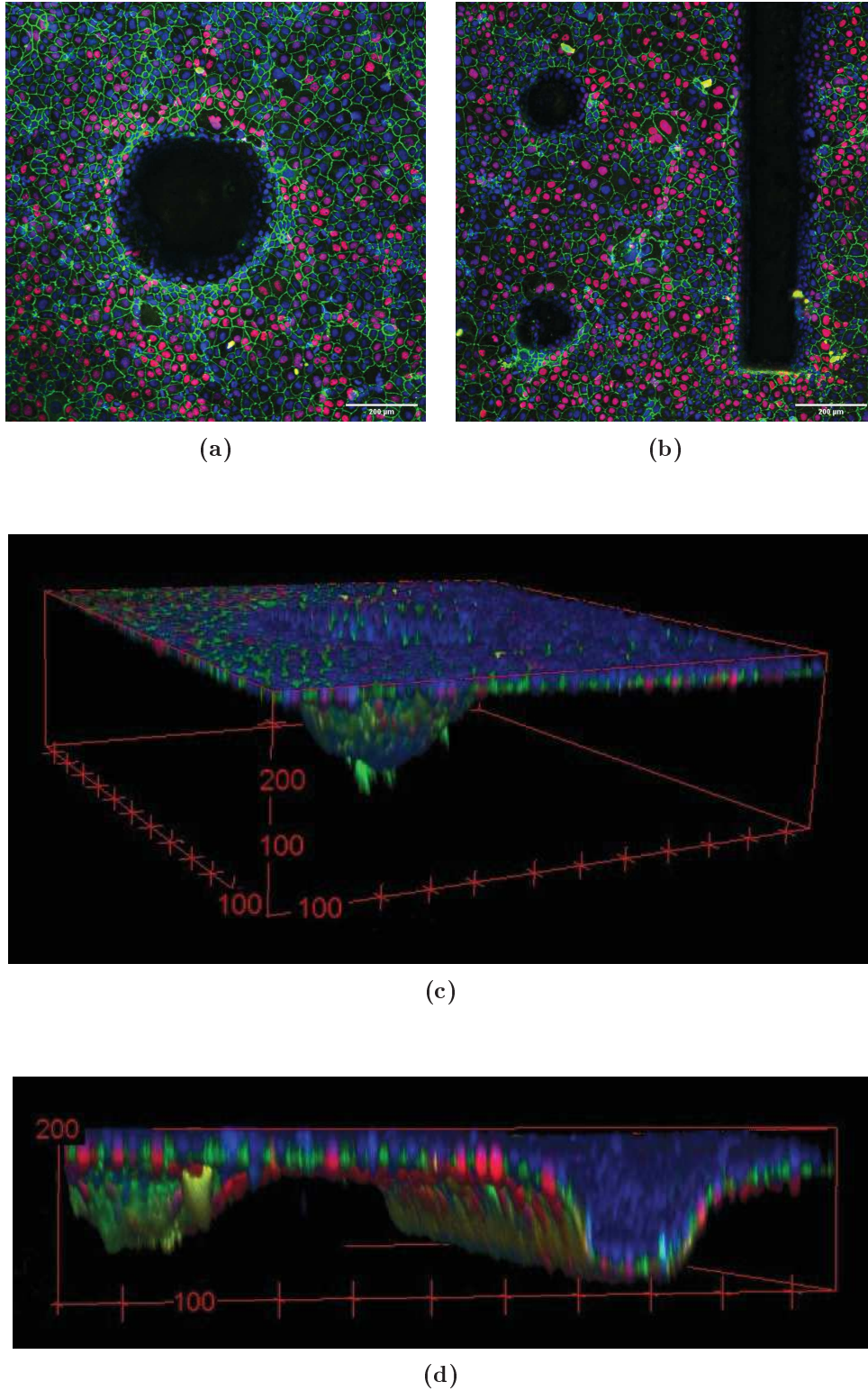


Figure 4.17: Picture of the surface of a 3D chip covered by Caco2 cells (a) and (b) [Scale bar = 200 μm], and 3D reconstructions of these patterns (c) and (d).
Dapi (blue) ZO1 (green) EdU (red)

i) How stretching does affect the covering of the patterns ?

For this set of experiments we performed a covalent binding of laminin on the scaffold, following by 3 days of proliferation to allow the cells to colonize all the structure, then the cells are stretched for 24 hours and directly fixed. Before evaluating how cells respond to stretching in 3D, we have observed in these conditions different cells behaviors: first, as expected, the cells follow the edges of the scaffold and cover completely the bottom of the crypts and grooves (*Figure 4.18 (a)*) or they detached from the curved surfaces and form suspended cell monolayers between the bottom and the adjacent walls of the crypts and grooves (*Figure 4.18 (b)*).

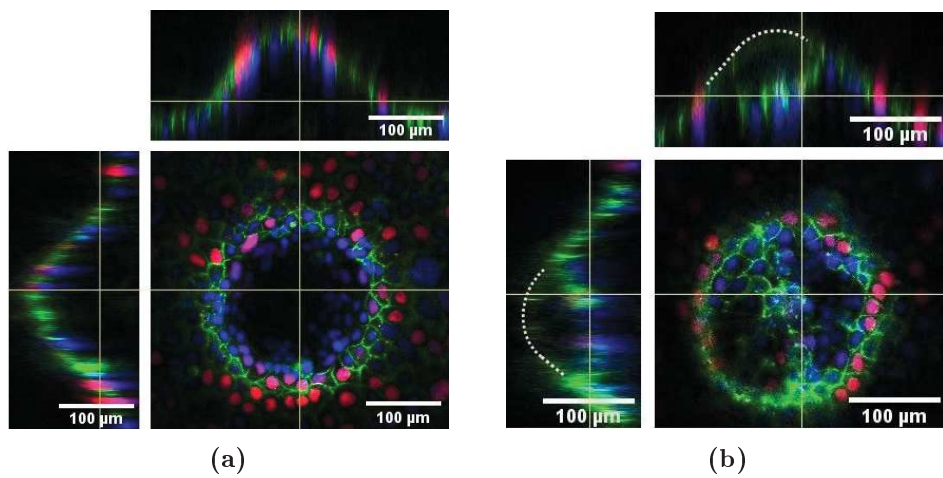


Figure 4.18: Orthogonal views of the crypts
($D=130\text{ }\mu\text{m}/r=50\text{ }\mu\text{m}/\text{slope}=50^\circ$) with (a) and without (b) suspended
layer. The original shape is represented by the white dotted lines.
Dapi (blue) ZO1 (green) EdU (red)

The formation of these suspended layers has already been reported by others [224, 231]. These observations of suspended cell layer open the question on how cells seeded on 3D scaffold colonize the scaffold and maintain their attachment to the imposed geometry.

The team of Viola Vogel has investigated the influence of the scaffold geometry, by varying the radius of circular semi-channels, and the cellular contractility on the formation of these suspended layers (*Figure 4.19*). Their experiments were performed on a glass substrate with semi-circular channels with a radius ranging from $300\text{ }\mu\text{m}$, $500\text{ }\mu\text{m}$ and $1000\text{ }\mu\text{m}$ coated with type I collagen. Two cell types were used for this study, endothelial cells and smooth muscle cells combined with the use of drugs (blebbistatin and $\text{TGF-}\beta$) to study the influence of the cell contractility on the formation of suspended layer.

From their work they observed an increase tissue detachment with decreased radius and increased contractility. They also use covalent and non covalent coating of collagen I and revealed that the rupture plane is localized along the substrate-coll I interface for non covalent coating while it takes place at the collagen integrin interface in case of covalent coating.

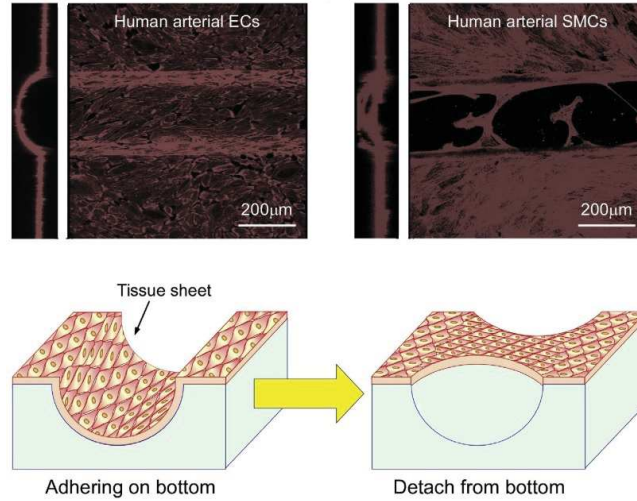


Figure 4.19: Representation of the formation of suspended monolayer, adapted from [224]

In our case, we will be able to investigate the same phenomena but with more complex structure: grooves as in the Vogel's paper as well as in crypt and we will also investigate how the mechanical forces exerted on cells will affect the formation of these suspended structures.

Suspended cell monolayers in crypts

To characterize the formation of these suspended cell monolayers in my experiments, in function of the geometric parameters and the stretching, first we counted the number of crypts with suspended layer in function of the total number of crypts. This qualitative study was only performed on 6 crypts for each condition, stretching versus control. Therefore these preliminary experiments are only discussed in terms of tendencies, and in a near future complementary experiments will be performed to either corroborate or contradict these tendencies.

The main tendency observed is the influence of the slope, when it becomes smoother (50°) we lost the formation of the suspended cell layers. In this case the slope directly influences the exit diameter, therefore we can reinterpret this trend as function of the exit diameter: an increased exit diameter (due to a larger bottom radius or a deeper crypt or a smoother slope) reduced the formation of the suspended cell monolayers, similarly to the conclusions of the team of Viola Vogel. Moreover, the influence of the stretching can not be properly estimated.

Formation of suspended cells monolayers in grooves structures

The results obtained with the crypts showed the presence of these cells suspended monolayers however it was difficult to extract trends regarding the effect of the geometrical constraints and of stretching on this suspended layers formation. We will now investigate if $2D^{1/2}$ structures will allow to decipher better the suspended layers formation.

To characterize the formation of the suspended monolayers we measured the total area of the bottom part of the grooves and the areas free of any cells. These empty areas at the bottom of the grooves correspond to the spaces below the suspended monolayers, as illustrated in the *Figure 4.20*. Therefore, we calculated the ratio between these two values to estimate the proportion of suspended layers in the grooves. The results are reported in the Table 4.3, where 0% corresponds to no suspended monolayers, in other words the bottom part is completely covered by cells.

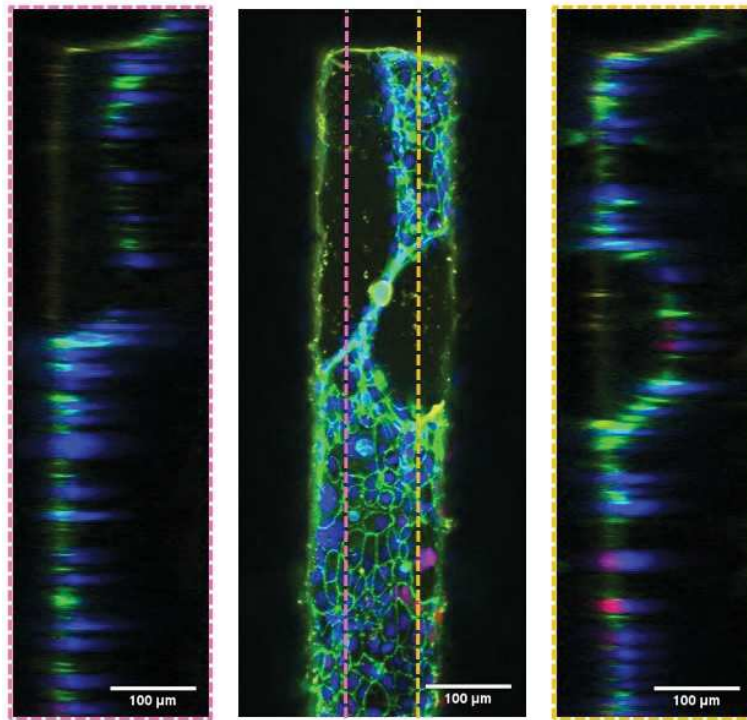


Figure 4.20: Pictures of the bottom of a groove
(Depth=130 μm /Radius=75 μm /Slope=75°) with orthogonal views of
the suspended cells monolayers
Dapi (blue) ZO1 (green) EdU (red)

We can first noticed that for these $2D^{1/2}$ geometry all the parameters seem to have an influence on the formation of the suspended layer. In general, increasing either the radius or the depth or decreasing the slope, that is the increase of the exit diameter, induces the diminution of the formation of suspended layers.

Moreover, for the smaller radius (50 μm) the stretching seems to prevent the apparition of suspended monolayers for both depths. This effect could be explained by the unstable form of the suspended layer destabilized by the cyclic stretching, indeed by definition these suspended cell layers can not be stabilized by the interaction with the surface therefore more experiments will be performed to both understand the underlying mechanisms and confirm the observed trends.

	Depth				
Radius	130 μm		250 μm		Slope
	Cont.	Pos.	Cont.	Pos.	
50	41 ± 19%	28 ± 7%	19 ± 5%	9 ± 5%	50°
75	10 ± 4%	13 ± 9%	3 ± 4%	3 ± 4%	
100			0%	2 ± 3%	
75	24 ± 14%	12 ± 14%	11 ± 4%	11 ± 4%	75°
100			2 ± 2%	0%	

Table 4.3: *Percentage of suspended layers in the grooves*
Cont. = control condition / Pos. = stretched condition

ii) Influence of topography on the cellular alignment in the grooves

Once discussed the formation of these suspended monolayers, we will now investigate cells response to stretching for cells that remain attached to the scaffold. In order to understand how cells are affected by stretching in 3D and to discriminate the effect of confinement from the effect of stretching, these experiments will be compared with cells seeded on the 3D scaffold without stretching and to cells stretched in 2D. To do so the same parameter has been analysed : cells orientation.

Cells orientation will be presented and discussed as a function of the scaffold geometry: radius, slope and depth as well as with and without stretching. For these experiments the chips have been stretched perpendicularly to the axis of the grooves. Moreover to estimate properly the distribution of the cellular orientation a minimum number of cells is needed, therefore this study has only been realised on the $2D^{1/2}$ geometry (grooves). The *Figure 4.21* represents the distribution of the cellular orientation of the cells at the bottom of the grooves in all conditions.

First we can see that as expected, the geometry by itself induces the cells alignment along the axis of the grooves. Indeed, without any stretching the cells preferentially lean toward an angle of 90° which corresponds to an angle of 0° regarding the grooves axis, this phenomenon is widely spread and is known as the contact guidance [166, 232]. This cells response seems dependent on the geometrical parameters of the grooves (depth / radius / slope) and more interestingly seems to be amplified by the stretching. Indeed, for this experiment the stretching direction was perpendicular to the groove axis, therefore the contact guidance effect and the cells reorientation induced by the

stretching are parallels. Future experiments will be performed in the opposite direction to study the competition between these two effects.

Anyway, to characterize the effect of the stretching and the contact guidance for every geometry we will study them individually in function of one geometrical parameter.

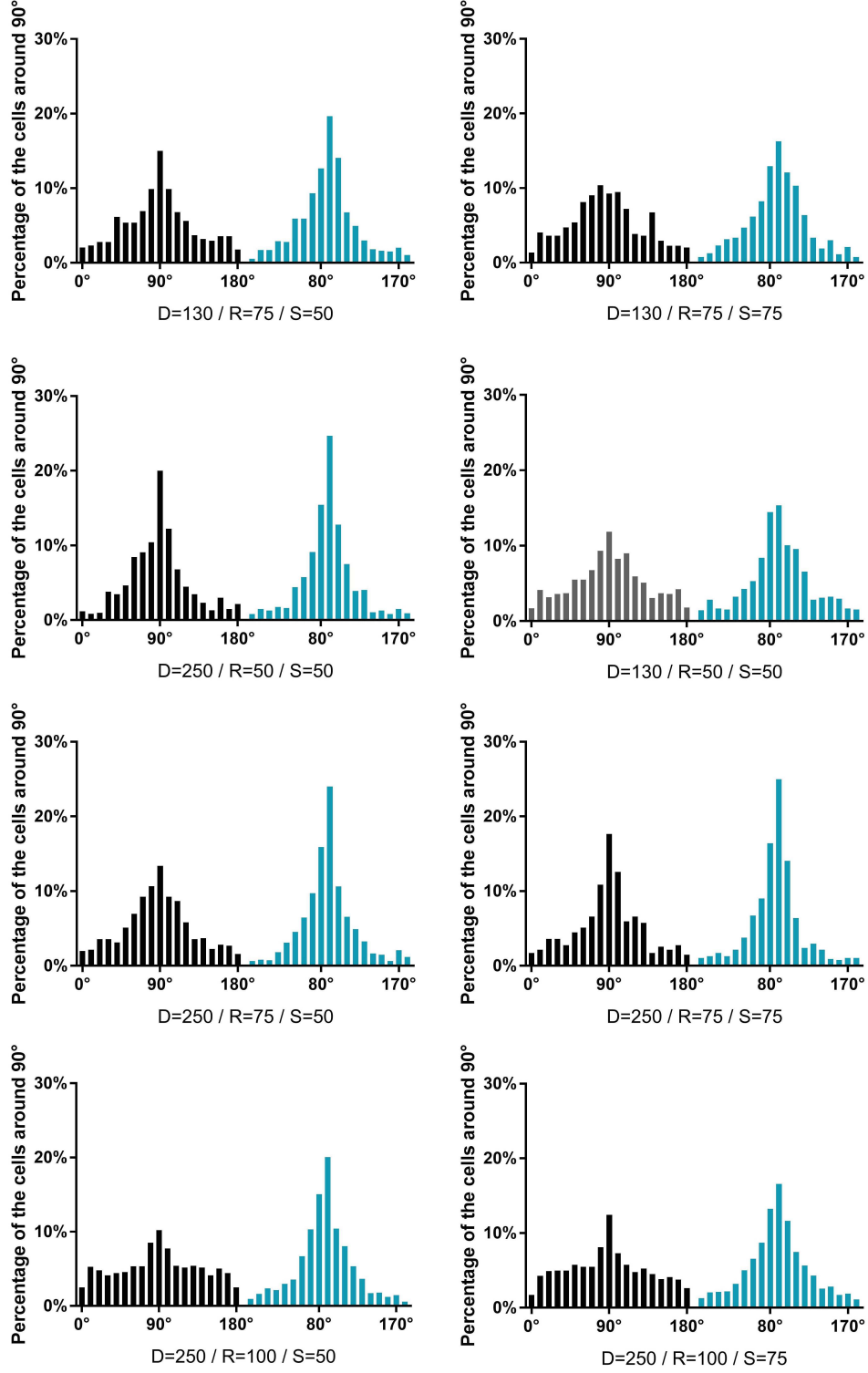


Figure 4.21: Angular distribution of the cells for all the $2D^{1/2}$ patterns of the 3D mold.
 $D=\text{depth}(\mu\text{m})$ / $R=\text{radius}(\mu\text{m})$ / $S=\text{slope}(^{\circ})$

The influence of the Radius will be estimated comparing the geometries (a), (b) and (c) *Figure 4.22* where only the radius is changing from 50 to 100 μm . To compare these conditions we will use the reduced percentages, meaning the percentage of cells with an angle ranging from 80° to 100° , reported in the Table 4.4.

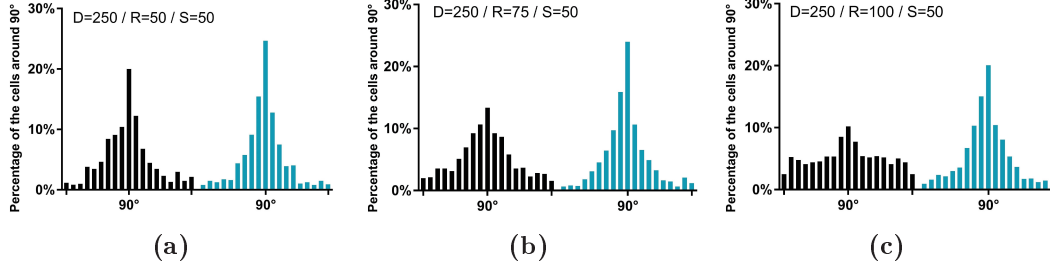


Figure 4.22: Angular distribution of the cells on the $2D^{1/2}$ patterns with a radius of (a) 50 μm , (b) 75 μm and (c) 100 μm
 $D=\text{depth}(\mu\text{m})$ / $R=\text{radius}(\mu\text{m})$ / $S=\text{slope}(\circ)$

First we can observe that the cells distribution of the cells orientation is narrower for the smallest radius, the effect is very similar to what has been reported in the literature ([166, 232]). Indeed, increase radius induces a decrease confinement of the cells which is translated by a decrease effect of the contact guidance. More interestingly, we demonstrate that stretching of the 3D structure also induces an increase of the percentage of cells oriented perpendicularly to the stretching axis. This effect seems more pronounced for larger radius, however it should be confirmed by a larger set of experiments. When comparing the amplitude of stretching effect, it seems that stretching cells in 3D amplifies their response compared to 2D conditions by a factor at least of 2.

Radius	50 μm		75 μm		100 μm		Flat	
Condition	Cont.	Pos.	Cont.	Pos.	Cont.	Pos.	Cont.	Pos.
Cells percentage ($\theta = 90^\circ \pm 10^\circ$)	38%	48%	29%	45%	23%	40%	14%	21%
Contribution of confinement : $\%_{\text{Cont.3D}} - \%_{\text{Cont.2D}}$	24%		15%		9%			
Contribution of stretching : $\%_{\text{Pos.3D}} - \%_{\text{Cont.3D}}$		10%		16%		17%		7%

Table 4.4: Percentage of cells oriented along the grooves axis, perpendicularly to the stretch axis for grooves of 250 μm depth with a radius ranging from 50 μm to 100 μm .
 $\text{Cont} = \text{control condition}$ / $\text{Pos.} = \text{stretching condition}$

The effect of the Depth has been estimated by comparing the geometries two by two (a) / (b) and (c) / (d) *Figure 4.23* where depth is the only varying parameter, the reduced percentages are reported in the Table 4.5.

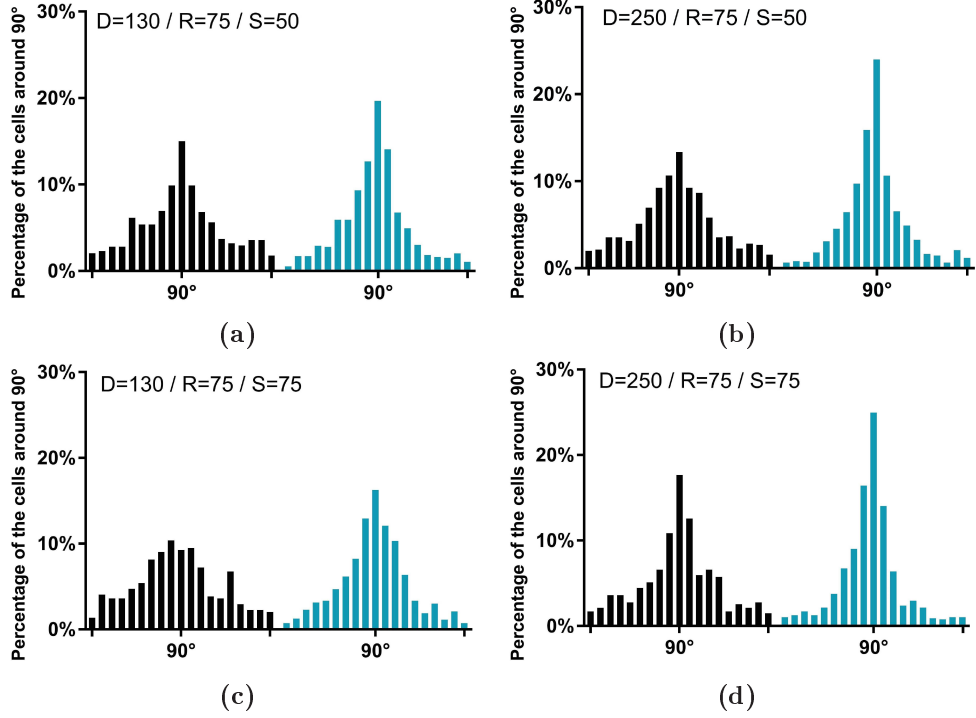


Figure 4.23: Angular distribution of the cells on the $2D^{1/2}$ patterns
with a depth of (a) and (c) 130 μm and (b) and (d) 250 μm
 $D=\text{depth}(\mu\text{m}) / R=\text{radius}(\mu\text{m}) / S=\text{slope}(^{\circ})$

From the Table 4.5 two observations can be made. First, the impact of the depth on the contact guidance seems modulated by the slope. Indeed for a smoother slope, the increase of the depth does not influence the contact guidance effect, whereas for a higher slope the effect of the contact guidance on the cell orientation increases with the depth. As previously, we observed that whatever the conditions, the cells response to stretching is amplified in 3D and this effect is slightly more pronounced for deeper grooves independently to the slope value.

Depth	130 μm		250 μm		Slope	Flat	
Condition	Cont.	Pos.	Cont.	Pos.		Cont.	Pos.
Cells percentage ($\theta = 90^\circ \pm 10^\circ$)	30%	41%	29%	45%	50°	14%	21%
Contribution of confinement $\%_{\text{Cont.3D}} - \%_{\text{Cont.2D}}$	16%		15%				
Contribution of stretching $\%_{\text{Pos.3D}} - \%_{\text{Cont.3D}}$		11%		16%			7%
Cells percentage ($\theta = 90^\circ \pm 10^\circ$)	26%	36%	36%	50%	75°	14%	21%
Contribution of confinement $\%_{\text{Cont.3D}} - \%_{\text{Cont.2D}}$	12%		22%				
Contribution of stretching $\%_{\text{Pos.3D}} - \%_{\text{Cont.3D}}$		10%		14%			7%

Table 4.5: Percentage of cells oriented along the grooves axis, perpendicularly to the stretch axis for grooves with a radius of 75 μm .
Cont = control condition / Pos. = stretching condition

The effect of the Slope has been estimated by comparing the scaffold geometry two by two (a) / (b) and (c) / (d) *Figure 4.24* where only the slope changes, the reduced percentages are reported in the Table 4.6.

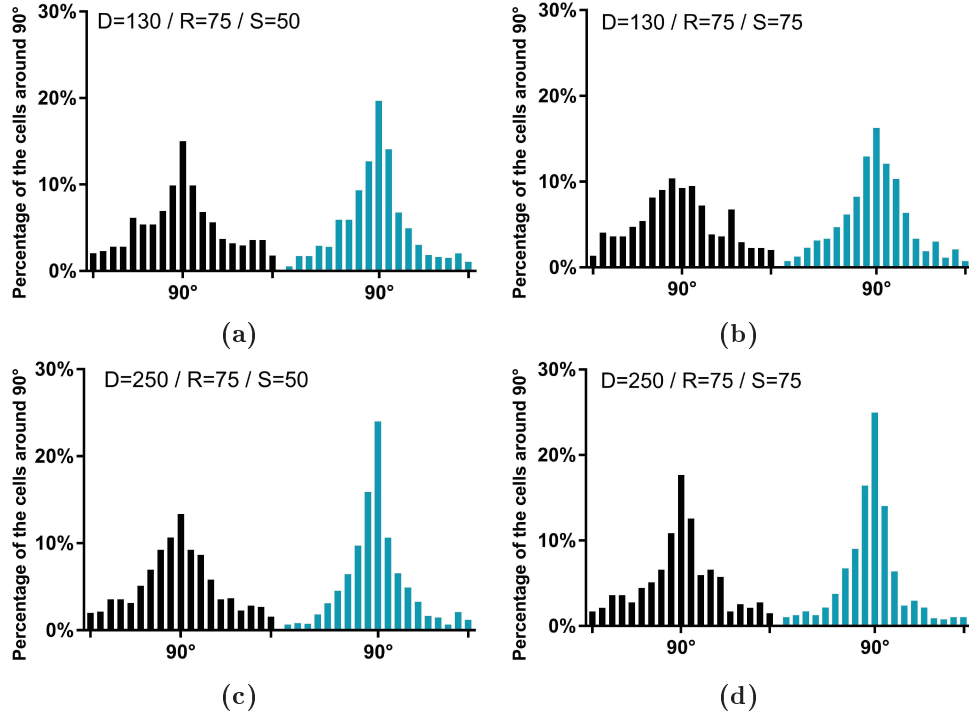


Figure 4.24: Angular distribution of the cells on the $2D^{1/2}$ patterns with a slope of (a) and (c) 50° and (b) and (d) 75°.
 $D = \text{depth}(\mu\text{m}) / R = \text{radius}(\mu\text{m}) / S = \text{slope}(\circ)$

Similarly to the last observations, we observed increased effect of the contact guidance with the slope for deeper grooves only, in contrary the amplification of the stretching effect in 3D is observed whatever the depth and even in larger extent in deeper grooves. These results also show that this amplification does not seem to depend on the slopes of the grooves.

Slope	50°		75°		Depth	Flat	
Condition	Cont.	Pos.	Cont.	Pos.		Cont.	Pos.
Cells percentage ($\theta = 90^\circ \pm 10^\circ$)	30%	41%	26%	36%	130 μm	14%	21%
Contribution of confinement $\%_{\text{Cont.3D}} - \%_{\text{Cont.2D}}$	16%		12%				
Contribution of stretching $\%_{\text{Pos.3D}} - \%_{\text{Cont.3D}}$		11%		10%			7%
Cells percentage ($\theta = 90^\circ \pm 10^\circ$)	29%	45%	36%	50%	250 μm	14%	21%
Contribution of confinement $\%_{\text{Cont.3D}} - \%_{\text{Cont.2D}}$	15%		22%				
Contribution of stretching $\%_{\text{Pos.3D}} - \%_{\text{Cont.3D}}$		16%		14%			7%

Table 4.6: *Percentage of cells oriented along the grooves axis, perpendicularly to the stretch axis*

To summarize the 3D geometry increases the cell reorientation by itself with a significant effect of the radius and a correlated effect of the slope and the depth. This reorientation is therefore increased by cyclic stretching by approximately 41%. The impact of the stretching by itself seems amplified with an average contribution of 12% compared to 7% for 2D experiments. This experiment underlines the need to the combination of these two simulations (topography and stretching) to maximize the cell response with a maximum of 50% of the population with an angle ranging from 80° to 100° for the grooves with the highest geometrical constraints ($D=130 \mu\text{m}/R=50 \mu\text{m}/S=50^\circ$; $D=250 \mu\text{m}/R=50 \mu\text{m}/S=50^\circ$; $D=250 \mu\text{m}/R=75 \mu\text{m}/S=75^\circ$). Indeed, the 3D architecture may lead to different mechanical stress distributions along the z-axis similar to mechanical stress distribution along the crypt-villus axis.

Previous gut-on-chip platforms have already demonstrated either the importance of the 3D architecture or the influence of the stretching to increase the cellular polarization and differentiation [84, 116, 117]. Therefore the next generation of gut on chip should combine these two simulations, a path already explored by our team thanks to the platform developed along my PhD project.

Nevertheless still plenty of work has to be done for a proper characterization of this platform such as replicating the experiments to increase the statistical analysis, estimating the effect of the stretching on the cells that are located along the edges of the grooves and not only observing the cells at the bottom of the structure, as well

as studying the spatial distribution of the proliferative cells along the 3D structure. Moreover, the use of a collagen coating instead of a laminin one could change the cellular response induced by the cyclic stretching thanks to the long range communication enhanced by the collagen fibers [233].

4.4 Conclusion

In this chapter we have investigated how cells are affected by stretching both in 2D and 3D. A first set of experiments performed in 2D has evidenced the importance of the coating techniques used. Indeed, only a covalent coating was strong enough to support the traction forces, induced by the cells during stretching, without detachment of the cellular layer. We also shown that using covalent coating conditions, the cells proliferation does not seem to be significantly affected by stretching. To evaluate individual cells response to stretching, we characterised the dynamics of the cellular reorientation induced by the stretching over time, for different coating and confluency conditions. To compare the kinetics of the cells response, we used a simple chemical model and we were able to estimate the kinetics parameters as well as the amplitude of the response. We showed that both depends on the coating conditions and on the initial confluency level of the cells. In particular, a non covalent coating induced an instantaneous but limited cells response while a non confluent cells monolayer allows more cells to respond to the stretching. Finally, the strongest response is obtained for a quasi-confluent cell monolayer (90%) on a covalent coating. To further investigate the effect of the confluency the missing time points (24 hours and 48 hours) of the non-confluent set of experiments (30%) are currently performed by Moencopi Bernheim-Dennery and should be included for the oral presentation.

Interestingly, we also showed that after 24 hours of relaxation after 24 hours of stretching, cells almost recover their initial orientation. These experiments should allow us to extract more precisely the k_1 and k_2 of the orientation equilibrium. In a next future we aim at investigating how long should be the relaxation time to completely recover the initial orientation and how the relaxation time is correlated with both the stretching time and the coating conditions (nature and techniques).

Finally, the 3D experiments were performed in order to really decipher the effect of cells stretching in 3D. To do so we have compared these conditions, with non stretched 3D structure and stretched 2D structure. These experiments have shown that as expected cells orientation depends on the geometry, and that this contact guidance depends mainly on the grooves radius as well as on the slope and depth of the structure. More strikingly we have shown that the response of cells stretched is amplified in 3D compared to 2D experiments, this amplitude being in particular dependent on the grooves radius. These results confirm our expectation that the next generation of gut

on chip should combine 3D structure with stretching.

Despite being interesting results on the effect of stretching on intestinal cells, there are plenty of experiments to run to move one step further. With the Caco2 cells, we aim also at improving the imaging to get complete view of cells response in 3D as well as, we aim at better investigate cells response by looking at cells proliferation, polarisation and differentiation. Finally as illustrated by very preliminary experiments our ultimate goal will be to perform such experiments with organoids to get closer to the *in vivo* complexity. Next to my main project the observation of the suspended cells monolayer raises an interesting issue of tissue engineering and cells response. Indeed, this unexpected cells response to geometrical constraints opens a new project for the next: Can we characterize the formation of the suspended cells monolayer in function of the geometries ? And at which extent these structures can resist stretching ?

Conclusion and perspectives

My PhD project is part of the *Gut-on-chip* field, therefore it aims at developing a *Gut-on-chip* model that recapitulates as much as possible the intestine complexity.

During the first part of my PhD I have been involved in the development of an original Gut-on-chip platform that recapitulates for the first time both the epithelial and stromal compartment thanks to collagen molding in 3D. This Gut-on-chip allows to address new questions in particular regarding the interplay between the epithelial and the stromal compartments.

Despite a high level of biomimicry, this Gut-on-chip does not recapitulate perfectly the differentiated cells positioning. Moreover, one of the missing part of this platform is the absence of peristaltic motion. It is in this context that we decided to study the influence of mechanical constraints on the intestinal cells behavior. This work represents the main objective of my PhD and more particularly we aimed at mimicking the peristaltic motion on chip. Therefore, we investigated how cyclic stretching affects intestinal cells behavior and how the geometry of the scaffold influences this response.

These questions were addressed through the development of a versatile gut-on-chip platform recapitulating both the 3D architecture and the mechanical micro-environment of the intestine. Indeed, cells stretching and 3D scaffold geometry have already demonstrated their potential in term of cellular differentiation and proliferation [116–118, 182], therefore they are important intestinal features to recapitulate on a gut-on-chip platform. However, they have never been combined in a gut-on-chip platform. Indeed the widely used Gut-on-chip platform developed by Donald E. Ingber recapitulates the peristaltic motion but lack the 3D geometry. In Ingber’s experimental conditions, self developed villi-like structures by the intestinal cells have been observed after 100 hours of stretching [84, 107, 120, 121, 183]. However, it represents an incomplete structure of the intestine missing the crypt compartment as well as the stromal core of the villi arising questions about the biomimicry of these structures.

On the other hand, my Gut-on-chip platform recapitulates both the 3D architecture, thanks to a micro-milled mold used to fabricate 3D stretchable PDMS chips with intestinal structures, and the peristaltic motion mimicked by a home-made stretcher able to stretch these 3D chips at a tunable amplitude and frequency. Therefore, our Gut-on-chip allowed first the study of the influence of the stretching on an intestinal cell monolayer on a 2D and 3D scaffold. We have characterized the cells response (cells reorientation under stretching) as a function of the substrate coating and the initial cell confluency before stretching. This study rises interesting questions regarding the strength balance between the PDMS membrane and the ECM proteins, in particular we showed that long stretching time induces cellular detachment in the case of a non-covalent coating. Which demonstrates the weak link between the PDMS and the adhesion molecules for this coating, Moreover the largest cellular reorientation was achieved for cells stretching starting on non confluent cells, this rises question about the influence of the cell-cell junction on cells response to stretching. In a next future, complementary experiments will be performed to know if a complete cell reorientation can be achieved by decreasing the initial confluency.

The stretching of the intestinal cells on a 3D scaffold has shown the influence of the geometry of the scaffold on the cellular alignment, already widely known as contact guidance. Besides, this study has also shown that the combination of the 3D structure and the stretching allow to reach an unprecedented level of cell alignment, demonstrating the need to combine these two stimuli to attempt to recreate a more faithful in-vitro intestinal model. In particular we shown, that cells stretching response in 3D is not only the sum of contact guidance and 2D stretching response, but that growing cells in 3D amplifies the response to stretching. Interestingly, the effect of the stretching was not uniform between the 3D structures arising the question about the distribution of the force among the 3D structure. This study represents a first step and was only performed for one time point, therefore it will be completed in a near future by more time points to study the dynamics of this alignment as well as the location of the proliferative cells and the impact on the cellular polarisation and differentiation of the combination of the 3D geometry and the stretching.

Regarding the intestinal function we can also wonder if the cellular reorientation is related to the intestinal barrier property. Indeed previous studies have demonstrated both an increased permeability of FITC-dextran and a decreased transepithelial electrical resistance (TEER) in response to cyclic stretching [120, 183] whereas the 3D structure alone has been shown to increase the TEER [115, 116], without studying the cells orientation. Therefore it could be interesting to investigate how it is correlated in our case.

Finally, almost all the experiments performed during my PhD work have been done using Caco2 cells, it is now crucial to move forward using organoids. Preliminary experiments have demonstrated the feasibility of this approach, allowing more biomimetic study of stretching on intestinal cells. In a more long term a new generation of gut on chip platform is envisioned. Indeed, during my PhD I demonstrated the interest of my platform to address biophysical questions. However, there is still a missing feature: the dynamic control of the interface of the intestinal barrier between the lumen covered with epithelial cells in contact with bacteria and the stromal compartment. Indeed several studies have shown the importance of the chemical gradients to achieve cells differentiation and positioning along the crypt-villus axis [116–118]. We are currently considering how this dynamic control could be implemented in the next future.

Appendix A

Immunostaining protocol

1. **Permeabilization** using Triton (X-100) at 0.5 % for 5 minutes at room temperature
2. Rinse 3 times (5 min) and 1 time (10min) with PBS at room temperature
3. **Saturation** using BSA at 4% in PBS, 2 hours at room temperature
4. Rinse with PBS for 10 minutes
5. **Staining** using primary antibody (ZO1: 1/75) for 3 hours for the flat chip at room temperature or overnight at deg 4 for the 3D chip
6. Rinse 3 times (5 min) and 1 time (10min) with PBS at room temperature
7. Secondary antibody (*Alexa Fluor Plus*: 1/100) for 30min for 2D chip or 1 hour for 3D chip at room temperature protected from light
8. Rinse 3 times (5 min) and 1 time (10min) with PBS at room temperature
9. **Mounting** using one drop of *EverBrite Hardset Mounting Medium* overnight protected from light

Appendix B

Code of the first stretchers

```
// ***** Attribution des pin
int pin_direction = 13;
int pin_step = 12;
int pin_endstop_moteur =4;
int pin_endstop_puce =2;
int pin_MS1 = 8;
int pin_MS2 = 9;
int pin_MS3 = 10;

// ***** Information utiles
direction HIGH = direction vers le bloc support
direction LOW = direction vers le moteur
MS1=MS2=MS3 = LOW 1 pas
MS1 = HIGH MS2=MS3=LOW 1/2pas
MS1 = LOW MS2= HIGH MS3=LOW 1/4pas
MS1=MS2 = HIGH MS3=LOW 1/8pas
MS1=MS2=MS3 = HIGH 1/16pas

/*_____Fonctions_____*/
//XXXXXXXXX* Fonction Setup
void setup()
{ // Definition des entrees et sorties
pinMode (pin_direction, OUTPUT);
pinMode (pin_step, OUTPUT);
pinMode (pin_MS1, OUTPUT);
pinMode (pin_MS2, OUTPUT);
pinMode (pin_MS3, OUTPUT);
```

```

pinMode (pin_endstop_moteur, INPUT);
pinMode (pin_endstop_puce, INPUT);
Serial.begin(9600);

Initiation ();
//Oscillations(Nombre_de_pas);
Oscillations (500); }

//XXXXXXXXXXXXXXXXXXXX* Fonction Initiation
void Initiation ()
{
// POSITION INITIALE
// Direction moteur
digitalWrite (pin_direction, LOW);
// MS1 = HIGH MS2=MS3=LOW -----> 1/2pas
digitalWrite (pin_MS1, HIGH);
digitalWrite (pin_MS2, LOW);
digitalWrite (pin_MS3, LOW);

while (digitalRead(pin_endstop_moteur) != LOW)
    { digitalWrite(pin_step, HIGH);
      delay(1);
      digitalWrite(pin_step,LOW);
      delay (1);  }

//CALIBRATION
// Direction bloc fixe
digitalWrite (pin_direction, HIGH);
// MS1=MS2 = HIGH MS3=LOW -----> 1/4pas
digitalWrite (pin_MS1, LOW);
digitalWrite (pin_MS2, HIGH);
digitalWrite (pin_MS3, LOW);

double x=0;

while (digitalRead(pin_endstop_puce) != LOW)
    { digitalWrite(pin_step, HIGH);
      delay(1);
      digitalWrite(pin_step,LOW);
      delay (1);
      x++;      }

```

```
//POSITION DE DEPART
// direction moteur
digitalWrite (pin_direction, LOW);
// MS1=MS2 = HIGH MS3=LOW 1/4pas
digitalWrite (pin_MS1, LOW);
digitalWrite (pin_MS2, HIGH);
digitalWrite (pin_MS3, LOW);

double y = 0;
y=((1*x)/5.2);

for (int i=0; i<= (int)y; i++)
    { digitalWrite(pin_step, HIGH);
      delay(1);
      digitalWrite(pin_step,LOW);
      delay (1);    }
}

//XXXXXXXXXXXXXXXXXXXXXXXXXXXX* OSCILLATIONS
void Oscillations (int pas)
{ int y=1;
  double pause=0;
  pause = (2.5*1000)/(2*pas);

  // MS1=MS2 = HIGH MS3=LOW 1/8pas
  digitalWrite (pin_MS1, HIGH);
  digitalWrite (pin_MS2, HIGH);
  digitalWrite (pin_MS3, LOW);

  while ( y !=0)
    {      digitalWrite(pin_direction, LOW);
      for(int i=0; i<=pas; i++)
        { digitalWrite(pin_step, HIGH);
          delay(pause);
          digitalWrite(pin_step,LOW);
          delay (pause);  }
        digitalWrite(pin_direction, HIGH);
      for (int j=0; j<=pas;j++)
        { digitalWrite(pin_step, HIGH);
          delay(pause);
```

```
        digitalWrite(pin_step,LOW);
        delay (pause);    }
    }}

//XXXXXXXXXXXXXXXXXXXXXXXXXXXX* Fonction LOOP
void loop()
{
    //Oscillations(Nombre_oscillations, Nombre_de_pas);
}
```

Appendix C

Code of the final stretcher

```
Conversation.Request("get maxspeed");
Conversation.Request("set maxspeed", 100079);
Conversation.Request("get maxspeed");

Conversation.Request("home");
Conversation.PollUntilIdle();

Conversation.Request("move max");
Conversation.PollUntilIdle();

Conversation.Request("move rel -201575");
Conversation.PollUntilIdle();

Conversation.Request("get maxspeed");
Conversation.Request("set maxspeed", 10079);
Conversation.Request("get maxspeed");

var moveCount = 5;
var distance = 25000;

for (var i = 0; i < moveCount; i--)
{ Conversation.Request("move rel", -distance);
  Conversation.PollUntilIdle();
  Conversation.Request("move rel", +distance);
  Conversation.PollUntilIdle(); }
```


Bibliography

1. Helander, H. F. & Fändriks, L. Surface area of the digestive tract-revisited. *Scandinavian Journal of Gastroenterology* **49**, 681–689. ISSN: 15027708 (2014).
2. Rehfeld, A., Nylander, M. & Karnov, K. *Compendium of Histology* 517–539. ISBN: 978-3-319-41871-1. doi:10.1007/978-3-319-41873-5. <http://link.springer.com/10.1007/978-3-319-41873-5> (2017).
3. Štrkalj, G. & Chorn, D. Herophilus of Chalcedon and the practice of dissection in Hellenistic Alexandria. *South African Medical Journal* **98**, 86–89. ISSN: 02569574 (2008).
4. Krause, W. J. Brunner's glands: A structural, histochemical and pathological profile. *Progress in Histochemistry and Cytochemistry* **35**, 255–367. ISSN: 00796336 (2000).
5. Tortora, Derrickson, J., G. & Bryan. *Principles of Anatomy & Physiology, Cardiovascular System: Blood Vessels and Hemodynamics". Principles of Anatomy & Physiology (13th ed.). John Wiley & Sons. p. 816. ISBN 978-0470-56510-0* ISBN: 9781118345009 (2012).
6. Yeo, C. J. & MD. *Surgery of the alimentary tract* ISBN: 9780323402323 (2018).
7. DeSesso, J. M. & Jacobson, C. F. Anatomical and physiological parameters affecting gastrointestinal absorption in humans and rats. *Food and Chemical Toxicology* **39**, 209–228. ISSN: 02786915 (2001).
8. Jung, C., Hugot, J.-P. & Barreau, F. Peyer's Patches: The Immune Sensors of the Intestine. *International Journal of Inflammation* **2010**, 1–12. ISSN: 2042-0099 (2010).
9. Shyer, A. E. *et al.* Villification: how the gut gets its villi. *Science (New York, N. Y.)* **342**, 212–8. ISSN: 1095-9203 (2013).
10. Guiu, J. & Jensen, K. B. From Definitive Endoderm to Gut—a Process of Growth and Maturation. *Stem Cells and Development* **24**, 1972–1983. ISSN: 1547-3287 (2015).

11. McCorry, L. K. *Essentials of Human Physiology for Pharmacy, Second Edition* 520. ISBN: 1420043919 (2008).
12. Clevers, H. XThe intestinal crypt, a prototype stem cell compartment. *Cell* **154**, 274–284. ISSN: 00928674 (2013).
13. Chin, A. M., Hill, D. R., Aurora, M. & Spence, J. R. Morphogenesis and maturation of the embryonic and postnatal intestine. *Seminars in Cell and Developmental Biology* **66**, 81–93. ISSN: 10963634 (2017).
14. Jiang, P. *et al.* Antibiotics Increase Gut Metabolism and Antioxidant Proteins and Decrease Acute Phase Response and Necrotizing Enterocolitis in Preterm Neonates. *PLoS ONE* **7**. ISSN: 19326203. doi:10.1371/journal.pone.0044929 (2012).
15. Shyer, A. E. *et al.* Villification: How the gut gets its villi. *Science* **342**, 212–218. ISSN: 10959203 (2013).
16. Brittan, M. & Wright, N. A. The gastrointestinal stem cell. *Cell Proliferation* **37**, 35–53. ISSN: 09607722 (2004).
17. Meran, L., Baulies, A. & Li, V. S. W. Intestinal Stem Cell Niche: The Extracellular Matrix and Cellular Components. *Stem Cells International* **2017**, 1–11. ISSN: 1687-966X (2017).
18. Totafurno, J., Bjerknes, M. & Cheng, H. The crypt cycle. Crypt and villus production in the adult intestinal epithelium. *Biophysical Journal* **52**, 279–294. ISSN: 00063495 (1987).
19. Pageot, L. P. *et al.* Human cell models to study small intestinal functions: recapitulation of the crypt-villus axis. *Microscopy research and technique* **49**, 394–406. ISSN: 1059-910X (2000).
20. Barker, N. Adult intestinal stem cells: Critical drivers of epithelial homeostasis and regeneration. *Nature Reviews Molecular Cell Biology* **15**, 19–33. ISSN: 14710072 (2014).
21. Leblond, C. P. & Walker, B. E. Renewal of Cell populations. *American Physiological Society* **36** (1956).
22. Yousefi, M., Li, L. & Lengner, C. J. Hierarchy and Plasticity in the Intestinal Stem Cell Compartment. *Trends in Cell Biology* **27**, 753–764. ISSN: 18793088 (2017).
23. Van der Flier, L. G. & Clevers, H. Stem Cells, Self-Renewal, and Differentiation in the Intestinal Epithelium. *Annual Review of Physiology* **71**, 241–260. ISSN: 0066-4278 (2009).
24. Bevins, C. L. & Salzman, N. H. Paneth cells, antimicrobial peptides and maintenance of intestinal homeostasis. *Nature Reviews Microbiology* **9**, 356–368. ISSN: 17401526 (2011).

25. Sato, T. *et al.* Paneth cells constitute the niche for Lgr5 stem cells in intestinal crypts. *Nature* **469**, 415–418. ISSN: 00280836 (2011).
26. Potten, C. S., Owen, G. & Booth, D. Intestinal stem cells protect their genome by selective segregation of template DNA strands. *Journal of cell science* **115**, 2381–8. ISSN: 0021-9533 (2002).
27. Li, N., Nakauka-Ddamba, A., Tobias, J., Jensen, S. T. & Lengner, C. J. Mouse Label-Retaining Cells Are Molecularly and Functionally Distinct From Reserve Intestinal Stem Cells. *Gastroenterology* **151**, 298–310.e7. ISSN: 15280012 (2016).
28. Blander, J. M. Death in the intestinal epithelium—basic biology and implications for inflammatory bowel disease. *FEBS Journal* **283**, 2720–2730. ISSN: 17424658 (2016).
29. By, I. & Carroll, M. Exploring the Villus (2003).
30. Crawley, S. W., Mooseker, M. S. & Tyska, M. J. Shaping the intestinal brush border. *Journal of Cell Biology* **207**, 441–451. ISSN: 15408140 (2014).
31. Gustafsson, J. K. *et al.* The mucus and mucins of the goblet cells and enterocytes provide the first defense line of the gastrointestinal tract.pdf, 8–20 (2014).
32. McDole, J. R. *et al.* Goblet cells deliver luminal antigen to CD103+ dendritic cells in the small intestine. *Nature* **483**, 345–349. ISSN: 0028-0836 (2012).
33. Parker, H. E., Gribble, F. M. & Reimann, F. The role of gut endocrine cells in control of metabolism and appetite. *Experimental Physiology* **99**, 1116–1120. ISSN: 1469445X (2014).
34. Gribble, F. M. & Reimann, F. Enteroendocrine Cells: Chemosensors in the Intestinal Epithelium. *Annual Review of Physiology* **78**, 277–299. ISSN: 0066-4278 (2016).
35. Mabbott, N. A., Donaldson, D. S., Ohno, H., Williams, I. R. & Mahajan, A. Microfold (M) cells: Important immunosurveillance posts in the intestinal epithelium. *Mucosal Immunology* **6**, 666–677. ISSN: 19330219 (2013).
36. Gerbe, F. & Jay, P. Intestinal tuft cells: Epithelial sentinels linking luminal cues to the immune system. *Mucosal Immunology* **9**, 1353–1359. ISSN: 19353456 (2016).
37. Li, X. *et al.* Deconvoluting the intestine: molecular evidence for a major role of the mesenchyme in the modulation of signaling cross talk. *Physiological Genomics* **29**, 290–301. ISSN: 1094-8341 (2007).
38. Powell, D., Pinchuk, I., Saada, J., Chen, X. & Mifflin, R. Mesenchymal Cells of the Intestinal Lamina Propria. *Annual Review of Physiology* **73**, 213–237. ISSN: 0066-4278 (2011).

-
39. Roulis, M. & Flavell, R. A. Fibroblasts and myofibroblasts of the intestinal lamina propria in physiology and disease. *Differentiation* **92**, 116–131. ISSN: 14320436 (2016).
 40. Owens, B. M. J. & Simmons, A. Intestinal stromal cells in mucosal immunity and homeostasis. *Mucosal Immunology* **6**, 224–234. ISSN: 19330219 (2013).
 41. Crosnier, C., Stamataki, D. & Lewis, J. Organizing cell renewal in the intestine: Stem cells, signals and combinatorial control. *Nature Reviews Genetics* **7**, 349–359. ISSN: 14710056 (2006).
 42. Brink, G. R. Hedgehog Signaling in Development and Homeostasis of the Gastrointestinal Tract. *Physiol Rev* **87**, 1343–1375. ISSN: 0031-9333 (2007).
 43. Farin, H. F., Van Es, J. H. & Clevers, H. Redundant sources of Wnt regulate intestinal stem cells and promote formation of paneth cells. *Gastroenterology* **143**, 1518–1529.e7. ISSN: 00165085 (2012).
 44. Madison, B. B. Epithelial hedgehog signals pattern the intestinal crypt-villus axis. *Development* **132**, 279–289. ISSN: 0950-1991 (2005).
 45. Haramis, A. P. G. *et al.* De Novo Crypt Formation and Juvenile Polyposis on BMP Inhibition in Mouse Intestine. *Science* **303**, 1684–1686. ISSN: 00368075 (2004).
 46. Qi, Z. *et al.* BMP restricts stemness of intestinal Lgr5 + stem cells by directly suppressing their signature genes. *Nature Communications* **8**, 1–14. ISSN: 20411723 (2017).
 47. Valenta, T. *et al.* Wnt Ligands Secreted by Subepithelial Mesenchymal Cells Are Essential for the Survival of Intestinal Stem Cells and Gut Homeostasis. *Cell Reports* **15**, 911–918. ISSN: 22111247 (2016).
 48. Beumer, J. & Clevers, H. Regulation and plasticity of intestinal stem cells during homeostasis and regeneration. *Development* **143**, 3639–3649. ISSN: 0950-1991 (2016).
 49. Clevers, H., Loh, K. M. & Nusse, R. An integral program for tissue renewal and regeneration: Wnt signaling and stem cell control. *Science* **346**. ISSN: 10959203. doi:10.1126/science.1248012 (2014).
 50. Noah, T. K. & Shroyer, N. F. Notch in the Intestine: Regulation of Homeostasis and Pathogenesis. *Annual Review of Physiology* **75**, 263–288. ISSN: 0066-4278 (2013).
 51. Sancho, R., Cremona, C. A. & Behrens, A. Stem cell and progenitor fate in the mammalian intestine: Notch and lateral inhibition in homeostasis and disease. *EMBO reports* **16**, 571–581. ISSN: 1469-221X (2015).
 52. Yoo, B. B. & Mazmanian, S. K. The Enteric Network: Interactions between the Immune and Nervous Systems of the Gut. *Immunity* **46**, 910–926. ISSN: 10974180 (2017).

53. Obata, Y. & Pachnis, V. The Effect of Microbiota and the Immune System on the Development and Organization of the Enteric Nervous System. *Gastroenterology* **151**, 836–844. ISSN: 15280012 (2016).
54. Sommer, F. & Bäckhed, F. The gut microbiota-masters of host development and physiology. *Nature Reviews Microbiology* **11**, 227–238. ISSN: 17401526 (2013).
55. Wells, J. M., Rossi, O., Meijerink, M. & van Baarlen, P. Epithelial crosstalk at the microbiota-mucosal interface. *Proceedings of the National Academy of Sciences* **108**, 4607–4614. ISSN: 0027-8424 (2011).
56. Lyte, M. & Cryan, J. F. *Microbial Endocrinology: The Microbiota- Gut-Brain Axis in Health and Disease* **November 2015**, 432. ISBN: 9781493908967. doi:10.1007/978-1-4939-0987-4. <http://download.springer.com.ezp.lib.unimelb.edu.au/static/pdf/772/bok%7B%5C%%7D253A978-1-4939-0897-4.pdf?originUrl=http%7B%5C%%7D3A%7B%5C%%7D2F%7B%5C%%7D2Flink.springer.com%7B%5C%%7D2Fbook%7B%5C%%7D2F10.1007%7B%5C%%7D2F978-1-4939-0897-4%7B%5C%%7Dtoken2=exp=1495086750%7B~%7Dac1=%7B%5C%%7D2Fstatic%7B%5C%%7D2Fpdf%7B%5C%%7D2F772%7B%5C%%7D2Fbok%7B%5C%%7D253A978-1-4939-0897-4.pdf> (2014).
57. Kabouridis, P. S. *et al.* Microbiota controls the homeostasis of glial cells in the gut lamina propria. *Neuron* **85**, 289–295. ISSN: 10974199 (2015).
58. Macpherson, A. J., Yilmaz, B., Limenitakis, J. P. & Ganai-Vonarburg, S. C. IgA Function in Relation to the Intestinal Microbiota. *Annual Review of Immunology* **36**, annurev-immunol-042617-053238. ISSN: 0732-0582 (2018).
59. Purves, D. *et al.* *Neuroscience* 773. ISBN: 0878937250. doi:978-0878937257. arXiv: NBK10799 (2004).
60. Young, E. Gut instincts: The secrets of your second brain. *New Scientist* **216**, 38–42. ISSN: 02624079 (2012).
61. Lyte, M. & Cryan, J. F. *Microbial Endocrinology : The Microbiota- Gut-Brain Axis in Health and Disease* ISBN: 9781493908967 ().
62. Furness, J. B. The enteric nervous system: Normal functions and enteric neuropathies. *Neurogastroenterology and Motility* **20**, 32–38. ISSN: 13501925 (2008).
63. Costa, M. Anatomy and physiology of the enteric nervous system. *Gut* **47**, 15iv–19. ISSN: 00175749 (2000).
64. Podolsky, D. K. *Yamada's Atlas of Gastroenterology* Wiley. ISBN: 9781118496435 (2016).
65. Veiga-Fernandes, H. & Pachnis, V. Neuroimmune regulation during intestinal development and homeostasis. *Nature Immunology* **18**, 116–122. ISSN: 15292916 (2017).
66. Alvarez, C. AND. **69** (1924).

67. Mostafa, R. M., Moustafa, Y. M. & Hamdy, H. Interstitial cells of Cajal, the Maestro in health and disease. *World Journal of Gastroenterology* **16**, 3239–3248. ISSN: 10079327 (2010).
68. Costanzo, L. S. *Gastrointestinal Physiology* 339–393. ISBN: 9783319071633. doi:10.1007/978-3-319-91056-7 (2018).
69. Deloose, E., Janssen, P., Depoortere, I. & Tack, J. The migrating motor complex: control mechanisms and its role in health and disease. *Nature Reviews Gastroenterology & Hepatology* **9**, 271–285. ISSN: 1759-5045 (2012).
70. Klein, S. *et al.* Interstitial cells of Cajal integrate excitatory and inhibitory neurotransmission with intestinal slow-wave activity. *Nature Communications* **4**. ISSN: 20411723. doi:10.1038/ncomms2626 (2013).
71. Al-Shboul, O. The importance of interstitial cells of cajal in the gastrointestinal tract. *Saudi Journal of Gastroenterology* **19**, 3. ISSN: 1319-3767 (2013).
72. Boeckxstaens, G. *et al.* Fundamentals of neurogastroenterology: Physiology/-motility - Sensation. *Gastroenterology* **150**, 1292–1304e2. ISSN: 15280012 (2016).
73. Bredenoord, A. J., Smout, A. & Tack, J. *A Guide to Gastrointestinal Motility Disorders* 113. ISBN: 9789031378395. doi:10.1007/978-3-319-26938-2 (2010).
74. Deloose, E. & Tack, J. Redefining the functional roles of the gastrointestinal migrating motor complex and motilin in small bacterial overgrowth and hunger signaling. *American Journal of Physiology - Gastrointestinal and Liver Physiology* **310**, G228–G233. ISSN: 0193-1857 (2016).
75. Huizinga, J. D. *et al.* The origin of segmentation motor activity in the intestine. *Nature Communications* **5**, 1–11. ISSN: 20411723 (2014).
76. Huh, D., Hamilton, G. A. & Ingber, D. E. From 3D cell culture to organs-on-chips. *Trends in Cell Biology* **21**, 745–754. ISSN: 09628924 (2011).
77. Huh, D., Torisawa, Y. S., Hamilton, G. A., Kim, H. J. & Ingber, D. E. Micro-engineered physiological biomimicry: Organs-on-Chips. *Lab on a Chip* **12**, 2156–2164. ISSN: 14730189 (2012).
78. Dietzel, A. *Microsystems for pharmatechnology: Manipulation of fluids, particles, droplets, and cells* 1–348. ISBN: 9783319269207. doi:10.1007/978-3-319-26920-7 (2016).
79. Perestrelo, A. R., Águas, A. C., Rainer, A. & Forte, G. Microfluidic organ/body-on-a-chip devices at the convergence of biology and microengineering. *Sensors (Switzerland)* **15**, 31142–31170. ISSN: 14248220 (2015).
80. Bhatia, S. N. & Ingber, D. E. Microfluidic organs-on-chips. *Nature Biotechnology* **32**, 760–772. ISSN: 15461696 (2014).

81. Wikswo, J. P. *et al.* Engineering challenges for instrumenting and controlling integrated organ-on-chip systems. *IEEE Transactions on Biomedical Engineering* **60**, 682–690. ISSN: 00189294 (2013).
82. Kodzius, R., Schulze, F., Gao, X. & Schneider, M. R. Organ-on-chip technology: Current state and future developments. *Genes* **8**, 8–10. ISSN: 20734425 (2017).
83. Huh, D. *et al.* Reconstituting Organ-Level Lung. *Science* **328**, 1662–1668 (2010).
84. Kim, H. J., Huh, D., Hamilton, G. & Ingber, D. E. Human gut-on-a-chip inhabited by microbial flora that experiences intestinal peristalsis-like motions and flow. *Lab on a Chip* **12**, 2165–2174. ISSN: 14730189 (2012).
85. Huh, D. *et al.* Microfabrication of human organs-on-chips. *Nature Protocols* **8**, 2135–2157. ISSN: 1754-2189 (2013).
86. Grosberg, A., Alford, P. W., McCain, M. L. & Parker, K. K. Ensembles of engineered cardiac tissues for physiological and pharmacological study: Heart on a chip. *Lab on a Chip* **11**, 4165–4173. ISSN: 14730189 (2011).
87. Van den Broek, L. J., Bergers, L. I., Reijnders, C. M. & Gibbs, S. Progress and Future Prospectives in Skin-on-Chip Development with Emphasis on the use of Different Cell Types and Technical Challenges. *Stem Cell Reviews and Reports* **13**, 12. ISSN: 15586804 (2017).
88. Wilmer, M. J. *et al.* Kidney-on-a-Chip Technology for Drug-Induced Nephrotoxicity Screening. *Trends in Biotechnology* **34**, 156–170. ISSN: 18793096 (2016).
89. Arrigoni, C., Gilardi, M., Bersini, S., Candrian, C. & Moretti, M. Bioprinting and Organ-on-Chip Applications Towards Personalized Medicine for Bone Diseases. *Stem Cell Reviews and Reports* **13**, 407–417. ISSN: 15586804 (2017).
90. Dickey, C. A., Patterson, C., Dickson, D. & Petrucelli, L. Brain CHIP: removing the culprits in neurodegenerative disease. *Trends in Molecular Medicine* **13**, 32–38. ISSN: 14714914 (2007).
91. Griep, L. M. *et al.* BBB on CHIP: Microfluidic platform to mechanically and biochemically modulate blood-brain barrier function. *Biomedical Microdevices* **15**, 145–150. ISSN: 13872176 (2013).
92. Caballero, D. *et al.* Organ-on-chip models of cancer metastasis for future personalized medicine: From chip to the patient. *Biomaterials* **149**, 98–115. ISSN: 18785905 (2017).
93. Uhl, C. G., Shi, W. & Liu, Y. Organ-on-Chip Devices towards Applications in Drug Development and Screening: A Review. *Journal of Medical Device* **in press**, 30. ISSN: 1932-6181 (2018).
94. Shuler, M. L. Organ-, body- and disease-on-a-chip systems. *Lab on a Chip* **17**, 2345–2346. ISSN: 14730189 (2017).

-
95. Waseem, H. *et al.* *Nanotoxicology, Experimental and Computational perspectives* (eds Dhawan, A., Anderson, D. & Shanker, R.) 380. ISBN: 9781782629887 (Royal Society of Chemistry, 2017).
96. Ghaemmaghami, A. M., Hancock, M. J., Harrington, H., Kaji, H. & Khademhosseini, A. Biomimetic tissues on a chip for drug discovery. *Drug Discovery Today* **17**, 173–181. ISSN: 13596446 (2012).
97. Bhise, N. S. *et al.* Organ-on-a-chip platforms for studying drug delivery systems. *Journal of Controlled Release* **190**, 82–93. ISSN: 18734995 (2014).
98. Esch, E. W., Bahinski, A. & Huh, D. Organs-on-chips at the frontiers of drug discovery. *Nature Reviews Drug Discovery* **14**, 248–260. ISSN: 14741784 (2015).
99. Zhang, B., Korolj, A., Lai, B. F. L. & Radisic, M. Advances in organ-on-a-chip engineering. *Nature Reviews Materials* **3**, 257–278. ISSN: 20588437 (2018).
100. Wagner, I. *et al.* A dynamic multi-organ-chip for long-term cultivation and substance testing proven by 3D human liver and skin tissue co-culture. *Lab on a Chip* **13**, 3538–3547. ISSN: 14730189 (2013).
101. Luni, C., Serena, E. & Elvassore, N. Human-on-chip for therapy development and fundamental science. *Current Opinion in Biotechnology* **25**, 45–50. ISSN: 09581669 (2014).
102. Maschmeyer, I. *et al.* A four-organ-chip for interconnected long-term co-culture of human intestine, liver, skin and kidney equivalents. *Lab on a Chip* **15**, 2688–2699. ISSN: 14730189 (2015).
103. Huh, D. *et al.* A human disease model of drug toxicity-induced pulmonary edema in a lung-on-a-chip microdevice. *Science Translational Medicine* **4**. ISSN: 19466242. doi:10.1126/scitranslmed.3004249 (2012).
104. Benam, K. H. *et al.* Small airway-on-a-chip enables analysis of human lung inflammation and drug responses in vitro. *Nature Methods* **13**, 151–157. ISSN: 15487105 (2016).
105. Jain, A. *et al.* Primary Human Lung Alveolus-on-a-chip Model of Intravascular Thrombosis for Assessment of Therapeutics. *Clinical Pharmacology and Therapeutics* **103**, 332–340. ISSN: 15326535 (2018).
106. Kim, H. J., Lee, J., Choi, J.-H., Bahinski, A. & Ingber, D. E. Co-culture of Living Microbiome with Microengineered Human Intestinal Villi in a Gut-on-a-Chip Microfluidic Device. *Journal of Visualized Experiments*, 3–9. ISSN: 1940-087X (2016).
107. Bein, A. *et al.* Microfluidic Organ-on-a-Chip Models of Human Intestine. *Cmgh* **5**, 659–668. ISSN: 2352345X (2018).
108. Richmond, C. A. & Breault, D. T. Move Over Caco-2 Cells: Human-Induced Organoids Meet Gut-on-a-Chip. *Cmgh* **5**, 634–635. ISSN: 2352345X (2018).

109. Sakalem, M. E. & Ribeiro-Paes, J. T. New methodologies for old problems: Tridimensional gastrointestinal organoids and guts-on-a-chip. *Journal of Coloproctology* **38**, 90–93. ISSN: 22379363 (2018).
110. Sato, T. *et al.* Single Lgr5 stem cells build crypt-villus structures in vitro without a mesenchymal niche. *Nature* **459**, 262–265. ISSN: 00280836 (2009).
111. Dutta, D., Heo, I. & Clevers, H. Disease Modeling in Stem Cell-Derived 3D Organoid Systems. *Trends in Molecular Medicine* **23**, 393–410. ISSN: 1471499X (2017).
112. Tottey, W. *et al.* The Human Gut Chip "HuGChip", an Explorative Phylogenetic Microarray for Determining Gut Microbiome Diversity at Family Level. *PLoS ONE* **8**, 1–12. ISSN: 19326203 (2013).
113. Chen, Y. *et al.* Robust bioengineered 3D functional human intestinal epithelium. *Scientific Reports* **5**, 1–11. ISSN: 20452322 (2015).
114. Salomon, J. *et al.* Contractile forces at tricellular contacts modulate epithelial organization and monolayer integrity. *Nature Communications* **8**. ISSN: 20411723. doi:10.1038/ncomms13998 (2017).
115. Yu, J., Peng, S., Luo, D. & March, J. C. In vitro 3D human small intestinal villous model for drug permeability determination. *Biotechnology and Bioengineering* **109**, 2173–2178. ISSN: 00063592 (2012).
116. Costello, C. M. *et al.* Synthetic small intestinal scaffolds for improved studies of intestinal differentiation. *Biotechnology and Bioengineering* **111**, 1222–1232. ISSN: 10970290 (2014).
117. Wang, Y. *et al.* A microengineered collagen scaffold for generating a polarized crypt-villus architecture of human small intestinal epithelium. *Biomaterials* **128**, 44–55. ISSN: 18785905 (2017).
118. Shim, K. Y. *et al.* Microfluidic gut-on-a-chip with three-dimensional villi structure. *Biomedical Microdevices* **19**. ISSN: 15728781. doi:10.1007/s10544-017-0179-y (2017).
119. Yissachar, N. *et al.* An Intestinal Organ Culture System Uncovers a Role for the Nervous System in Microbe-Immune Crosstalk. *Cell* **168**, 1135–1148.e12. ISSN: 10974172 (2017).
120. Kim, H. J. & Ingber, D. E. Gut-on-a-Chip microenvironment induces human intestinal cells to undergo villus differentiation. *Integrative Biology (United Kingdom)* **5**, 1130–1140. ISSN: 17579694 (2013).
121. Kasendra, M. *et al.* Development of a primary human Small Intestine-on-a-Chip using biopsy-derived organoids. *Scientific Reports* **8**, 1–14. ISSN: 20452322 (2018).
122. Verhulsel, M. *Reproduction in vitro d ' un intestin sur puce microfluidique* PhD thesis (Université Pierre et Marie Curie (UPMC)), 162.

-
123. Thampatty, J. H. W. B. P. An introductory review of cell mechanobiology, 1–16 (2006).
 124. Jaalouk, D. E. & Lammerding, J. Mechanotransduction gone awry. *Nature Reviews Molecular Cell Biology* **10**, 63–73. ISSN: 14710072 (2009).
 125. Jansen, K. A. *et al.* A guide to mechanobiology: Where biology and physics meet. *Biochimica et Biophysica Acta - Molecular Cell Research* **1853**, 3043–3052. ISSN: 18792596 (2015).
 126. Engler, A. J., Sen, S., Sweeney, H. L. & Discher, D. E. Matrix Elasticity Directs Stem Cell Lineage Specification. *Cell* **126**, 677–689. ISSN: 00928674 (2006).
 127. Jufri, N. F., Mohamedali, A., Avolio, A. & Baker, M. S. Mechanical stretch: Physiological and pathological implications for human vascular endothelial cells. *Vascular Cell* **7**, 1–12. ISSN: 2045824X (2015).
 128. Tan, J. *et al.* Decreased osteogenesis of adult mesenchymal stem cells by reactive oxygen species under cyclic stretch: A possible mechanism of age related osteoporosis. *Bone Research* **3**. ISSN: 20956231. doi:10.1038/boneres.2015.3 (2015).
 129. Vining, K. H. & Mooney, D. J. Mechanical forces direct stem cell behaviour in development and regeneration. *Nature Reviews Molecular Cell Biology* **18**, 728–742. ISSN: 14710080 (2017).
 130. Hoffman, B. D., Grashoff, C. & Schwartz, M. A. Dynamic molecular processes mediate cellular mechanotransduction. *Nature* **475**, 316–323. ISSN: 00280836 (2011).
 131. Kobayashi, T. & Sokabe, M. Sensing substrate rigidity by mechanosensitive ion channels with stress fibers and focal adhesions. *Current Opinion in Cell Biology* **22**, 669–676. ISSN: 09550674 (2010).
 132. Sapir, L. & Tzliil, S. Talking over the extracellular matrix: How do cells communicate mechanically? *Seminars in Cell and Developmental Biology* **71**, 99–105. ISSN: 10963634 (2017).
 133. Schwartz, M. A. & DeSimone, D. W. Cell adhesion receptors in mechanotransduction. *Current Opinion in Cell Biology* **20**, 551–556. ISSN: 09550674 (2008).
 134. Gu, Y. & Gu, C. Physiological and Pathological Functions of Mechanosensitive Ion Channels. *Molecular Neurobiology* **50**, 339–347. ISSN: 15591182 (2014).
 135. Coste, B. *et al.* Activated Cation Channels. *October* **330**, 7–12. ISSN: 0036-8075 (2010).
 136. Ranade, S. S., Syeda, R. & Patapoutian, A. Mechanically Activated Ion Channels. *Neuron* **87**, 1162–1179. ISSN: 10974199 (2015).
 137. Gudipaty, S. A. *et al.* Mechanical stretch triggers rapid epithelial cell division through Piezo1. *Nature* **543**, 118–121. ISSN: 14764687 (2017).

138. McMahon, L. A., Campbell, V. A. & Prendergast, P. J. Involvement of stretch-activated ion channels in strain-regulated glycosaminoglycan synthesis in mesenchymal stem cell-seeded 3D scaffolds. *Journal of Biomechanics* **41**, 2055–2059. ISSN: 00219290 (2008).
139. Hynes, R. O. Integrins: Bidirectional, allosteric signaling machines. *Cell* **110**, 673–687. ISSN: 00928674 (2002).
140. Chen, W., Lou, J., Evans, E. A. & Zhu, C. Observing force-regulated conformational changes and ligand dissociation from a single integrin on cells. *Journal of Cell Biology* **199**, 497–512. ISSN: 00219525 (2012).
141. Kong, F. *et al.* Cyclic mechanical reinforcement of integrin-ligand interactions. *Molecular Cell* **49**, 1060–1068. ISSN: 10972765 (2013).
142. Jansen, K. A., Atherton, P. & Ballestrem, C. Mechanotransduction at the cell-matrix interface. *Seminars in Cell and Developmental Biology* **71**, 75–83. ISSN: 10963634 (2017).
143. Yan, J., Yao, M., Goult, B. T. & Sheetz, M. P. Talin Dependent Mechanosensitivity of Cell Focal Adhesions. *Cellular and Molecular Bioengineering* **8**, 151–159. ISSN: 18655033 (2015).
144. Sun, Z., Guo, S. S. & Fässler, R. Integrin-mediated mechanotransduction. *Journal of Cell Biology* **215**. ISSN: 15408140. doi:10.1083/jcb.201609037 (2016).
145. Case, L. B. & Waterman, C. M. Integration of actin dynamics and cell adhesion by a three-dimensional, mechanosensitive molecular clutch. *Nature Cell Biology* **17**, 955–963. ISSN: 14764679 (2015).
146. Burridge, K. & Guilluy, C. Focal adhesions, stress fibers and mechanical tension. *Experimental Cell Research* **343**, 14–20. ISSN: 10902422 (2016).
147. Smith, M. A., Hoffman, L. M. & Beckerle, M. C. LIM proteins in actin cytoskeleton mechanoresponse. *Trends in Cell Biology* **24**, 575–583. ISSN: 18793088 (2014).
148. Ross, T. D. *et al.* Integrins in mechanotransduction. *Current Opinion in Cell Biology* **25**, 613–618. ISSN: 09550674 (2013).
149. Harris, A. R. *et al.* Characterizing the mechanics of cultured cell monolayers. *Proceedings of the National Academy of Sciences* **109**, 16449–16454. ISSN: 0027-8424 (2012).
150. Alberts, B. *et al.* *Molecular biology of the Cell* 4th, 1560. ISBN: 978-0-8153-4105-5. doi:10.1016/0014-2999(85)90385-1. arXiv: MolecularBiologyoftheCell, 4thedition (2002).
151. Charras, G. & Yap, A. S. Tensile Forces and Mechanotransduction at Cell–Cell Junctions. *Current Biology* **28**, R445–R457. ISSN: 09609822 (2018).

-
152. Takeichi, M. Dynamic contacts: Rearranging adherens junctions to drive epithelial remodelling. *Nature Reviews Molecular Cell Biology* **15**, 397–410. ISSN: 14710080 (2014).
 153. Buckley, C. D. *et al.* The minimal cadherin-catenin complex binds to actin filaments under force. *Science* **346**. ISSN: 10959203. doi:10.1126/science.1254211. arXiv: 15334406 (2014).
 154. Huveneers, S. & de Rooij, J. Mechanosensitive systems at the cadherin-F-actin interface. *Journal of Cell Science* **126**, 403–413. ISSN: 0021-9533 (2013).
 155. Harris, A. R., Daeden, A. & Charras, G. T. Formation of adherens junctions leads to the emergence of a tissue-level tension in epithelial monolayers. *Journal of Cell Science* **127**, 2507–2517. ISSN: 0021-9533 (2014).
 156. Wyatt, T., Baum, B. & Charras, G. A question of time: Tissue adaptation to mechanical forces. *Current Opinion in Cell Biology* **38**, 68–73. ISSN: 18790410 (2016).
 157. Friedl, P. & Mayor, R. Tuning Collective Cell Migration by Cell – Cell Junction Regulation. *Cold Spring Harbor Perspectives in Biology*, 1–18. ISSN: 1943-0264 (2017).
 158. Leung, D. Y. M., Glagov, S. & Mathews, M. B. Cyclic Stretching Stimulates Synthesis of Matrix Components by Arterial Smooth Muscle Cells in vitro Abstract . Rabbit aortic medial cells were grown on purified elastin membranes , which. *Science* **191**, 475–477 (1976).
 159. Mihic, A. *et al.* The effect of cyclic stretch on maturation and 3D tissue formation of human embryonic stem cell-derived cardiomyocytes. *Biomaterials* **35**, 2798–2808. ISSN: 01429612 (2014).
 160. Lux, M. *et al.* In vitro maturation of large-scale cardiac patches based on a perfusable starter matrix by cyclic mechanical stimulation. *Acta Biomaterialia* **30**, 177–187. ISSN: 18787568 (2016).
 161. Qin, T. W. *et al.* Effect of mechanical stimulation on bone marrow stromal cell-seeded tendon slice constructs: A potential engineered tendon patch for rotator cuff repair. *Biomaterials* **51**, 43–50. ISSN: 18785905 (2015).
 162. Rosenfeld, D. *et al.* Morphogenesis of 3D vascular networks is regulated by tensile forces. *Proceedings of the National Academy of Sciences* **113**, 3215–3220. ISSN: 0027-8424 (2016).
 163. Song, Y. *et al.* Cyclic mechanical stretch enhances BMP9-induced osteogenic differentiation of mesenchymal stem cells. *International Orthopaedics* **42**, 947–955. ISSN: 14325195 (2018).

-
164. Morita, Y., Watanabe, S., Ju, Y. & Xu, B. Determination of optimal cyclic Uniaxial stretches for stem cell-to-tenocyte differentiation under a wide range of mechanical stretch conditions by evaluating gene expression and protein synthesis levels. *Acta of Bioengineering and Biomechanics* **15**, 71–79. ISSN: 1509409X (2013).
165. Morita, Y., Yamashita, T., Toku, Y. & Ju, Y. Optimization of differentiation time of mesenchymal-stem-cell to tenocyte under a cyclic stretching with a microgrooved culture membrane and selected measurement cells. *Acta of Bioengineering and Biomechanics* **20**, 3–10. ISSN: 1509409X (2018).
166. Ahmed, W. W. *et al.* Myoblast morphology and organization on biochemically micro-patterned hydrogel coatings under cyclic mechanical strain. *Biomaterials* **31**, 250–258. ISSN: 01429612 (2010).
167. Campos, L. C. G. *et al.* Cyclic stretch-induced Crp3 sensitizes vascular smooth muscle cells to apoptosis during vein arterialization remodeling. *Clinical science (London, England : 1979)* **132**, 449–459. ISSN: 1470-8736 (2018).
168. Montenegro, M. F. *et al.* Nox4-dependent activation of cofilin mediates VSMC reorientation in response to cyclic stretching. *Free Radical Biology and Medicine* **85**, 288–294. ISSN: 18734596 (2015).
169. Hayakawa, K., Sato, N. & Obinata, T. Dynamic reorientation of cultured cells and stress fibers under mechanical stress from periodic stretching. *Experimental Cell Research* **268**, 104–114. ISSN: 00144827 (2001).
170. Hayakawa, K., Hosokawa, A., Yabusaki, K. & Obinata, T. Orientation of Smooth Muscle-Derived A10 Cells in Culture by Cyclic Stretching: Relationship between Stress Fiber Rearrangement and Cell Reorientation. *Zoological Science* **17**, 617. ISSN: 0289-0003 (2000).
171. Wang, D. *et al.* A stretching device for imaging real-time molecular dynamics of live cells adhering to elastic membranes on inverted microscopes during the entire process of the stretch. *Integrative Biology* **2**, 288–293. ISSN: 17579694 (2010).
172. Kaneko, D. *et al.* Temporal effects of cyclic stretching on distribution and gene expression of integrin and cytoskeleton by ligament fibroblasts in vitro. *Connective Tissue Research* **50**, 263–269. ISSN: 03008207 (2009).
173. Cui, Y. *et al.* Cyclic stretching of soft substrates induces spreading and growth. *Nature communications* **6**, 6333. ISSN: 2041-1723 (2015).
174. Abiko, H. *et al.* Rho guanine nucleotide exchange factors involved in cyclic-stretch-induced reorientation of vascular endothelial cells. *Journal of Cell Science* **128**, 1683–1695. ISSN: 0021-9533 (2015).

175. Wang, J. H., Goldschmidt-Clermont, P. & Yin, F. C. Contractility affects stress fiber remodeling and reorientation of endothelial cells subjected to cyclic mechanical stretching. *Annals of Biomedical Engineering* **28**, 1165–1171. ISSN: 00906964 (2000).
176. Wang, J. H., Goldschmidt-Clermont, P., Wille, J. & Yin, F. C. Specificity of endothelial cell reorientation in response to cyclic mechanical stretching. *Journal of Biomechanics* **34**, 1563–1572. ISSN: 00219290 (2001).
177. Tondon, A. & Kaunas, R. The direction of stretch-induced cell and stress fiber orientation depends on collagen matrix stress. *PLoS ONE* **9**. ISSN: 19326203. doi:10.1371/journal.pone.0089592 (2014).
178. Cavanaugh K.J., J., Oswari, J. & Margulies, S. S. Role of stretch on tight junction structure in alveolar epithelial cells. *American Journal of Respiratory Cell and Molecular Biology* **25**, 584–591. ISSN: 10441549 (2001).
179. Craig, D. H., Zhang, J. & Basson, M. D. Cytoskeletal signaling by way of α -actinin-1 mediates ERK1/2 activation by repetitive deformation in human Caco2 intestinal epithelial cells. *American Journal of Surgery* **194**, 618–622. ISSN: 00029610 (2007).
180. Chaturvedi, L. S., Marsh, H. M., Shang, X., Zheng, Y. & Basson, M. D. Repetitive deformation activates focal adhesion kinase and ERK mitogenic signals in human Caco-2 intestinal epithelial cells through Src and Rac1. *Journal of Biological Chemistry* **282**, 14–28. ISSN: 00219258 (2007).
181. Chaturvedi, L. S., Saad, S. A., Bakshi, N., Marsh, H. M. & Basson, M. D. Strain Matrix-Dependently Dissociates Gut Epithelial Spreading and Motility. *Journal of Surgical Research* **156**, 217–223. ISSN: 00224804 (2009).
182. Chaturvedi, L. S., Marsh, H. M. & Basson, M. D. Role of RhoA and its effectors ROCK and mDia1 in the modulation of deformation-induced FAK, ERK, p38, and MLC motogenic signals in human Caco-2 intestinal epithelial cells. *AJP: Cell Physiology* **301**, C1224–C1238. ISSN: 0363-6143 (2011).
183. Kim, H. J., Li, H., Collins, J. J. & Ingber, D. E. Contributions of microbiome and mechanical deformation to intestinal bacterial overgrowth and inflammation in a human gut-on-a-chip. *Proceedings of the National Academy of Sciences* **113**, E7–E15. ISSN: 0027-8424 (2016).
184. Kamble, H., Barton, M. J., Jun, M., Park, S. & Nguyen, N. T. Cell stretching devices as research tools: Engineering and biological considerations. *Lab on a Chip* **16**, 3193–3203. ISSN: 14730189 (2016).
185. Iwase, E., Shimoyama, I., Kan, T., Matsumoto, K. & Heo, Y. J. Stretchable cell culture platforms using micropneumatic actuators. *Micro & Nano Letters* **8**, 865–868. ISSN: 1750-0443 (2013).

186. Moraes, C., Chen, J. H., Sun, Y. & Simmons, C. A. Microfabricated arrays for high-throughput screening of cellular response to cyclic substrate deformation. *Lab on a Chip* **10**, 227–234. ISSN: 14730189 (2010).
187. Cui, Y. *et al.* Cyclic stretching of soft substrates induces spreading and growth. *Nature Communications* **6**, 1–8. ISSN: 20411723 (2015).
188. Paul, N. E. *et al.* The effect of mechanical stress on the proliferation, adipogenic differentiation and gene expression of human adipose-derived stem cells. *Journal of Tissue Engineering and Regenerative Medicine* **12**, 276–284. ISSN: 19326254 (2018).
189. Shikata, Y. *et al.* Differential effects of shear stress and cyclic stretch on focal adhesion remodeling, site-specific FAK phosphorylation, and small GTPases in human lung endothelial cells. *Experimental Cell Research* **304**, 40–49. ISSN: 00144827 (2005).
190. Samak, G. *et al.* Cyclic stretch disrupts apical junctional complexes in Caco-2 cell monolayers by a JNK-2-, c-Src-, and MLCK-dependent mechanism. *AJP: Gastrointestinal and Liver Physiology* **306**, G947–G958. ISSN: 0193-1857 (2014).
191. Tremblay, D., Chagnon-Lessard, S., Mirzaei, M., Pelling, A. E. & Godin, M. A microscale anisotropic biaxial cell stretching device for applications in mechanobiology. *Biotechnology Letters* **36**, 657–665. ISSN: 15736776 (2014).
192. Huang, Y. & Nguyen, N.-T. A polymeric cell stretching device for real-time imaging with optical microscopy. *Biomedical Microdevices* **15**, 1043–1054. ISSN: 1387-2176 (2013).
193. Kamotani, Y. *et al.* Individually programmable cell stretching microwell arrays actuated by a Braille display. *Biomaterials* **29**, 2646–2655. ISSN: 01429612 (2008).
194. Chang, Y. J., Tsai, C. J., Tseng, F. G., Chen, T. J. & Wang, T. W. Micropatterned stretching system for the investigation of mechanical tension on neural stem cells behavior. *Nanomedicine: Nanotechnology, Biology, and Medicine* **9**, 345–355. ISSN: 15499634 (2013).
195. Deguchi, S., Kudo, S., Matsui, T. S., Huang, W. & Sato, M. Piezoelectric actuator-based cell microstretch device with real-time imaging capability. *AIP Advances* **5**. ISSN: 21583226. doi:10.1063/1.4922220 (2015).
196. Tschumperlin, D. J. & Margulies, S. S. Equibiaxial deformation-induced injury of alveolar epithelial cells in vitro. *American Journal of Physiology-Lung Cellular and Molecular Physiology* **275**, L1173–L1183. ISSN: 1040-0605 (1998).
197. Morita, Y., Matsubara, F., Toku, Y. & Ju, Y. Use of a Tendon / Ligament Cell Sheet with Mesenchymal Stem Cells and Cyclic Stretch Stimulus for Tendon / Ligament Tissue Restoration. **5**, 1–11 (2018).
198. Livne, A., Bouchbinder, E. & Geiger, B. Cell reorientation under cyclic stretching. *Nature communications* **5**, 1–8. ISSN: 2041-1723 (2014).

-
199. Schad, J. F. *et al.* Cyclic strain upregulates VEGF and attenuates proliferation of vascular smooth muscle cells. *Biochemical Journal* **308**, 697–711. ISSN: 0264-6021 (1995).
200. Mantella, L. E., Quan, A. & Verma, S. Variability in vascular smooth muscle cell stretch-induced responses in 2D culture. *Vascular Cell* **7**, 1–9. ISSN: 2045824X (2015).
201. Qi, Y.-X. *et al.* Nuclear envelope proteins modulate proliferation of vascular smooth muscle cells during cyclic stretch application. *Proceedings of the National Academy of Sciences* **113**, 5293–5298. ISSN: 0027-8424 (2016).
202. Peyton, K. J., Liu, X.-m. & Durante, W. Prolonged cyclic strain inhibits human endothelial cell growth, 205–212 (2016).
203. Tan, S. & Barker, N. Epithelial stem cells and intestinal cancer. *Seminars in Cancer Biology* **32**, 40–53. ISSN: 10963650 (2015).
204. Ghazanfari, S., Tafazzoli-Shadpour, M. & Shokrgozar, M. A. Effects of cyclic stretch on proliferation of mesenchymal stem cells and their differentiation to smooth muscle cells. *Biochemical and Biophysical Research Communications* **388**, 601–605. ISSN: 0006291X (2009).
205. Sun, L. *et al.* Effects of Mechanical Stretch on Cell Proliferation and Matrix Formation of Mesenchymal Stem Cell and Anterior Cruciate Ligament Fibroblast. *Stem Cells International* **2016**. ISSN: 16879678. doi:10.1155/2016/9842075 (2016).
206. Banerjee, I. *et al.* Cyclic stretch of embryonic cardiomyocytes increases proliferation, growth, and expression while repressing Tgf- β signaling. *Journal of Molecular and Cellular Cardiology* **79**, 133–144. ISSN: 10958584 (2015).
207. Chen, K. *et al.* Role of boundary conditions in determining cell alignment in response to stretch. *Proceedings of the National Academy of Sciences* **115**, 986–991. ISSN: 0027-8424 (2018).
208. Basson, M. D., Turowski, G. & Emenaker, N. J. Regulation of human (Caco-2) intestinal epithelial cell differentiation by extracellular matrix proteins. *Experimental Cell Research* **225**, 301–305. ISSN: 00144827 (1996).
209. Wang, L., Sun, B., Ziemer, K. S., Barabino, G. A. & Carrier, R. L. Chemical and physical modifications to poly(dimethylsiloxane) surfaces affect adhesion of Caco-2 cells. *Journal of Biomedical Materials Research - Part A* **93**, 1260–1271. ISSN: 15493296 (2010).
210. Beaulieu, J. F. Integrins and human intestinal cell functions. *Journal Of Cell Biology*, 310–321 (1999).
211. Lussier, C., Basora, N., Bouatrouss, Y. & Beaulieu, J. F. Integrins as mediators of epithelial cell-matrix interactions in the human small intestinal mucosa. *Microscopy Research and Technique* **51**, 169–178. ISSN: 1059910X (2000).

-
212. Vllasaliu, D., Falcone, F. H., Stolnik, S. & Garnett, M. Basement membrane influences intestinal epithelial cell growth and presents a barrier to the movement of macromolecules. *Experimental Cell Research* **323**, 218–231. ISSN: 10902422 (2014).
213. Teller, I. C. & Beaulieu, J. F. Interactions between laminin and epithelial cells in intestinal health and disease. *Expert Reviews in Molecular Medicine* **3**, 1–18. ISSN: 14623994 (2001).
214. Yurchenco, P. D. Basement Membranes: Cell Scaffoldings and Signaling Platforms. *Cold Spring Harbor Perspectives in Biology* **3**, 1–28. ISSN: 1943-0264 (2011).
215. Turck, N. *et al.* Laminin isoforms: Biological roles and effects on the intracellular distribution of nuclear proteins in intestinal epithelial cells. *Experimental Cell Research* **303**, 494–503. ISSN: 00144827 (2005).
216. Koçer, G. & Jonkheijm, P. About Chemical Strategies to Fabricate Cell-Instructive Biointerfaces with Static and Dynamic Complexity. *Advanced Healthcare Materials* **7**, 1–32. ISSN: 21922659 (2018).
217. Charras, G. & Sahai, E. Physical influences of the extracellular environment on cell migration. *Nature Reviews Molecular Cell Biology* **15**, 813–824. ISSN: 14710080 (2014).
218. Gunawan, R. C., Silvestre, J., Gaskins, H. R., Kenis, P. J. & Leckband, D. E. Cell migration and polarity on microfabricated gradients of extracellular matrix proteins. *Langmuir* **22**, 4250–4258. ISSN: 07437463 (2006).
219. Maheshwari, G., Brown, G., Lauffenburger, D. A., Wells, A. & Griffith, L. G. Cell adhesion and motility depend on nanoscale RGD clustering. *Journal of cell science* **113** (Pt 1, 1677–1686. ISSN: 0021-9533 (2000).
220. Selhuber-Unkel, C. *et al.* Cell adhesion strength is controlled by intermolecular spacing of adhesion receptors. *Biophysical Journal* **98**, 543–551. ISSN: 15420086 (2010).
221. Koo, L. Y., Irvine, D. J., Mayes, A. M., Lauffenburger, D. a. & Griffith, L. G. Co-regulation of cell adhesion by nanoscale RGD organization and mechanical stimulus. *Journal of Cell Science* **115**, 1423–1433. ISSN: 0021-9533 (2002).
222. Kuddannaya, S. *et al.* Surface chemical modification of poly(dimethylsiloxane) for the enhanced adhesion and proliferation of mesenchymal stem cells. *ACS Applied Materials and Interfaces* **5**, 9777–9784. ISSN: 19448244 (2013).
223. Wipff, P. J. *et al.* The covalent attachment of adhesion molecules to silicone membranes for cell stretching applications. *Biomaterials* **30**, 1781–1789. ISSN: 01429612 (2009).

- 224. Yamashita, T., Kollmannsberger, P., Mawatari, K., Kitamori, T. & Vogel, V. Cell sheet mechanics: How geometrical constraints induce the detachment of cell sheets from concave surfaces. *Acta Biomaterialia* **45**, 85–97. ISSN: 18787568 (2016).
- 225. Simon-Assmann, P., Turck, N., Sidhoum-Jenny, M., Gradwohl, G. & Kedinger, M. In vitro models of intestinal epithelial cell differentiation. *Cell Biology and Toxicology* **23**, 241–256. ISSN: 07422091 (2007).
- 226. Schindelin, J. *et al.* Fiji: An open-source platform for biological-image analysis. *Nature Methods* **9**, 676–682. ISSN: 15487091 (2012).
- 227. Aigouy, B., Umetsu, D. & Eaton, S. *Drosophila*. **1478**, 227–239 (2016).
- 228. Aigouy, B. *et al.* Cell Flow Reorients the Axis of Planar Polarity in the Wing Epithelium of *Drosophila*. *Cell* **142**, 773–786. ISSN: 00928674 (2010).
- 229. ATCC. Colorectal Adenocarcinoma. **37**, 1–25 (2012).
- 230. Edelstein-Keshet, L. *A Primer on Mathematical Models in Biology* ISBN: 978-0-89871-554-5. doi:10.1137/1.9780898719147. arXiv: 9809069v1 [arXiv:gr-qc]. <http://epubs.siam.org/doi/book/10.1137/1.9780898719147> (2005).
- 231. Wang, L., Murthy, S. K., Fowle, W. H., Barabino, G. A. & Carrier, R. L. Influence of micro-well biomimetic topography on intestinal epithelial Caco-2 cell phenotype. *Biomaterials* **30**, 6825–6834. ISSN: 01429612 (2009).
- 232. Sun, B., Xie, K., Chen, T. H. & Lam, R. H. Preferred cell alignment along concave microgrooves. *RSC Advances* **7**, 6788–6794. ISSN: 20462069 (2017).
- 233. Ma, X. *et al.* Fibers in the extracellular matrix enable long-range stress transmission between cells. *Biophysical Journal* **104**, 1410–1418. ISSN: 00063495 (2013).

Titre: D  veloppement d'un mod  le d'intestin *in-vitro* incluant le p  ristaltisme

R  sum  : Le *Gut-on-chip* fait partie d'un th  me de recherche plus g  n  rale, appelez *Organ-on-chip* qui a pour objectif de d  velopper des mod  les *in-vitro* qui r  capitulent des caract  ristiques essentielles de l'organe d'int  r  t. Dans le cas de l'intestin, les *Gut-on-chip* plateformes ont   t   principalement d  velopp  es pour reconstituer soit l'architecture 3D de l'intestin, soit sa dynamique et plus particuli  rement le p  ristaltisme. Durant ma th  se j'ai d  velopp   une nouvelle et polyvalente *Gut-on-chip*, pr  sentant ces deux aspects du micro-environnement intestinale. Cette *Peristalsis-on-chip* nous a permis d'  tudier l'influence du mouvement p  ristaltique sur le comportement cellulaire en fonction de la g  om  trie de la structure. Pour cette   tude nous avons ensemenc   des cellules Caco2 sur des substrats 2D ou 3D recouvert de laminine et les avons soumis    un   tirement cyclique (   0.2 Hz et 10%) pendant 2, 5, 8, 16, 24 et 48 heures. Lors de ces exp  riences nous avons pu observer une r  orientation cellulaire perpendiculaire    l'axe d'  tirement que nous avons caract  ris   en fonction des conditions de recouvrement, de la confluence initiale, du temps d'  tirement et de la g  om  trie de la structure. Il est int  ressant de noter que la r  ponse cellulaire la plus importante a   t   obtenue par la combinaison de la g  om  trie 3D et de l'  tirement, ce qui illustre bien le besoin de ces deux   l  ments pour mieux mimer les conditions intestinales *in-vivo*.

Mots cl  s: Organ-on-chip, Gut-on-chip, P  ristaltisme, Intestin, Caco2, 3D culture, Reorientation cellulaire,   tirement

Title: Development of an in vitro intestinal model featuring peristaltic motion

Abstract: *Gut-on-chip* is part of a more general research theme, the so-called *Organ-on-chip* that aims at developing *in-vitro* models which recapitulate key features of an organ of interest. In the case of the intestine, *Gut-on-chip* platforms have been mainly developed to reconstitute either the intestinal 3D architecture or its dynamics, especially the peristalsis. Throughout my PhD I developed a new versatile *Gut-on-chip*, featuring both of these aspects of the intestinal micro-environment. This *Peristalsis-on-chip* allowed us to study the influence of peristaltic motion on cellular behavior, depending on the geometry of the scaffold. For this study Caco2 cells have been seeded either on a 2D or a 3D substrate coated with laminin and submitted to a cyclic stretching (at 0.2 Hz and 10%) for 2, 5, 8, 16, 24 and 48 hours. From these experiments we observed a cellular reorientation perpendicular to the axis of stretching. We then characterized this cellular response as a function of the coating condition, the initial confluency, the stretching time and the scaffold geometry. Interestingly, the strongest response was obtained when the 3D geometry and the stretching were combined, therefore illustrating the need of these two features to better mimic the intestinal *in vivo* conditions.

Keywords: Organ-on-chip, Gut-on-chip, Peristalsis, Intestine, Caco2, 3D scaffold, Cellular reorientation, Stretching